Multivariable H_∞ control for an active magnetic bearing flywheel system

A dissertation presented to

The School of Electrical, Electronic and Computer Engineering

North-West University

In partial fulfilment of the requirements for the degree

Magister Ingeneriae

in Computer and Electronic Engineering

by

Stephanus Jacobus Marais Steyn

Supervisor: Dr. P. A. van Vuuren

Co-supervisor: Prof. G. van Schoor

Date: October 2010

Potchefstroom Campus

Abstract

Conventional ball-bearings in rotational applications can potentially be replaced by active magnetic bearings (AMBs). AMBs levitate the rotor via contact-free, actively controlled, electromagnetic forces. At the North-West University, AMBs are applied to a flywheel uninterrupted power supply (Fly-UPS) system. Regrettably, AMBs are inherently open-loop unstable because of the inverse displacement-force relationship, and for this reason requires closed-loop feedback control. Thus, the feasibility of multivariable H_∞ control for a Fly-UPS system is investigated.

At present, the Fly-UPS system is being controlled by a number of decentralized single-input single-output (SISO), PD controllers. Ultimately, the combination of a multivariable plant, inherent instability, model uncertainties, cross-coupled stiffness, high rotational speed as well as external disturbances, calls for the development of a multivariable robust H_∞ controller. The aim of H_∞ control is to compute a controller such that the modelling uncertainties, noise and disturbances are minimized according to predefined performance and robustness requirements.

A state-space model of both the radial AMBs and the axial AMB of the Fly-UPS system is developed and modelled according to the parameters of the physical rotor system. The sensors, power amplifiers and anti-aliasing filters are modelled and cascaded onto the rotor model. Finally, the system response is evaluated whereby the developed multivariable model is verified and validated.

In the context of robust H_∞ control, it is vital in specifying the uncertainty bound (difference weighting function) between the mathematical model and physical system in order to ascertain stability robustness. Thus, the additive uncertainties between the nominal simulation model and the physical model at varied rotational speeds are characterised. Furthermore, the mixed sensitivity H_∞ control synthesis strategy is described. Different weighting schemes are explained and the *six block problem* weighting scheme is used for H_∞ controller synthesis. A multivariable controller is synthesised with weighting functions relevant to the AMB Fly-UPS system and the controller is reduced to a 19th order controller for implementation.

The controller is implemented on the physical Fly-UPS system and the experimental performance of the H_∞ controller is verified and validated. The synthesised controller proves stability robustness against rotational speed variation by providing stable system responses for all axes of freedom. It also robustly tolerates a rotational speed variation of up to 6400 r/min with a large gain/phase margin. Furthermore, the controller performance is evaluated according to the proposed ISO CD 14839-3 standard. The controller is unable to successfully comply with the performance sensitivity specifications due to controller order reduction, synchronous unbalance and cyclic oscillatory behaviour. Finally, the results obtained are compared to the previous PD controllers of the system and it is established that the H_∞ controller provides an improvement.

One of the setbacks of H_∞ control is that the weighting functions are chosen on a trial and error basis. Nonetheless, H_∞ control has the advantage that it provides a systematic and lucid design procedure as well as the ability to compensate for highly coupled multivariable systems, where in classical control the task of tuning the controller to compensate for multivariable systems is problematical. Therefore, robust H_∞ control design provides a systematic tool to develop a multivariable controller that provides performance and stability robustness, with the advantage of specifying and shaping the design requirement trade-offs.

This project may serve as the foundation for further investigation into the feasibility of advanced control algorithms when applied to the Fly-UPS AMB system.

Acknowledgements

It is impossible to thank all the people who contributed to my dissertation in some way. Nonetheless, I would like to mention a few people without whom this work would not have been possible:

I would first like to extend a very special thank you to my beautiful wife, Liezl. Your love and support kept me afloat throughout all the 'ups and downs' in this project. Thank you for believing in me and being there to share every experience with me. I love you.

My sincere thanks to my supervisors, Dr. Pieter van Vuuren and Prof. George van Schoor. Your guidance, time, dedication and valuable inputs were and are priceless. Thank you for placing your trust in me and making it possible for me to further my studies. It has been an honour and a privilege working with you both.

Furthermore, the financial assistance of the National Research Foundation (NRF) towards this research is hereby acknowledged. Opinions expressed and conclusions arrived at, are those of the author and are not necessarily to be attributed to the NRF.

I would like to thank Stefan Myburgh and Jan Janse van Rensburg for helping, guiding and assisting me throughout this project (and allowing me to tinker with their flywheel system). My thanks to all my colleagues in the McTronX group, your teamwork and kinship are valuable to me.

I would like to thank all my friends, Eugène, Jacques, Martin, Ryno, Luke and my brother and sister, who kept me sane at times when I got too 'academic'. And to all those I have not mentioned, I appreciate your support.

Finally, to my parents, Martin and Ansa Steyn, for making my studies possible and teaching me that I can accomplish anything I put my mind to. I appreciate your love, wisdom and guidance.

TABLE OF CONTENTS

LIST OF FIGURES

LIST OF TABLES

NOMENCLATURE

LIST OF ABBREVIATIONS

3-D	Three dimensional
AMB	Active magnetic bearing
DOF	Degrees-of-freedom
Fly-UPS	Flywheel uninterrupted power supply
GUI	Graphical user interface
H_∞	H-infinity
ISO	International Organization for Standardization
LFT	Linear fractional transformation
LPV	Linear parameter varying
LQG	Linear-quadratic Gaussian
LQR	Linear-quadratic regulator
LTI	Linear time invariant
MIMO	Multiple-input, multiple-output
MMF	Magneto-motive force
NWU	North-West University
PA	Power amplifier
PID	Proportional, integral and derivative
PMSM	Permanent magnet synchronous machine
P.O.	Percentage overshoot
PWM	Pulse-width modulation
RLS	Recursive least squares
SISO	Single-input, single-output
SVD	Singular value decomposition

LIST OF SYMBOLS

A_g	Air-gap surface area
B	Magnetic flux density
E	Stored energy
F/F_m	Electromagnetic force
g	Gravitational force
g_0	Air-gap size
G_a	Augmented/interconnected system
G_n	Nominal model
G_p	Perturbed model
H	Magnetic field intensity
$H(j\omega)$	Frequency response
i	Control current
I	Moment of inertia
i_0	Bias current
i_m	Electromagnetic coil current
k	Inertial constant
k_i	Force-current factor
k_s	Force-displacement factor
K_D	Derivative gain
K_I	Integral gain
K_P	Proportional gain
l	Length of flux path
L	Open loop transfer function
m/M	Rotor mass
N	Number of coil turns
r	Flywheel radius
V_D	Disturbance input
V_R	Reference input
W	Field energy
W_d	Disturbance weighting function
W_e	Error weighting function

W_r	Reference weighting function
W_u	Input weighting function
W_y	Output weighting function
W_Δ	Uncertainty weighting function
x, x_s,s_0	Rotor position
S	Sensitivity function
S_i	Input sensitivity
S_o	Output sensitivity
T	Complimentary sensitivity function
T_i	Input closed-loop transfer function
T_o	Output closed-loop transfer function
α	Constant multiplicative factor
δ	Perturbation
Δ	Uncertainty
γ	Condition number
μ_0	Permeability of free space
ω	Angular velocity
ϕ	Magnetic flux
ψ	Parameter values
σ	Singular value
θ	Magnetic pole angle

Chapter 1

Introduction

This chapter serves as an introduction to and motivation for this dissertation. The topic of the dissertation is briefly introduced and explained in this chapter, followed by the methods used to achieve the required outcome. Finally, the structure of the dissertation is provided.

1.1 Background

1.1.1 Introduction

With progress in technology and the industry, there is an ever increasing need for high precision bearings in rotating machinery [**1**]. Conventional ball bearings function by physically enclosing the rotor of rotational machinery. Furthermore, lubrication is required within ball bearings in order to reduce the effects of friction. However, there are many alternatives to ball bearing technology. One such alternative is the contact-free, actively controlled, electromagnetic bearing. Hence, conventional bearings in rotational applications can potentially be replaced by active magnetic bearings (AMBs) [**2**].

In this dissertation, AMBs are applied to the North-West University's (NWU) flywheel uninterrupted power supply (Fly-UPS) system. By utilizing AMBs for the Fly-UPS, a contact-free, lubrication-free and actively controllable bearing system is achieved. Alas, the inherently unstable nature and complexity[1] of the AMBs for the Fly-UPS necessitates sophisticated feedback control. By introducing an advanced control method such as H_∞ control to the AMBs of the Fly-UPS, robust control can be realized.

1.1.2 Active magnetic bearings

The subject of magnetic bearings has been researched and developed extensively in recent years, as a result, only a brief description of AMB functioning will be given. A basic magnetic bearing consists of an electromagnetic actuator, displacement sensor, controller and a power amplifier (PA). The functioning of an AMB is detailed in Figure 1.1-1. A sensor is

[1] Complexity, in this case, refers to the multiple-input, multiple-output (MIMO) nature, gyroscopic effects and cross-coupling of AMBs.

used to measure the displacement of the rotor from the centre reference point. A microprocessor, serving as the controller, derives a control signal from this measurement. This control reference is then supplied to a power amplifier which provides the appropriate current to the electromagnet. Finally, the electromagnet exerts force on the rotor, allowing the rotor to levitate. This whole cycle repeats continuously as a closed-loop system.

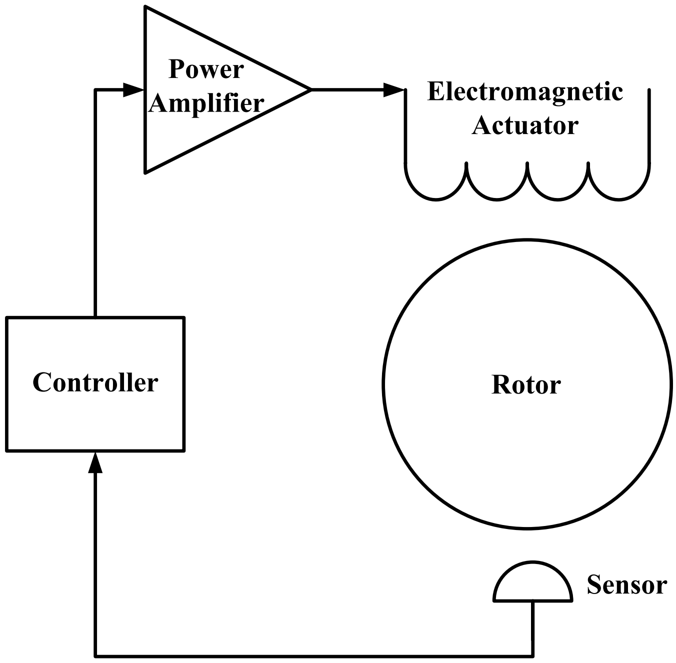

Figure 1.1-1: Basic AMB functional diagram [**6**]

1.1.3 Flywheel systems

Flywheel systems have long been used in the past and are still being used presently as an energy storage mechanism. In modern high-tech systems, flywheels are used as energy storage batteries or in this particular case, a Fly-UPS [**3**,**4**]. In the Fly-UPS, kinetic energy is stored in the rotational motion of the flywheel. The energy is supplied to the flywheel via an electric motor, and can be retrieved by changing the motor into a generator.

The disc shape of a flywheel makes the axial moment of inertia[2] of a flywheel greater than that of an elongated rotor of the same mass, making a flywheel an effective energy storage method [**3**]. However, due to a flywheel's higher moment of inertia, a flywheel rotor has lar-

[2] The axial moment of inertia is the resistance to change in a body's rotational velocity.

ger gyroscopic cross-coupling when compared to an elongated rotor. The rotor dynamics of a flywheel rotor are explained in section 2.3 and section 2.4.

The energy stored in a flywheel can be given by

$$E = \frac{1}{2} I \omega^2, \tag{1.1}$$

where I is the moment of inertia and ω is the angular velocity [**3**].

1.1.4 Control

AMBs are inherently open-loop unstable because of the inverse displacement-force relationship[3], and for this reason require closed-loop feedback control [**5**]. Without feedback control, the rotor will either cling to one side of the electromagnets, or oscillate between the electromagnets [**6**].

Ultimately, the combination of inherent instability, model uncertainties, cross-coupled[4] stiffness, high rotational speed, and critical speeds[5] call for the development of a multivariable robust controller [**7**]. Robust controllers are controllers that provide acceptable control over a larger range of implementations (systems) than standard controllers, either in performance or stability [**8**].

In robust control synthesis, the primary goal is to reduce the effects of model uncertainty, steady-state error, noise, and disturbances on system performance and stability [**9**]. A multivariable robust control technique such as H_∞ control adheres to the above mentioned objective [**10**]. The aim of H_∞ control is to compute a controller $\boldsymbol{K}$ such that the modelling uncertainties, noise and disturbances are minimized according to predefined performance requirements at low frequencies and robustness requirements at high frequencies [**11**,**12**]. In a study done by [**5**], it was found that H_∞ control on vertical AMBs, compared to LQR[6] or PID control, reduced the required control current and provided greater stability robustness with varying rotational speed. However, H_∞ control was found lacking in position deviation regulation when compared to optimal LQR control.

---

[3] Because the magnetic force decreases with an increase in distance by the inverse square law of distance: $F \sim 1/d^2$

[4] Cross-coupling represents the coupling between the *x*-*y* axes, as well as the upper - lower *x*-*x*, *y*-*y* axes.

[5] Critical speeds are dependent on and are sensitive to the rotor design.

[6] Linear Quadratic Regulation control minimises the control energy (see [**28**]).

By considering all of the above mentioned factors, the feasibility of multivariable H_∞ control for the Fly-UPS system is investigated.

1.2 Problem statement

The objective of this dissertation is to develop a multivariable robust H_∞ controller to replace the decentralized single-input, single-output (SISO), PD controllers of an active magnetic bearing flywheel system (Fly-UPS).

Because the Fly-UPS design is subject to various uncertainties as well as gyroscopic effects at varying rotational speeds, *stability robustness* is a primary feedback requirement. Additionally, having sufficient disturbance attenuation over varying rotational speed is a major *performance robustness* requirement. Thus the additional requirements are:

- Robust stability by having large gain/phase margins during speed variation.
- Robust performance via sufficient disturbance rejection and good system response.

1.3 Issues to be addressed

The following issues are addressed in the dissertation:

- **System modelling.** A mathematical state-space model of the Fly-UPS system is developed. The sensors, power amplifiers (PAs) and anti-aliasing filters are designed and specified. Furthermore the model is verified and validated.

- **H_∞ control theory and design.** The controller is synthesized using the state-space model developed, thus characterization and inclusion of uncertainties within the Fly-UPS model is of great importance [**1**]. An investigation into H_∞ control theory is done, in order to decide which H_∞ control method to use for controller synthesis. After the investigation, an H_∞ controller is designed in order to control the Fly-UPS.

- **Implementation.** The H_∞ controller is implemented on the mathematical model of the Fly-UPS in order to make theoretical predictions. The controller is then implemented on the physical Fly-UPS system. Both simulation and physical implementations are monitored and recorded for evaluation purposes.

- **Verification and validation.** The accuracy of the mathematical model as well as the controller synthesis and final design are verified and validated. Moreover, the mathematical model is validated from the physical implementation test data.

- **Evaluation and conclusion.** The closed-loop system stability robustness is analyzed. In addition, the system performance robustness is measured and evaluated according to the proposed ISO standard. The implemented H_∞ controller is compared to the PD control strategy using the same evaluation methods. Finally, recommendations for further work are made.

1.4 Methodology

This section describes the methods used in addressing each of the above mentioned issues.

1.4.1 Literature study

The field of AMBs are studied in order to develop a model that represents the Fly-UPS system. Modelling uncertainties are also studied thoroughly. The field of H_∞ control theory is studied, as an in depth understanding of H_∞ control is required in order to choose a control synthesis method and successfully develop the H_∞ controller. Finally, physical implementation methods are researched. This literature study is briefly documented in Chapter 2 of the dissertation and relevantly extended in more detail in each subsequent chapter.

1.4.2 System modelling

A mathematical state-space model of the rigid-rotor Fly-UPS plant is developed using parameters from the existing Fly-UPS system. MATLAB® software is the development environment, as it has the required computational functionality.

All the AMBs in the Fly-UPS are modelled, including the power amplifiers, filters and sensors. The gyroscopic characteristics are included in the model using the rotor's inertial properties. Furthermore, including modelling uncertainties (modelling errors) in the mathematical model is the key to successful robust H_∞ control design [**13**]. Unfortunately, characterising uncertainties is not a trivial procedure and different types of uncertainty structures will be considered.

1.4.3 H_∞ control theory and design

An investigation into H_∞ control theory is done in order to decide which H_∞ control method to use for controller synthesis. The two basic design approaches considered are open-loop transfer function loop shaping and closed-loop transfer function loop shaping [**10**]. In loop shaping, the required shape of a transfer function is defined in the frequency domain using singular values (see Appendix A), and a controller is designed to shape the system transfer function into that required shape [**2**].

By adhering to open-loop design objectives, it is relatively easy to estimate the closed-loop requirements over specific frequencies [**10**]. But, because the Fly-UPS AMBs are open-loop unstable, specifying an open-loop shape is relatively difficult. Consequently, closed-loop transfer function design in mixed sensitivity H_∞ control synthesis is the primary focus of this dissertation [**2**]. This allows robust stability by including uncertainties in the model as well as providing robust performance by minimizing the H_∞ norm via weighting [**14**].

1.4.4 Implementation

Firstly, the synthesized H_∞ controller is implemented on the mathematical model of the Fly-UPS. From this simulation, certain theoretical predictions concerning the system response, closed-loop system stability and sensitivity functions of the physical system are made which provides useful insight on the projected physical implementation results. This helps in validating and verifying the accuracy of the H_∞ controller and the mathematical model.

Lastly the developed multivariable H_∞ controller, is implemented on the physical system utilising a dSPACE® card. The dSPACE® card interfaces the Simulink® environment with the physical hardware by means of input-output data cables. The controller is implemented on a workstation computer at the NWU's Magnetic Bearing Laboratory. This computer is already connected to the Fly-UPS via dSPACE®, therefore, only the MATLAB® and Simulink® environments are used to develop and implement the H_∞ controller.

1.4.5 Verification and validation

Verification and validation is done throughout each subsequent chapter. For instance, in the system modelling chapter, the nominal mathematical model is verified and validated by comparing step responses between the mathematical and physical systems. The H_∞ controller is verified in the implementation chapter, when the simulation results are compared to the physical implementation test data.

1.4.6 Evaluation and conclusion

The position of the Fly-UPS rotor is logged via the ControlDesk® graphical user interface (GUI). Initially, the stability robustness is evaluated by analyzing the closed-loop system stability during specified rotational speed variations. The gain and phase margins are evaluated in order to examine whether the synthesised control-loop guarantees closed-loop stability robustness. Secondly, the system performance robustness in having sufficient disturbance rejection is evaluated via the sensitivity function. The sensitivity function is obtained by feeding a sinusoidal signal into each separate rotor input over a predefined frequency range [**15**]. The magnitude of the response of the rotor due to the signal provides the sensitivity function. The AMB performance is finally evaluated according to the ISO/CD 14839-3 standard [**4**].

In conclusion, the implemented H_∞ controller is compared to the popular AMB suspension control strategy, namely PD control. Finally, recommendations for further work are made, depending on the evaluated results.

1.5 Dissertation overview

Chapter 2 consists of a brief background on AMBs, flywheels, AMBs applied to flywheels and the control thereof. This chapter will elaborate on the Fly-UPS system to be modelled and the system on which the controller will be implemented.

An in-depth study on developing a mathematical model of the Fly-UPS system is discussed and developed in Chapter 3. The AMBs, power amplifiers, filters and sensors are discussed and modelled. The model developed in this chapter will be used to synthesise the robust controller.

An in-depth study on robust control and H_∞ control is done in Chapter 4. Plant uncertainties are discussed and characterised. Furthermore, the different H_∞ control development methods are discussed here. The different weighting schemes relevant to H_∞ control are also discussed. Finally, a specific H_∞ controller is synthesised.

Chapter 5 explains how the H_∞ controller is implemented on the physical system. Results from the implementation are acquired, analysed and characterized in this chapter. The sensitivity function, closed-loop stability margin as well as system response graphs are given.

Finally, in Chapter 6, a conclusion is drawn regarding the results and recommendations are made for further study.

The Appendices A, B, C, D and E contain the mathematical notations, mathematical equations, model state-space matrices, photographs of the Fly-UPS system and research publications respectively. Furthermore, footnotes will be used to explain specific definitions, terms and concepts.

1.6 Publication status of research

The research done within this dissertation was presented at two conferences, namely:

- Southern African Universities Power Electronics Conference (SAUPEC 2010).
- United Kingdom Automation and Control Conference (UKACC 2010).

These articles were published within the following conference proceedings (Appendix E):

S. J. M Steyn, P. A. Van Vuuren, and G. van Schoor, "Multivariable H_∞ Control for an LTI Active Magnetic Bearing Flywheel System," in *Proceedings of the 19th Southern African Universities Power Engineering Conference*, Johannesburg, South-Africa, January 28-29, 2010, pp. 100-106.

S. J. M Steyn, P. A. Van Vuuren, and G. van Schoor, "Multivariable H_∞ Control for an Active Magnetic Bearing Flywheel System," in *Proceedings of the UKACC International Conference on CONTROL 2010*, Coventry, United Kingdom, September 7-10, 2010, pp. 1014-1019.

1.7 Conclusion

This chapter briefly explains the functioning and control of AMBs. The problem statement is defined followed by the issues to be addressed, methodology and an overview of the proposed dissertation. This chapter, as a whole, serves as an introduction to the development of an H_∞ controller for an AMB system with application to the Fly-UPS. The next chapter will present an overview on AMBs, flywheels, the application of AMBs to the Fly-UPS system and finally a short summary on robust control.

Chapter 2

Flywheel AMB system: a brief overview

This chapter provides a literature study on the field of AMBs, flywheels and AMB control. Initially, AMBs and their applications are explained, followed by flywheels in general. The application of AMBs to the Fly-UPS system is then explained. Finally, a brief overview of robust control is given.

2.1 Active magnetic bearings (AMBs)

2.1.1 Introduction

Bearings are some of the most crucial components in rotating machinery [**3**]. Bearings are usually static, making them part of the stationary (stator) components used to support the moving part (rotor) of the machine. For simple rotational applications, ball bearings are most commonly used, although in more complex machines that require multi-degree-of-freedom motion, air and fluid bearings can be used. Unfortunately, ball bearings require lubrication, increasing the possibility of system failure due to contaminated lubrication or lubrication thermal breakdown.

An alternative to ball bearings are active magnetic bearings (AMBs). AMBs are typical mechatronic products that use magnetic energy properties in order to replicate the physical characteristics of ball bearings [**6**]. By applying controlled magnetic force on a rotor via AMBs, a rotor can levitate and spin without touching the stator, eliminating contact friction entirely. Applications for AMBs are thus emerging in high speed and high performance technology such as turbo-machines, centrifuges, motors, machining spindles, and flywheels [**2**]. With recent advances in power electronics, AMBs can be developed and implemented with little external hardware allowing for smaller applications [**3**].

The following section does not intend to provide extensive background on AMBs, as AMBs have been extensively documented in literature such as [**4**] and [**6**]. Only a basic introduction to AMBs and their functioning will be provided.

2.1.2 Basic force classification

The magnetic subsystem of the AMB, shown in Figure 2.1-1, is usually fabricated from magnetic material such as silicon steel. It has an air gap with thickness, g_0, and a surface area of A_g. The magnetic flux is generated by the coil which has N number of turns and current, i_m, flowing through it. The product $N \cdot i_m$ is called the magneto-motive force (MMF). The length, l, of the flux path extends through the magnet, the air gap, as well as the rotor.

Ampere's circuital law states: the magnetic field intensity, H, induced by N number of turns in a wire, carrying current, i_m, around a path of length, l, is given by [**4**]

$$H = \frac{Ni_m}{l} \text{ [A•turns/m]}. \tag{2.1}$$

The magnetic flux, ϕ, is simply the product of the magnetic flux density, B, and the area A_g,

$$\phi = B \bullet A_g \text{ [N•m/A]}. \tag{2.2}$$

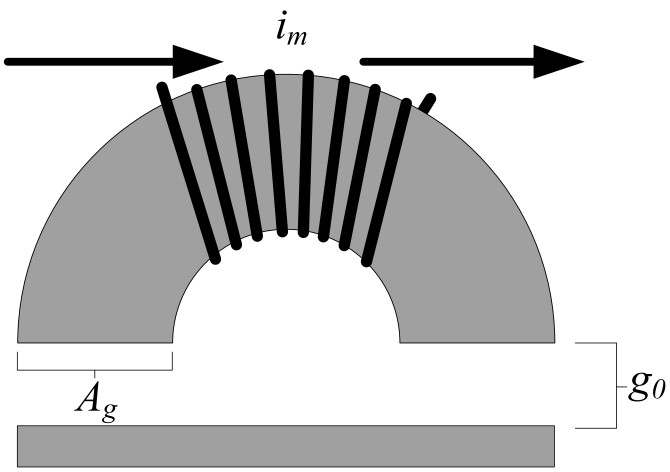

Figure 2.1-1: Basic electromagnetic geometry [**28**]

Furthermore, the flux density, B, is a linear function of the magnetic field intensity, H,

$$B = \mu_0 \bullet H \text{ [Wb/m}^2\text{]}, \tag{2.3}$$

where the permeability of free space is given by,

$$\mu_0 = 4\pi \times 10^{-7} \text{ [H/m]}. \tag{2.4}$$

Thus by substituting (2.1) into (2.3) and assuming $l = 2g_0$ [**4**], and that no MMF is lost, the flux density can be given in terms of N number of wire turns and current, i_m,

$$B = \frac{\mu_0 N i_m}{2g_0} \text{ [Wb/m}^2\text{]}. \tag{2.5}$$

The electromagnet's attractive force is determined by taking the partial derivative of the field energy, W,

$$W = \frac{1}{2} B H A_g 2g_o \tag{2.6}$$

in terms of the air gap, g_0, to acquire:

$$F_m = \frac{dW}{dg_0} = BHA_g = \frac{B^2 A_g}{\mu_0}. \tag{2.7}$$

Hence, by substituting (2.5) into (2.7), the attractive force is represented in terms of coil current and air gap,

$$F_m = \frac{\mu_0 N^2 i_m^{\ 2} A_g}{4 g_o^{\ 2}} \text{ [N]}. \tag{2.8}$$

However, in reality, there are effects such as fringing and leakage in magnetic circuits which are not included in the above modeling procedure. In addition, in the case of heteropolar geometry, the magnet poles are angled at $\theta = 22.5°$ with respect to the vertical axis (see Figure 2.1-2). So, in order to compensate for the fringing and leakage, (2.8) may be scaled with a constant factor $\alpha = 0.9$, and in order to compensate for the angled poles, further scaling is included [**16**,**4**]:

$$F_m = \alpha \frac{\mu_0 N^2 i_m^{\ 2} A_g}{4 g_o^{\ 2}} \cos(\theta) \left(\frac{\sin\left(\frac{\theta}{2}\right)}{\left(\frac{\theta}{2}\right)} \right)^2 \text{ [N]}. \tag{2.9}$$

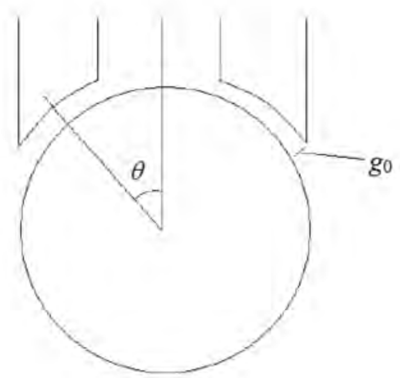

Figure 2.1-2: Heteropolar geometry of an AMB.

The generated electromagnetic force in (2.9) is directly proportional to the square of the coil current and indirectly proportional to the square of the air gap. Hence, the AMB system is a non-linear system with negative position stiffness and is open-loop unstable[7]. For stable rotor suspension, feedback control of the electromagnetic force is required.

The total force on the rotor should ensure that an equilibrium position is maintained. Equilibrium is reached when the sum of the forces acting on the rotor is equal to zero. In the case of a horizontal rotor, the only forces acting on the rotor are gravity, *mg*, and the magnetic force, F_m (Figure 2.1-3). The resultant force, *F*, applied to the object is given by:

$$F = F_m - mg. \tag{2.10}$$

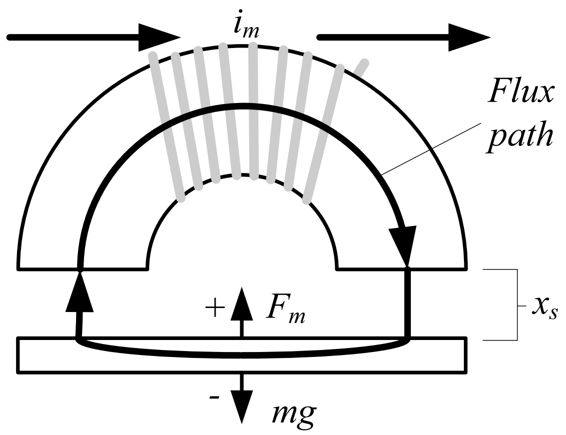

Figure 2.1-3: Forces exerted on an object to achieve equilibrium position

By continuously monitoring the equilibrium position, any deviation from equilibrium can be restored by adjusting the power amplifier outputs. This equilibrium position is called an operating point, or set-point. The current and displacement are both referenced around this operating point. By using a controller that only considers the slopes of the non-linear force-current and force-displacement curves at and around the set-point, the system is linearised (Figure 2.1-4).

This linearised force-current is shown in Figure 2.1-4 (a). A new term, *i*, is introduced in (2.11) which represents the change in the coil current, i_m, from the operating point i_0.

$$i = i_m - i_0 \text{ [A]}. \tag{2.11}$$

[7] Because the magnetic force increases with a decrease in distance by the inverse square law of distance: $F \sim 1/x^2$

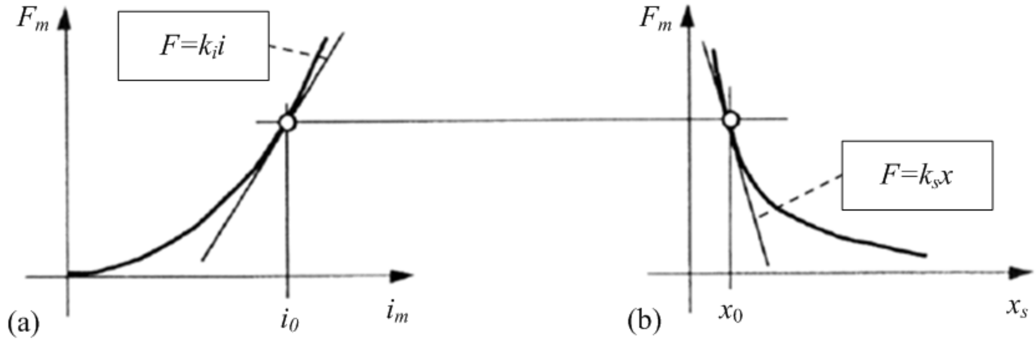

Figure 2.1-4: Magnetic force in terms of (a) current and (b) air gap [**6**]

The slope of the force-current function, *F(i)*, is the force-current factor, k_i, measured in Newton/Ampere (N/A). Likewise, linearised force-displacement function, *F(x)*, is shown in Figure 2.1-4 (b). Once again a new variable, x, is introduced which represents the change in displacement, x_s, from the operating point $x_0 = g_0$. It should be noted that positive displacement is assumed towards the magnet, implying positive values for k_s.

$$x = x_0 - x_s \text{ [m].} \tag{2.12}$$

The slope of *F(x)* is the force-displacement factor, k_s, measured in Newton/meter (N/m), similar to mechanical stiffness. As a result, the three variables, force, displacement and current, have constant operating point values (mg, x_0, i_0) as well as variables representing deviation from these operating points (F, x, i).

Finally, the resulting force acting on the rotor or object has been linearised in terms of displacement and current giving the equation for total instantaneous force in the operating point as:

$$F(x,i) = k_s x + k_i i \text{ [N].} \tag{2.13}$$

The values for k_s and k_i, are obtained by taking the partial derivative of the non-linear force equation (2.9) with respect to current and displacement at the operating point. Further explanation on the partial derivative of the non-linear force equation and the forces acting on a vertical rotor suspended by two electromagnets will be given in Chapter 3.

2.2 Advantages and drawbacks of AMBs

AMBs have many advantages because they support the rotor shaft using actively controlled magnetic fields and not conventional mechanical methods such as liquid or ball bearings. Because AMB suspended systems have no contaminating wear, they are ideal for vacuum techniques, such as in clean, sterile rooms or for the transportation of sensitive or radioactive material [**6**]. In addition, AMBs have a long lifetime. This reduces the required periodic maintenance, minimizing maintenance costs. Furthermore, the active feedback control nature of the AMB system, allows the adaptation of the system damping and stiffness characteristics [**3**,**11**]. Hence, AMB systems require no lubricant, allows a rotor to rotate without touching the stator as well as providing control of the rotor dynamics through the bearings [**6**].

Another advantage of AMB systems is the reduced dependence on environmental conditions. AMBs can run at much higher and lower temperatures compared to conventional bearings [**2**]. In addition, AMBs provide measurement information for the control process. This information can be used to determine any unbalances, vibrations or potential bearing failure. By providing on-line diagnosis, the reliability of the system can be increased [**2**].

Unfortunately, AMB systems do have some drawbacks. AMB systems are expensive due to their special applications and their complexity[8]. The complexity of AMB systems require well trained personnel for installation, running and maintenance [**6**]. Hence, the initial cost is large, but is compensated for by the longer lifespan and lower maintenance cost.

In addition, the loss of levitation of AMB systems during a power failure is another limitation [**16**]. To overcome this problem, conventional bearings are implemented as retainer bearings in case of such a power failure. These retainer bearings have a small clearance between them and the rotor, and thus only function during loss of levitation [**2**]. The effects of such a loss of levitation on the retainer bearings cannot be neglected as it can cause damage, vibrations and other system instabilities. Thus, an understanding of the rotor dynamics during touch-down is required for useful retainer bearing design [**6**].

[8] AMBs are a combination of mechanics, electronics and control.

There are some challenges and features of AMBs that are fundamental in successful field implementation which should be taken into consideration, especially when considering controller design [**2**]:

- AMBs are open loop unstable, requiring *feedback control*. Physically implementing such feedback control is a substantial challenge.
- AMBs in field applications are subject to *uncertainties*[9]; making *robustness* a primary requirement.
- AMBs are *multivariable* due to gyroscopic coupling, cross-coupled[10] stiffness and other structural interactions. From this, the challenge of multivariable (MIMO) control arises.
- The characteristics and dynamics of rotational application AMBs are rotational speed dependent. Gyroscopic effects, internal damping and centrifugal stiffening all influence the system dynamics. This not only complicates system dynamics, it complicates the control procedure.
- The AMB force current relationship is non-linear, making the implementation of a single AMB specific to a single application.

As a result of the above challenges, the feasibility of developing a multivariable robust H_∞ controller is substantiated and will be elaborated in section 2.5.

2.3 Flywheels

In the NWU's Fly-UPS system, AMB's are applied to an energy storage flywheel system. The reason a flywheel system is used is because it allows storage of rotational energy. It usually consists of a disc, mounted on an axle which can be rotated. Kinetic energy is stored and harnessed using a motor/generator setup. The flywheel is excited using a motor, reaching high rotational velocity. This rotation stores kinetic energy. The generator setup is then used to convert the stored kinetic energy back into electrical energy, and as a result, the rotational speed of the flywheel is reduced. Because a flywheel has a disc shape (see Table 2.3-1) it has a higher moment of inertia[11] when compared to an elongated rotor of the same mass [**3**].

---

[9] Uncertainty is the dynamic or static deviation of the mathematical system from the physical system.
[10] Cross-coupling represents the coupling between the *x*-*y* axes, as well as the upper - lower *x*-*x*, *y*-*y* axes.
[11] The axial moment of inertia is the resistance to change in a body's rotational velocity.

Table 2.3-1: Various flywheel shapes and inertial constants [**4**]

Flywheel geometry	Cross section	Shape factor *k*
Disc		1.000
Conical disc		0.806
Flat unpierced disc		0.606
Thin film		0.500
Rim with web		0.400
Flat pierced bar		0.305

The energy stored in a flywheel is given by the formula

$$E = \frac{1}{2} I \omega^2 \text{ [J]}, \tag{2.14}$$

where I is the moment of inertia and ω is the angular velocity [**3**,**4**]. It can then be deduced that if two bodies have the same angular velocity, more energy will be stored in the body with the higher moment of inertia.

The moment of inertia for a flywheel is calculated using

$$I = k \bullet M \bullet r^2 \text{ [kg.m}^2\text{]} \tag{2.15}$$

where r is the flywheel radius and M the mass. The inertial constant k is dependent on the flywheel disc shape, as seen in Table 2.3-1.

Flywheels have a high power density as well as a high energy density. This entails that flywheels can supply a high power for a longer period of time when compared to capacitors or batteries (see Figure 2.3-1) [**4**]. A flywheel battery falls in the same energy storage device group as a super capacitor [**3**].

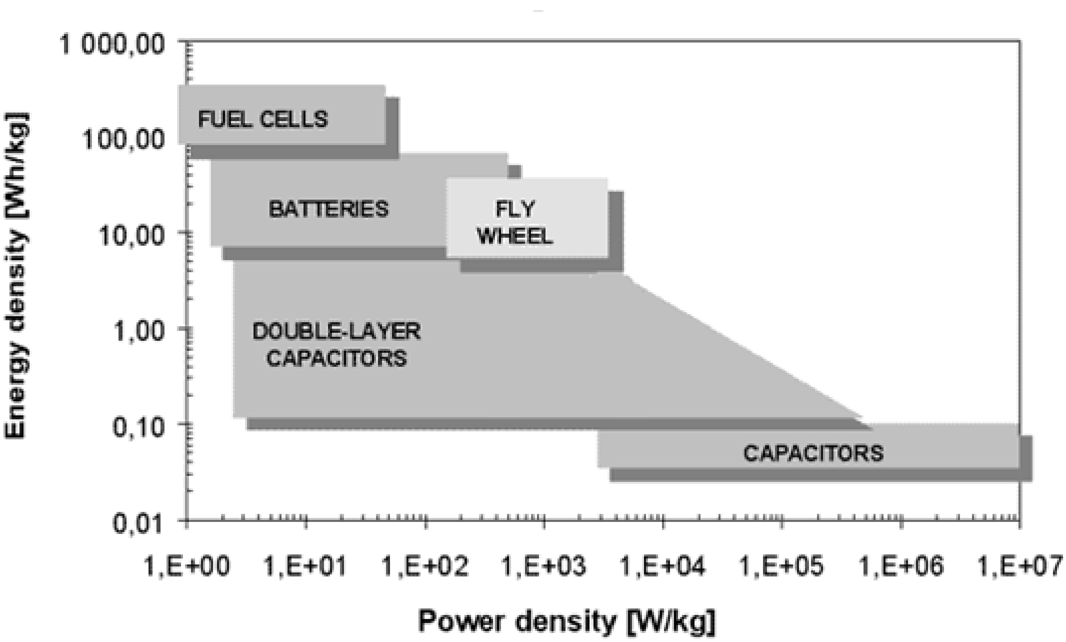

Figure 2.3-1: Power and energy density of various storage methods [**30**]

An example of a flywheel system is given in [**17**], where it is applied to a hybrid electric bus. The energy generated during braking is stored in the flywheel and then used when the bus accelerates again. A flywheel can also be used to provide power during the transition between a power outage and the back-up generator powering up [**4**].

2.4 AMB's applied to the Fly-UPS

In modern high-tech systems, flywheels are used as energy storage batteries [**3**]. In this particular case AMBs are applied to a flywheel uninterrupted power supply (Fly-UPS) system [**4**]. By utilizing AMBs for the Fly-UPS, a contact- and lubrication-free ideal vacuum environment is achieved [**18**]. However, when implementing AMBs on a Fly-UPS, the rotor dynamics must be considered. These rotor dynamics include: gyroscopic forces[12], resonance phenomena[13] and natural vibrations [**6**].

[12] Gyroscopic forces include forward whirl and backward whirl.
[13] Resonance phenomena, caused by unbalances in the rotor, occur at critical speeds and lead to vibration in the rotor. More on gyroscopic forces and resonance phenomena can be found in [**6**].

In order to suspend a rotor, such as the Fly-UPS, two four-poled[14] AMBs are required [**3**]. These AMBs are called radial AMBs and suspend the rotor in the two rotor x and y directions. A third axial AMB is required in order to suspend the rotor along the rotor z axis (Figure 2.4-1a).

A digital 3-D model of the Fly-UPS energy storage flywheel system with the axial bearings, radial bearings and motor/generator can be seen in Figure 2.4-1b. Figure 2.4-1b shows the upper and lower axial AMBs, the two eddy current probes, the upper and lower radial AMBs, the rotor/flywheel assembly as well as the permanent magnet synchronous machine (PMSM). The enclosure of the Fly-UPS is made of aluminium and is bolted onto a concrete floor.

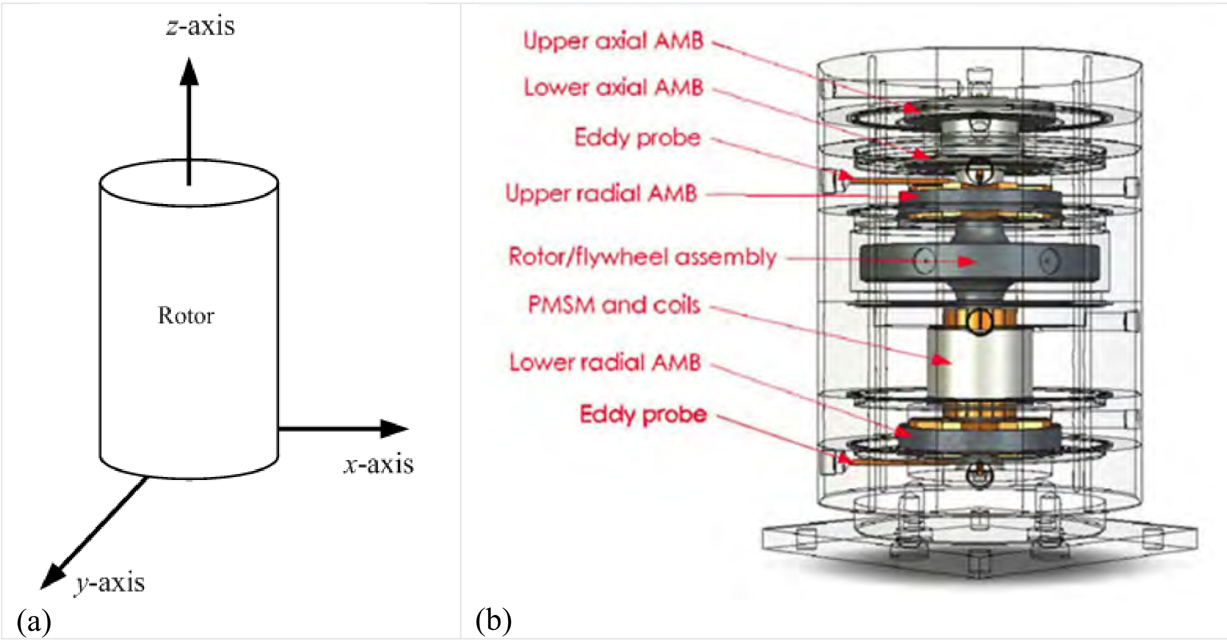

Figure 2.4-1: (a) Fly-UPS orientation and (b) digital Fly-UPS model [**22**]

2.5 Control

In order to fully suspend a rotor, it must be stabilised at its force equilibrium point (as stated in section 2.1). This equilibrium point is the position where the sum of the forces applied to the rotor is zero [**6**]. An open loop controller cannot provide correcting feedback, because the system requires knowledge of the output position, in order to change the magnitude of the

[14] A single electromagnet can provide either positive or negative directional force. Two electromagnets are required per axis, one to provide positive force and one to provide negative force. Thus, four electromagnets are required to suspend one side of a rotor in both directional axes.

force applied by the power amplifiers. Feedback control to manipulate the force acting on the rotor is important because the electromagnet aims to reduce the reluctance of the air gap, pulling the rotor closer (2.9). It is thus clear that AMB systems are open-loop unstable [**1**,**2**,**3**,**6**,**11**]. To enable the stable equilibrium state to be reached and maintained, a closed-loop controller should use the sensor measurement to manipulate the force acting on the rotor.

In section 2.1, the system explained is a single-input, single-output system. For the Fly-UPS, there are more than one input and output. The inputs to the system are the force control currents (2.11), on the bearings in the *x*, *y* and *z* axes. The outputs are the displacements (2.12) in the *x*, *y* and *z* axes.

At present, the Fly-UPS system is being controlled by a number of single-input, single-output (SISO) PD[15] controllers in parallel. These decentralized PD controllers are decoupled from one another, with each one controlling a directional axis. Decentralized control does not always provide acceptable performance and robustness, because the Fly-UPS system is inherently a MIMO system, prone to gyroscopic effects, multivariable cross-coupling[16] and speed dependent dynamics [**2**]. These MIMO characteristics of the Fly-UPS call for the development of a centralized multivariable controller that maintains stability robustness and performance robustness[17]. In addition, MIMO control allows each combination of input and output pairs to have individual gains and transfer functions [4]. Furthermore, *robust* MIMO control allows the inclusion of perturbations between the nominal system model and the physical plant via uncertainty weighting. H_∞ control is one such MIMO robust control method [**10**].

H_∞ control has successfully been applied to different AMB systems in [**1**,**2**,**5**,**11**]. In [**1**], H_∞ control was applied to an AMB *hard disk drive*, mainly to improve disturbance rejection. The H_∞ controller successfully complied with the servo specifications, but was only partially tested on the system due to hardware bandwidth limitations. Furthermore, in [**2**] and [**11**], H_∞ control was implemented on a simple *four degree of freedom* AMB *flexible cylindrical rotor*. In [**2**], H_∞ control was compared to μ-synthesis control and the μ-synthesis control proved superior to H_∞ control when implemented on a flexible rotor system. In [**11**], model error

[15] A controller with proportional, integral and derivative gains and the transfer function $G_c(s) = K_p + K_D s$ [**14**].

[16] Cross-coupling represents the coupling between the *x*-*y* axes, as well as the upper - lower *x*-*x*, *y*-*y* axes.

[17] Robust stability by having large gain/phase margins during speed variation and robust performance via sufficient disturbance rejection and good system response.

modelling and confidence interval networks were used to estimate the system uncertainty. Finally, in [**5**], H_∞ control was implemented on a four degree of freedom *cylindrical* rigid rotor. The H_∞ controller was found lacking in position deviation regulation when compared to optimal LQR control, but H_∞ control showed reduced control current and provided greater stability robustness with varying rotational speed. Using similarities and contributions from the above cases, the effectiveness of H_∞ control on a *five degree of freedom*, *rigid flywheel disc* rotor system will be investigated in this dissertation. It should be noted that H_∞ control is a model based control synthesis method. In addition, the weighting functions used are chosen on a trial and error basis. This model based control design, in addition to the trial and error selection of weighting functions, necessitates that H_∞ control be evaluated specific to the Fly-UPS.

Extensive literature on multivariable robust control and the applications thereof can be found in [**10**,**12**,**14**] and [**19**]. Therefore the preceding section is not intended as a comprehensive literature study on the complete field of robust H_∞ control. More detailed background on robust H_∞ control with application to the Fly-UPS will be given in Chapter 4.

2.6 Conclusion

Thus in conclusion, this chapter provides a brief overview of the Fly-UPS system as a whole, its substructures, and the control required for such a system. However, more detailed literature on the modelling of such a system, as well as robust H_∞ control will be supplied in each subsequent chapter. Therefore, in order to contextualise:

- AMB systems require control in order to function.
- Robust control allows compensating for perturbations between the physical AMB system and the simulation model.
- H_∞ control is part of the robust control family.
- A model of the Fly-UPS system is required in order to characterise the uncertainties.
- H_∞ control is synthesised from a mathematical model, requiring that such a model be derived.

Henceforth, modelling of the Fly-UPS will be studied, discussed and developed in Chapter 3, followed by the study of robust control, uncertainties and development of an H_∞ controller for the Fly-UPS in Chapter 4.

Chapter 3

Modelling

The modelling of the AMB Fly-UPS system is explained in detail in this chapter. Initially, a brief background on modelling is given. Then the Fly-UPS is modelled according to the parameters of the physical system. Finally, the sensors, power amplifiers and anti-aliasing filters are added onto the model and the system is verified and validated.

3.1 Background

Modelling is a method for mathematically describing the behaviour of a system[18] [**1**]. The purpose of modelling is usually to find a relationship between the input, *u* and the output, *y* of a system. However, real processes are non-linear, requiring accurate modelling in order to represent the non-linearity. Fortunately, if the system is mostly operated around or within the same set point, the system can be linearised [**6**]. Linearisation simplifies the model allowing for easier analysis as well as easier controller development, which is further supported by the large number of linear controller development methods available [**2**].

There are basically two types of modelling (Figure 3.1-1), each with its own subsequent acquisition method: Firstly, analytical modelling is the process of applying mathematical equations and laws to a system in order to explain the system dynamics. Transfer function modelling represents the Laplace transform of the output variable to the Laplace transform of the input variable, with all initial conditions at zero [**20**]. In the case of state variable models, the model consists of a structure, parameters and a state vector [**1**]:

- Structure- These are the mathematical equations.
- Parameters- These are the constants.
- States- These are usually the variables of the equations.

Thus, by using an analytical model[19], a greater understanding and study of the physics of the system can be achieved [**1**].

[18] In this case the AMB Fly-UPS is the system to be modelled.
[19] The states and parameters all have physical meaning and units.

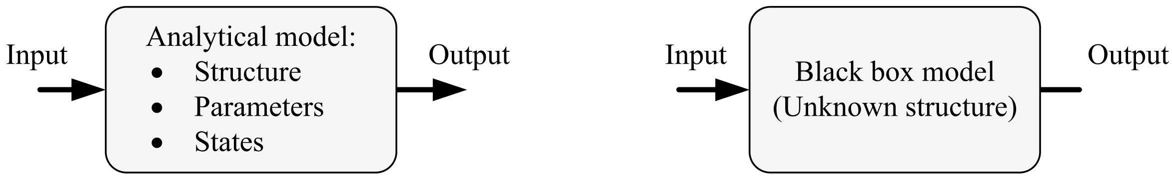

Figure 3.1-1: Comparison between analytical and black box models.

The second modelling type is called black box modelling (system identification). This type of modelling is solely concerned with observing the inputs and outputs of a physical system. There is no real interest in the physics or parameters of the system, only the relation between the inputs and the outputs of the system during a specified time frame. By measuring the inputs and outputs of the physical system within a certain time frame, a representative model for the system is extracted [**1**]. There are many different methods of system identification such as: model error modelling (MEM), recursive least squares (RLS), linear autoregressive with exogenous input (ARX) or artificial neural networks. These system identification methods are explained in [**11**] and [**21**].

Normally, system models are represented in either time domain or frequency domain. The frequency domain describes the frequency spectra of the input to the output. Whereas the time domain is the state space relation between the input and the output by making the present output a function of the previous input and output.

Both analytical and black box modelling methods are used in this dissertation. The system model is designed using the analytical method in this chapter and the uncertainty is characterised using a modified black box system identification method in Chapter 4.

3.2 Model development

This section will use the analytical method (based on the method used in [**6**]) to develop and describe the five degrees of freedom (5-DOF) AMB Fly-UPS. The five degrees of freedom are the radial x and y directions for the top ('b') and bottom ('a') AMBs and the axial, z, direction (Figure 3.2-1). The model is able to represent the dynamic behaviour of the Fly-UPS within small deviations from the nominal values. The rotor displacement, gyroscopic coupling, coil currents, power amplifier bandwidth as well as sensor bandwidth are all represented within this model [**18**].

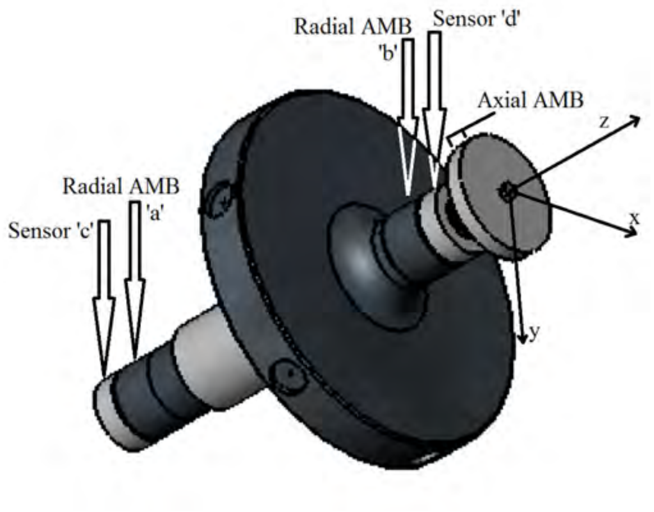

Figure 3.2-1: Fly-UPS rotor [**22**].

Some effects are not represented, such as rotor touchdown during a power failure as well as rotor whirls due to their nonlinear nature [**6**]. Furthermore, the model represents a rigid rotor and thus rotor bending modes are not modelled. Due to the linear set of connected rigid elements, the mathematical model results in a set of second-order differential equations.

In general, the dynamic behaviour of rotors can be represented using linear time invariant differential equations. Although it depends on limiting suppositions being made, namely [**7**]:

- Small rotor displacements.
- Rotationally symmetric rotor.
- Constant rotational speed.
- Radial (x and y) displacements are decoupled from axial (z) displacements.
- External forces and measurements are taken from discrete locations.

Figure 3.2-2 below, shows the basic design of the system model. The sensors measure the displacements of the rotor, which are fed via analogue-to-digital converters (ADCs) to the controller. The controller returns the current control signal via digital-to-analogue converters (DACs) to the power amplifiers that feed the actuators to produce the magnetic force. This creates the closed loop AMB system.

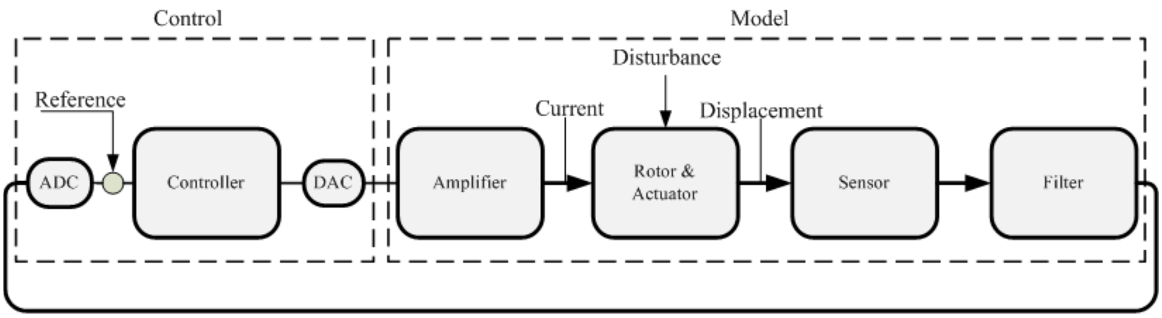

Figure 3.2-2: Full closed-loop design of the Fly-UPS system.

3.2.1 Linear state-space model

Chapter 2 provided insight into the basic magnetic force classification of AMB systems, but for the sake of completeness a brief review is now presented. The supposition that the radial and axial AMBs are modelled separately should be noted again. Initially, the focus will be on modelling the radial AMBs, with a separate section for modelling and adding the axial AMB.

3.2.1.1 Force model

The force of the AMBs acting on the rotor is based on the simple model shown in Figure 3.2-3 (a). A ferromagnetic horseshoe magnet with cross-sectional area A_g, and input current i_m, will exert a reluctance force of F on a metal object [**6**]. If the metal object is at a distance x_0 from the magnet, the force exerted on the object will be proportional to the square of the current and inversely proportional to the square of the distance,

$$F = K\left(\frac{i_m}{x_0}\right)^2, \forall x_0 > 0 \tag{3.1}$$

where

$$K = \frac{1}{4}\mu_0 N^2 A_g \cos(\theta). \tag{3.2}$$

N represents the number of turns in the coil, μ_0 represents the permeability of air and θ the magnetic force/pole angle.

However, equation (3.1) is non-linear. To facilitate modelling, the non-linear model is simplified to a linearised system that functions within a linear interval around a working point. The above setup is linearised by placing two electro-magnets opposite each other (Figure 3.2-3 (b)) and adding a constant pre-magnetisation current, or bias current, i_0, to the control currents, i, and assigning an operating point, x_0.

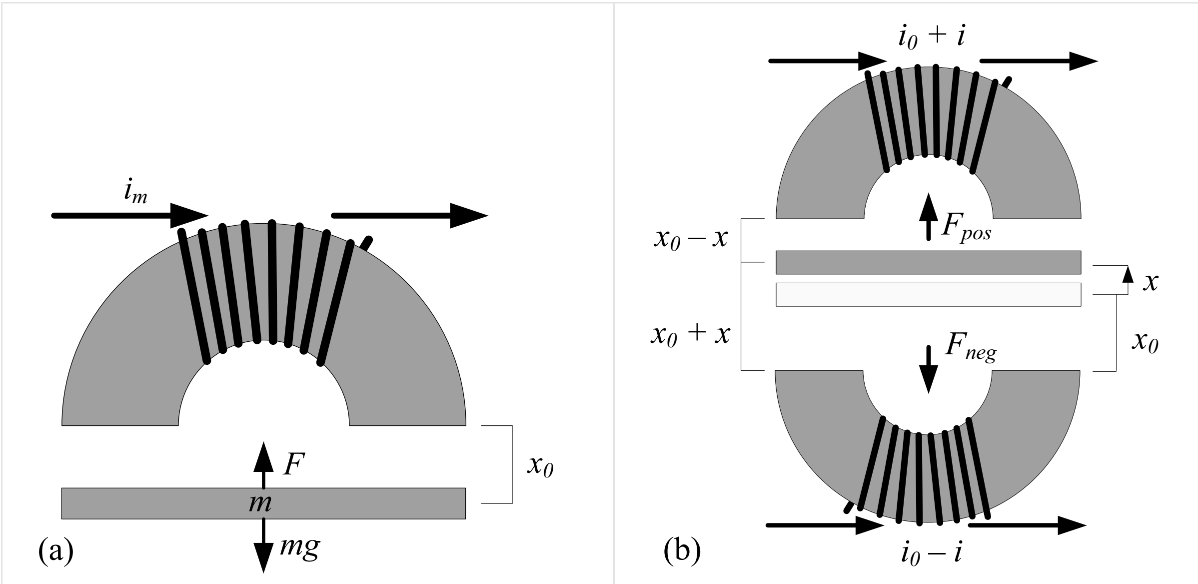

Figure 3.2-3: (a) Simple AMB magnetic setup. (b) Linearised AMB setup.

The current in the first magnet is the bias current plus the control current and the current in the second magnet is the bias current minus the control current. The control current is dependent on the displacement, x, of the object from the operating point, x_0. Therefore the total force acting on the object is the difference between the forces of the two magnets,

$$F = F_{pos} - F_{neg} = K\left(\frac{(i_0+i)^2}{(x_0-x)^2} - \frac{(i_0-i)^2}{(x_0+x)^2}\right). \tag{3.3}$$

By only allowing small deviations from the operating points, i_0 and x_0, equation (3.3) can be linearised around, i_0 and x_0, by [**1**]:

$$F(i,x) = k_i i + k_s x, \tag{3.4}$$

where the current-force constant, k_i, and the displacement-force constant, k_s, are defined as,

$$k_i = \left.\frac{\partial F}{\partial i_m}\right|_{i_m=i_0,\ x_s=x_0} = 2\frac{\mu_0 N^2 i_0 A_g}{x_o^{\ 2}}\cos(\theta)$$

and

$$k_s = \left.\frac{\partial F}{\partial x_s}\right|_{i_m=i_0,\ x_s=x_0} = -2\frac{\mu_0 N^2 i_0^{\ 2} A_g}{x_o^{\ 3}}\cos(\theta).$$

Both derivatives are evaluated with control current i=0 and a rotor position of x=0. The gain, k_i, is positive because the force increases with an increase in current. The gain k_s is negative because the force increases with a decrease in the air gap. As a result, by rearranging and altering (3.4), the force and displacement can be controlled in terms of the control current, i.

3.2.1.2 Rotor and actuators

In order to develop a model for the rigid[20] rotor, a frame of reference (coordinate framework) must first be established. A rigid body can be represented by six coordinates: three displacement coordinates and three rotational coordinates [**1**]. However, because the rotational speed is taken as constant and displacement in the axis of rotation is decoupled from the others; the rotor can be represented by four coordinates only (Figure 3.2-4). Hence, the coordinate framework is:

$$z = [x, \beta, y, -\alpha]^T, \tag{3.5}$$

which represents the displacement (x, y) and inclination (β, α) about the centre of mass [**6**]. Once the coordinate framework is defined, the rotor and bearing dynamics are represented.

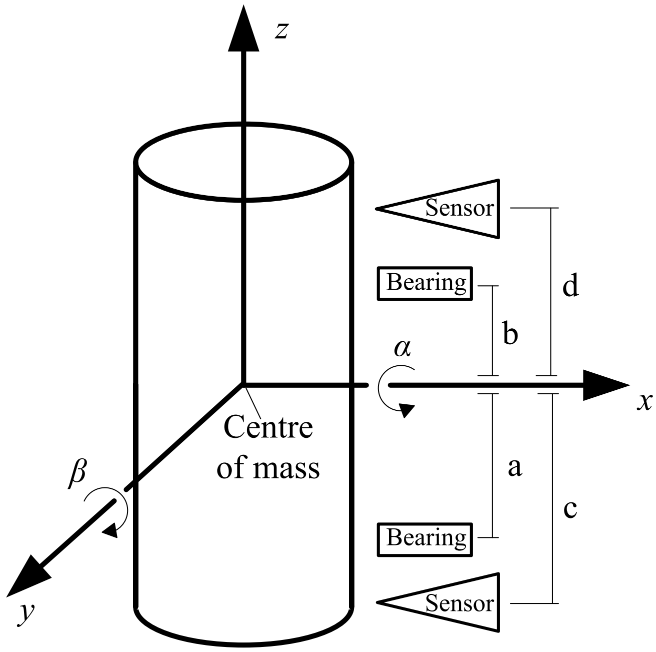

Figure 3.2-4: Rotor, bearing and sensor coordinate frame [**6**].

The rotor dynamics of a simple gyroscopic beam can be represented by the Newton-Euler equations of motion [**6**]:

$$m\ddot{x} = f_x \tag{3.6}$$

$$I_y\ddot{\beta} - I_z\Omega\dot{\alpha} = p_y \tag{3.7}$$

$$m\ddot{y} = f_y \tag{3.8}$$

$$-I_x\ddot{\alpha} - I_z\Omega\dot{\beta} = p_x \tag{3.9}$$

[20] In this dissertation, the Fly-UPS is considered as a rigid rotor body, assembled as a set of connected rigid elements.

The variables f_x and f_y are the forces acting on the centre of mass and p_y and p_x are the force couple moments. Variable m represents the rotor mass and Ω represents the constant angular velocity (rad/s) about the z axis. I_x, I_y and I_z are the moments of inertia in the x, y and z directions respectively. The equations for obtaining the moments of inertia, I_x, I_y and I_z are given and explained in Appendix B.

The Newton-Euler equations above can be simplified by combining them with the selected coordinate framework in equation (3.5) to create the model,

$$\boldsymbol{M}\ddot{\boldsymbol{z}} + \boldsymbol{G}\dot{\boldsymbol{z}} = \boldsymbol{f}, \tag{3.10}$$

where $\boldsymbol{f} = [f_x, p_y, f_y, p_x]$ and **M**, the mass matrix and **G**, the gyroscopic coupling matrix with

$$\boldsymbol{M} = \begin{bmatrix} m & 0 & 0 & 0 \\ 0 & I_y & 0 & 0 \\ 0 & 0 & m & 0 \\ 0 & 0 & 0 & I_x \end{bmatrix} \tag{3.11}$$

and

$$\boldsymbol{G} = \begin{bmatrix} 0 & 0 & 0 & 0 \\ 0 & 0 & 0 & 1 \\ 0 & 0 & 0 & 0 \\ 0 & -1 & 0 & 0 \end{bmatrix} I_z \Omega. \tag{3.12}$$

The actual system is current-controlled, necessitating coil current as input to the model [**4**]. A model with current as input and displacement as output is thus required. However, since the actual position of the rotor is not available but only the measured position at the bearing sensor locations, it would be sensible to transform or reference the above equations of motion to the bearing positions. The transformation from the centre of mass to the equivalent mass at the bearing locations, a and b (compare Figure 3.2-4), is done with the transformation matrix [**6**],

$$\boldsymbol{T}_B = \frac{1}{b-a}\begin{bmatrix} b & -a & 0 & 0 \\ -1 & 1 & 0 & 0 \\ 0 & 0 & b & -a \\ 0 & 0 & -1 & 1 \end{bmatrix}. \tag{3.13}$$

The coordinate framework in (3.5) becomes,

$$\boldsymbol{z} = \boldsymbol{T}_B \boldsymbol{z}_B = \boldsymbol{T}_B \begin{bmatrix} x_a \\ x_b \\ y_a \\ y_b \end{bmatrix}, \tag{3.14}$$

and the mass, gyroscopic and force matrices become:

$$\boldsymbol{M}_B = \boldsymbol{T}_B{}^T \boldsymbol{M}\boldsymbol{T}_B, \;\; \boldsymbol{G}_B = \boldsymbol{T}_B{}^T \boldsymbol{G}\boldsymbol{T}_B, \;\text{ and } \boldsymbol{f}_B = \begin{bmatrix} f_{ax} \\ f_{bx} \\ f_{ay} \\ f_{by} \end{bmatrix}. \tag{3.15}$$

The new equation of motion is thus:

$$\boldsymbol{M}_B \ddot{\boldsymbol{z}}_B + \boldsymbol{G}_B \dot{\boldsymbol{z}}_B = \boldsymbol{f}_B. \tag{3.16}$$

3.2.1.3 Radial state-space equation

According to the linearised system in section 3.2.1.1, the bearing forces are dependent on current and displacement (3.4). These linearised forces are now introduced into the equation of motion (3.16) to form:

$$\boldsymbol{M}_B \ddot{\boldsymbol{z}}_B + \boldsymbol{G}_B \dot{\boldsymbol{z}}_B = \boldsymbol{K}_i \boldsymbol{i}_B + \boldsymbol{K}_s \boldsymbol{z}_B. \tag{3.17}$$

The displacement-force constants, $\boldsymbol{K}_s$ and current-force constants, $\boldsymbol{K}_i$ of the radial bearings are simply diagonal matrices of the previously mentioned, k_s and k_i constants:

$$\boldsymbol{K}_s = \begin{bmatrix} k_{s\_ax} & 0 & 0 & 0 \\ 0 & k_{s\_bx} & 0 & 0 \\ 0 & 0 & k_{s\_ay} & 0 \\ 0 & 0 & 0 & k_{s\_by} \end{bmatrix} \tag{3.18}$$

and

$$\mathbf{K}_i = \begin{bmatrix} k_{i\_ax} & 0 & 0 & 0 \\ 0 & k_{i\_bx} & 0 & 0 \\ 0 & 0 & k_{i\_ay} & 0 \\ 0 & 0 & 0 & k_{i\_by} \end{bmatrix}. \tag{3.19}$$

The current-force and displacement-force values in the x and y directions at 'a' and 'b' are identical, i.e. $k_{s\_ax} = k_{s\_ay}$, and $k_{i\_bx} = k_{i\_by}$ [**4**].

The current vector, $\boldsymbol{i}_B$ is:

$$\boldsymbol{i}_B = \begin{bmatrix} i_{ax} & i_{bx} & i_{ay} & i_{by} \end{bmatrix}^T. \tag{3.20}$$

By rearranging (3.17) and making $\boldsymbol{i}_B = \boldsymbol{u}$, we get:

$$\ddot{\boldsymbol{z}}_B = -\boldsymbol{M}_B^{-1}\boldsymbol{G}_B\dot{\boldsymbol{z}}_B + \boldsymbol{M}_B^{-1}\boldsymbol{K}_s\boldsymbol{z}_B + \boldsymbol{M}_B^{-1}\boldsymbol{K}_i\boldsymbol{u}. \tag{3.21}$$

This gives the standard state-space formulation for the radial AMB system at bearing coordinates as:

$$\begin{aligned} \dot{\boldsymbol{x}}_B &= \boldsymbol{A}_B\boldsymbol{x}_B + \boldsymbol{B}_B\boldsymbol{u} \\ \boldsymbol{y}_B &= \boldsymbol{C}\boldsymbol{x}_B, \end{aligned} \tag{3.22}$$

with

$$\boldsymbol{x}_B = \begin{bmatrix} \boldsymbol{z}_B \\ \dot{\boldsymbol{z}}_B \end{bmatrix},\quad \boldsymbol{A}_B = \begin{bmatrix} 0 & \boldsymbol{I} \\ \boldsymbol{M}_B^{-1}\boldsymbol{K}_s & -\boldsymbol{M}_B^{-1}\boldsymbol{G}_B \end{bmatrix},\quad \boldsymbol{B}_B = \begin{bmatrix} 0 \\ \boldsymbol{M}_B^{-1}\boldsymbol{K}_i \end{bmatrix} \text{ and } \boldsymbol{C} = \begin{bmatrix} \boldsymbol{I} & \boldsymbol{I} \end{bmatrix}. \tag{3.23}$$

Unfortunately, the bearings and sensors of the Fly-UPS are not collocated, requiring two transformations to be made; first to the bearing locations and then to sensor positions. The transformation to bearing coordinates was done in section 3.2.1.2, leaving the transformation to sensor coordinates to be done next.

The bearing coordinate state-space system in (3.22) is referenced to the sensor coordinate system by transforming the state matrices $\boldsymbol{A}_B$ and $\boldsymbol{B}_B$ to

$$\boldsymbol{A}_S = \boldsymbol{T}_S\boldsymbol{A}_B\boldsymbol{T}_S^{-1} \quad \text{and} \quad \boldsymbol{B}_S = \boldsymbol{T}_S\boldsymbol{B}_B, \tag{3.24}$$

with

$$\boldsymbol{T}_S = \begin{bmatrix} \begin{bmatrix} 1 & c & 0 & 0 \\ 1 & d & 0 & 0 \\ 0 & 0 & 1 & c \\ 0 & 0 & 1 & d \end{bmatrix}\boldsymbol{T}_B & \boldsymbol{0} \\ \boldsymbol{0} & \begin{bmatrix} 1 & c & 0 & 0 \\ 1 & d & 0 & 0 \\ 0 & 0 & 1 & c \\ 0 & 0 & 1 & d \end{bmatrix}\boldsymbol{T}_B \end{bmatrix}. \tag{3.25}$$

This gives the final state-space model as:

$$\begin{aligned}\dot{\boldsymbol{x}}_S &= \boldsymbol{A}_S\boldsymbol{x}_S + \boldsymbol{B}_S\boldsymbol{u} \\ \boldsymbol{y}_S &= \boldsymbol{C}\boldsymbol{x}_S\end{aligned} \tag{3.26}$$

with

$$\boldsymbol{x}_S = \begin{bmatrix} x_c & x_d & y_c & y_d & \dot{x}_c & \dot{x}_d & \dot{y}_c & \dot{y}_d \end{bmatrix}^T. \tag{3.27}$$

The rotational speed of the rotor is taken into account in (3.12), and it can be seen from the equation of motion, (3.17), that there is a coupling between the moment in the x plane and the moment in the y plane. As a consequence, this radial AMB model developed is a fully coupled system with four inputs (current) and eight outputs (four displacement variables and their four derivatives). The model for the axial AMB can now be developed and appended to the above radial model as will be explained in the next section.

3.2.1.4 *Axial state-space equation*

In addition to suspending the rotor horizontally, the Fly-UPS system is required to lift and suspend the flywheel vertically. Consequently, the addition of an axial thrust bearing is required. The axial AMB is situated at the top of the Fly-UPS rotor, and will use the thrust disc to exert the required lifting force (Figure 3.2-1). The axial AMB is taken as a simple 1-DOF point mass system (Figure 3.2-3b) because axial rotor movement is assumed decoupled from the rotational speed due to rigid simple body motion [**7**], hence, not influencing the centre of mass of the radial AMBs. There is no need to transform the axial model to bearing or sensor coordinates, as it represents vertical movement of a point mass system only.

The force acting on the axial AMB is calculated similar to (3.3), with the current-force and displacement-force values calculated similarly to (3.4), but with values for the axial AMB:

$$f(i_z, x_z) = k_{iz} i_z + k_{sz} z = m\ddot{z}. \tag{3.28}$$

The state-space model for the axial AMB is thus:

$$\begin{aligned}\dot{\boldsymbol{x}}_z &= \boldsymbol{A}_z\boldsymbol{x}_z + \boldsymbol{B}_z\boldsymbol{u}_z \\ \boldsymbol{y}_z &= \boldsymbol{C}_z\boldsymbol{x}_z,\end{aligned} \tag{3.29}$$

with

$$\boldsymbol{x}_z = \begin{bmatrix} z \\ \dot{z} \end{bmatrix}, \quad \boldsymbol{u}_z = \begin{bmatrix} i_z \end{bmatrix}, \quad \boldsymbol{A}_z = \begin{bmatrix} 0 & 1 \\ \dfrac{k_{sz}}{m} & 0 \end{bmatrix}, \quad \boldsymbol{B}_z = \begin{bmatrix} 0 \\ \dfrac{k_{iz}}{m} \end{bmatrix} \text{ and } \boldsymbol{C}_z = \begin{bmatrix} \boldsymbol{I} & \boldsymbol{I} \end{bmatrix}. \tag{3.30}$$

This gives a system with a single current input and two outputs of displacement and velocity. The model for the axial AMB is simply appended to the model of the radial AMBs, as seen in Figure 3.2-5, because the axial AMB is decoupled from the radial AMBs [**7**].

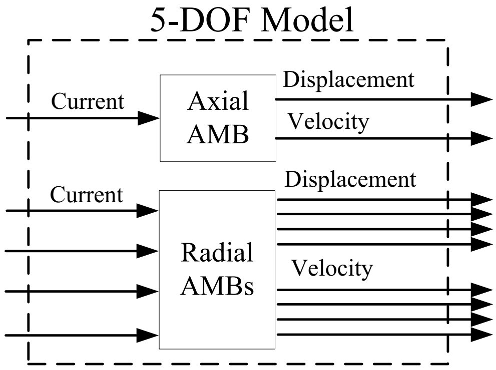

Figure 3.2-5: 5-DOF appended model

3.2.1.5 Application to Fly-UPS

In the previous section, a mathematical model for the NWU's AMB Fly-UPS system was explained. The system dependent coefficients for the Fly-UPS system are now calculated and implemented to form the actual mathematical model as explained above.

All the variables used within this model were obtained from the SolidWorks® simulation platform as well as experimentally measured from the physical Fly-UPS.

Firstly, the moments of inertia as used in (3.11) and (3.12) are determined. Because of the complex design and shape of the AMB rotor, calculating the inertias by hand is extremely difficult and time consuming. Therefore, the values were obtained by using the SolidWorks® software's mass property function. This function calculates the inertias for all axes directly from the 3-D rotor designed in SolidWorks® [**22**].

The moment of inertia values obtained are:

$$\begin{aligned} I_x &= 0.11575\ \mathrm{kg}\cdot\mathrm{m}^2, \\ I_y &= 0.11575\ \mathrm{kg}\cdot\mathrm{m}^2, \\ I_z &= 0.10669\ \mathrm{kg}\cdot\mathrm{m}^2. \end{aligned} \tag{3.31}$$

Secondly, the mass of the rotor and the displacements of the bearings from the centre of mass are [**22**]:

$$m = 17.65 \text{ kg} \tag{3.32}$$
$$a = -160\times10^{-3} \text{ m} \tag{3.33}$$
$$b = 64.4\times10^{-3} \text{ m.} \tag{3.34}$$

The distance of the sensors from the centre of mass are measured to be:

$$c = -190\times10^{-3} \text{ m} \tag{3.35}$$
$$d = 95.4\times10^{-3} \text{ m.} \tag{3.36}$$

Finally, the force-displacement and force-current constants for both the radial AMBs are calculated using (3.4):

$$k_i = \left.\frac{\partial F}{\partial i_m}\right|_{i_m=i_0,\, x_s=x_0} = 30 \text{ N/A} \tag{3.37}$$

$$k_s = \left.\frac{\partial F}{\partial x_s}\right|_{i_m=i_0,\, x_s=x_0} = -150000 \text{ N/m} \tag{3.38}$$

where $\mu_0 = 4\pi\times10^{-7}$, $A_g = 204.026\times10^{-6}$ m^2, $N = 80$, $i_0 = 2.5$ A, $x_0 = 500\times10^{-6}$ m, and $\theta = 22.5°$.

The force-displacement and force-current constants for the axial AMB are given as follows:

$$k_{iz} = 54.9 \text{ N/A} \tag{3.39}$$

$$k_{sz} = -329693 \text{ N/m,} \tag{3.40}$$

with

$\mu_0 = 4\pi\times10^{-7}$, $A_g = 168.45\times10^{-6}$ m^2, $N = 104$, $i_0 = 3$ A, $x_0 = 500\times10^{-6}$ m, and $\theta = 0°$

Hence, a complete 35th order state-space model of the full 5-DOF AMB rotor and actuators is developed. The displacement sensors, power amplifiers and the anti-aliasing filters are to be modelled next.

3.2.2 Sensor model

Although the system above is modelled with current as input and displacement as output, the displacement outputs are not correctly modelled until the characteristics of the displacement sensors are added.

The displacement sensors used within the Fly-UPS system are eddy-current sensors. Eddy-current sensors were chosen due to their resistance to high frequency noise generated by the power amplifiers [**4**]. The eddy-current sensors have a bandwidth of 10 kHz (-3dB) with a stern high frequency cut-off. Thus it would be adequate to model the sensors as second order low-pass filters [**1**]. The two parameters within the sensor model are the bandwidth, ω_s and the damping, ζ. The static sensor gain, $\boldsymbol{K}_{sens}$ is a diagonal matrix in order to represent the 5 displacement sensors in 5 axes.

$$\boldsymbol{T}_{sens} = \boldsymbol{K}_{sens} \cdot \frac{\omega_s^{\,2}}{s^2 + 2\zeta\omega_s s + \omega_s^{\,2}}, \tag{3.41}$$

with

$$\boldsymbol{K}_{sens} = \begin{bmatrix} K_{sensZ} & 0 & \cdots & & 0 \\ 0 & K_{sensX1} & & & \\ \vdots & & K_{sensY1} & & \vdots \\ & & & K_{sensX2} & 0 \\ 0 & & \cdots & 0 & K_{sensY2} \end{bmatrix}. \tag{3.42}$$

For the physical Fly-UPS system, the damping is ζ=0.707, the bandwidth is ω_s =10000·2·π rad/s, and the sensor gains were experimentally measured to be: K_{sensZ} = 1.5 for the z axis, and K_{sensX1} = 1.3, K_{sensY1} = 1.3, K_{sensX2} = 1.5, and K_{sensY2} = 1.5 for the x and y axes of the two radial AMBs respectively. The sensor gains differ between the upper and lower radial AMBs due to the physical proximity of the sensors with respect to the rotor.

The sensor model is converted to a state-space model using a modified version of the controllable canonical form with numerically rescaled state vectors [**14**]. The state-space sensor model (Appendix C) is then connected in series with the displacement outputs of the actuator model.

3.2.3 Power amplifier model

Power amplifiers (PAs) are required within the Fly-UPS system in order to supply control currents to the magnetic actuators [**5**]. The power amplifiers receive reference signals from the controller, and adjust their output levels to closely match the required current value.

The bandwidth of the PA consists of the small signal bandwidth and the power bandwidth. The small signal bandwidth represents the -3dB attenuation frequency of real currents for arbitrary small reference currents [**4**]. The power bandwidth is the frequency where half the rated power is supplied by the PA without distortion. The power amplifiers used within the Fly-UPS system are bi-state, PWM switching amplifiers from Advanced Motion Controls®. Switching amplifiers are used due to their high efficiency and low losses [**4**]. Figure 3.2-6 shows an example of a bi-state, PWM switching amplifier.

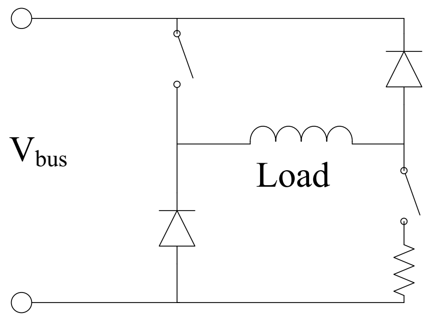

Figure 3.2-6: A bi-state PWM switching amplifier [**31**].

Figure 3.2-7 below shows the block diagram to determine the PA gain and bandwidth, with the PA bus voltage, V_{bus}, and the proportional constant and integral gain, K_P and K_I. The reference current is i_{ref}, the actual current is i_{out}, and R and L are the resistance and inductance of the load.

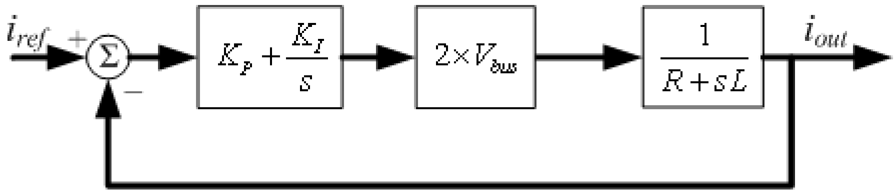

Figure 3.2-7: PA small signal close-loop system.

The closed loop transfer function of the PA is given by:

$$T_{PA} = \frac{i_{out}}{i_{ref}} = \frac{2V_{bus}(K_i + K_p s)}{Ls^2 + (2K_p V_{bus} + R)s + 2K_i V_{bus}}, \tag{3.43}$$

where: V_{bus} = 51 V is the bus voltage, R = 0.152 Ω is the coil resistance, L = 6.494 mH is the coil inductance, K_p = 1 is the proportional constant and K_i = 0.1 is the integral constant.

For the Fly-UPS, the bi-state, PWM switching amplifiers are modelled as a closed loop PI controlled system with a bandwidth of 2.5 kHz and all PAs assumed identical [**4**]. This PA model is then converted to state-space (see Appendix C) and cascaded with each of the current inputs of the rotor and bearing model. The PA model is converted to a state-space model using the same modified version of the controllable canonical form as the position sensors [**14**].

3.2.4 Anti-aliasing filter

The sampling rate of the hardware controller used by the Fly-UPS system is 10 kHz. In order to eliminate aliasing and recover all the signal components, an anti-aliasing filter is introduced at the Nyquist frequency of 5 kHz. The anti-aliasing filter used within the Fly-UPS system is a first order low-pass RC filter with a cut-off frequency of 4.82 kHz [**4**]. Thus the anti-aliasing filter is modelled as a first order low-pass filter and cascaded after the displacement sensors.

Once all the sub-components (anti-aliasing filter, sensors and PAs) are connected to the actuators, a complete model of the AMB Fly-UPS system, as seen in Figure 3.2-2, is created. The complete model is then used for controller development. The accuracy with which the model represents the physical system will be verified in the next section.

3.2.5 Model verification and validation

The mathematical model developed for the Fly-UPS is a linear model, constructed around an operating point as explained in section 3.2.1. In order to verify that this model is valid for the Fly-UPS system, a comparison between the mathematical and physical system response is made. The mathematical system is implemented with standard PD controllers, similar to the PD controllers implemented on the physical system. Figure 3.2-8 shows the setup used for both the mathematical and physical systems.

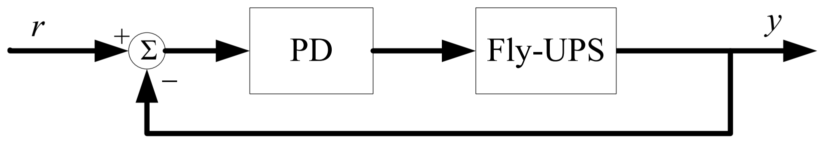

Figure 3.2-8: Closed-loop system setup

The PD values used within the above setup are K_P = 10 000 and K_D = 10 for both radial AMBs in the x and y axes and K_P = 8000 and K_D = 10 for the axial (z-axis) AMB.

Both radial AMBs were consecutively perturbed with a step displacement reference input of 10 µm in the x-axis. The following figures show the x-axis step input comparison between the mathematical and physical systems. The two figures below show the step response of the bottom radial AMB x-axis as well as the effect this step has on the top radial AMB x-axis. This clearly shows the multivariable cross-coupling between the two radial AMBs.

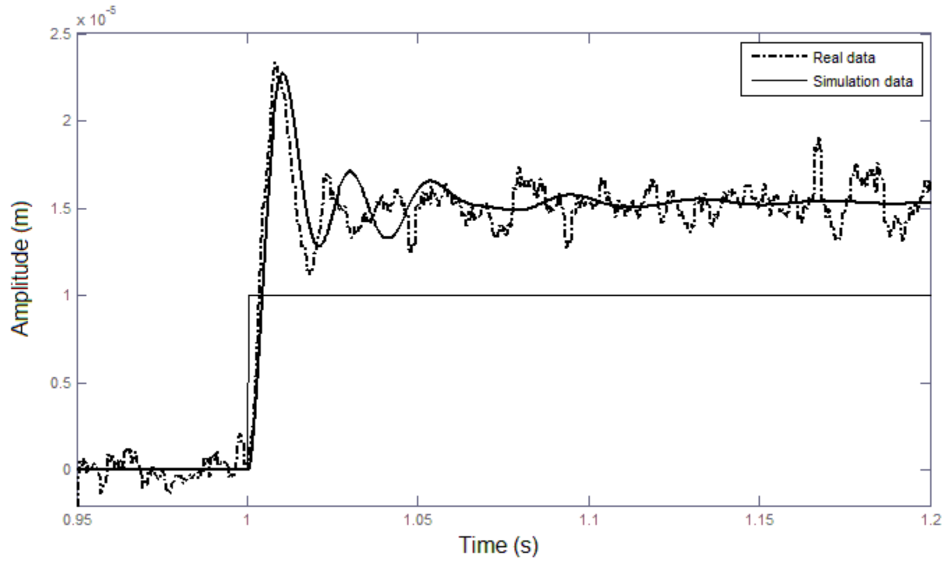

Figure 3.2-9: Bottom AMB x-axis step response (real vs. simulation)

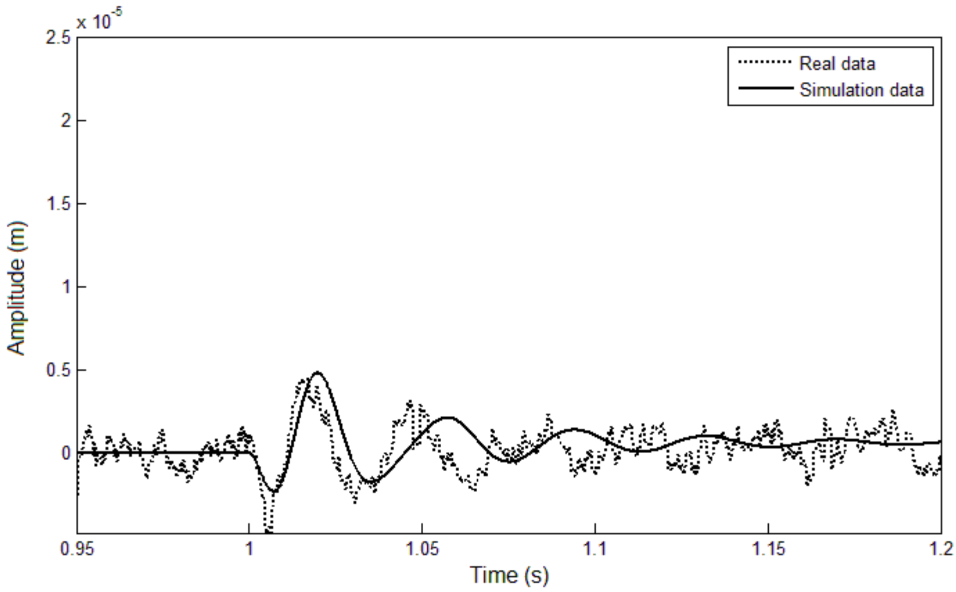

Figure 3.2-10: Bottom to top AMB cross-coupling x-axis response (real vs. simulation)

Similarly, the step response of the top radial AMB *x*-axis as well as the effect this step has on the bottom radial AMB *x*-axis is shown in the following two figures. There is a slight inertial phase shift visible between the real and simulated systems. This is due to less equivalent rotor mass near the top AMB, producing less sluggishness.

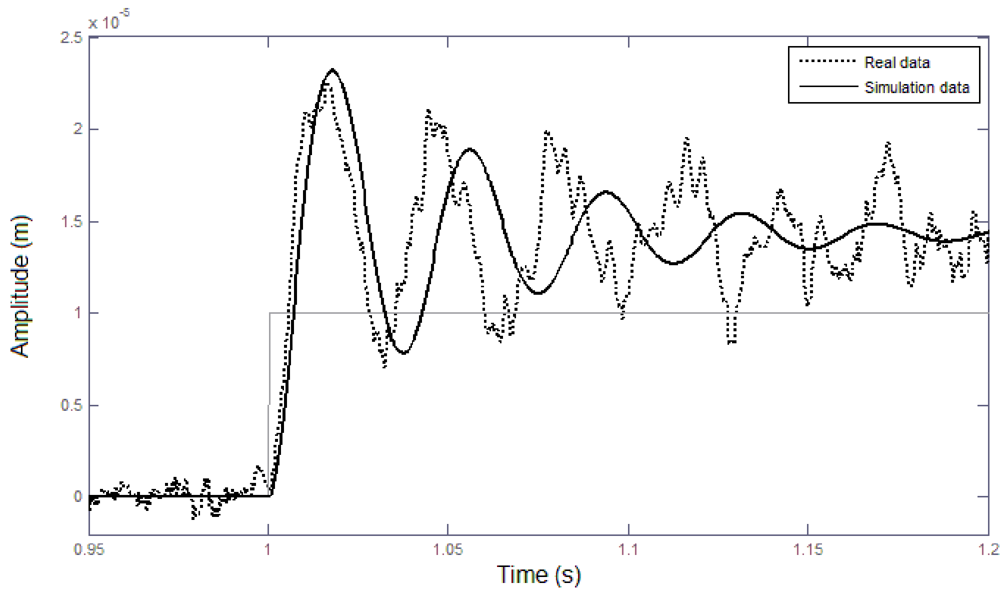

Figure 3.2-11: Top AMB *x*-axis step response (real vs. simulation)

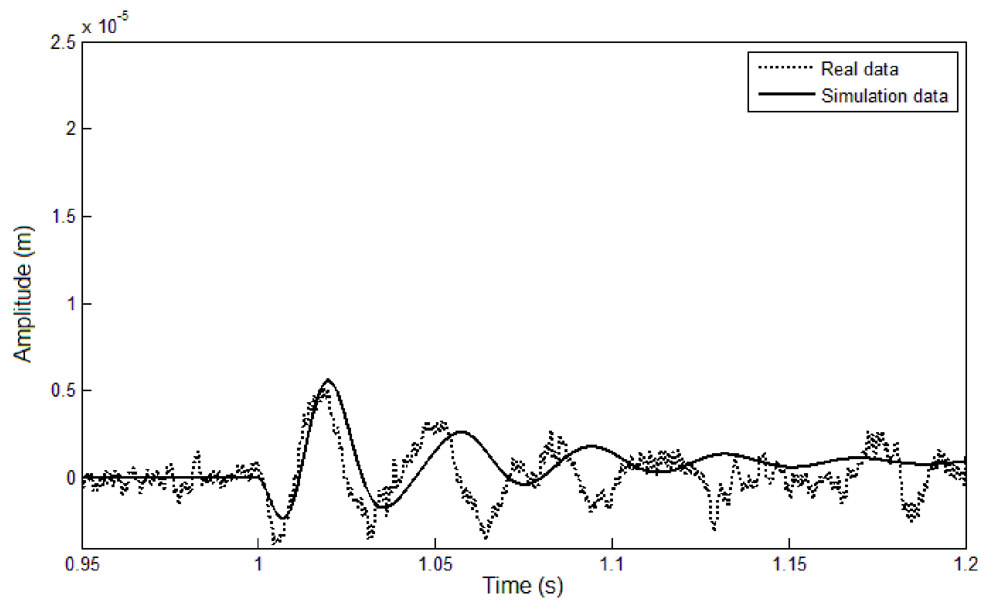

Figure 3.2-12: Top to bottom AMB cross-coupling *x*-axis response (real vs. simulation)

The axial AMB z-axis was perturbed in a similar fashion, using the same 10 µm step reference signal. The oscillation in Figure 3.2-13 may be due to the large deviation from the operating point or lower damping due to the extra pole introduced in the differential path [**16**].

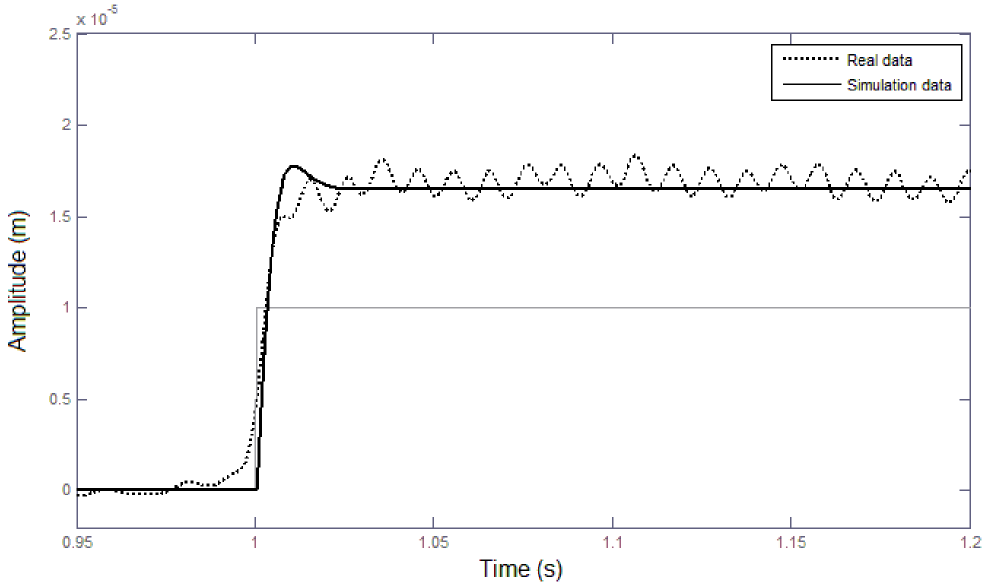

Figure 3.2-13: Axial AMB step response (real vs. simulation)

From the above figures, it is clear that the linear mathematical model developed to represent the Fly-UPS system is accurate and valid within certain bounds around the linear operating point. However, there are minor differences between the mathematical and physical systems, especially concerning stiffness, damping and high frequency noise. This difference between the mathematical and physical system must be characterised in order to synthesise a robust controller from the modelled system.

3.3 Conclusion

This chapter explains the modelling of the AMB Fly-UPS system in detail. Initially, a brief background on different modelling methods was given. Furthermore, a state-space model of both the radial AMBs and the axial AMB was developed and modelled according to the parameters of the physical rotor system. The sensors, power amplifiers and anti-aliasing filters were modelled and cascaded onto the rotor model. Finally, the system response is evaluated whereby the developed multivariable model is verified and validated.

However, with the Fly-UPS being a MIMO[21] plant and inherently unstable, robustness against deviations of the real system from the mathematical model (used to design the controller) is required in order to maintain stability, especially for high speed rotation [**7**]. Moreover, the large clearance between the rotor and the AMB leaves more room for vibration than in traditional ball bearings [**16**].

In the context of robust H_∞ control, it is vital in specifying the uncertainty bound (difference weighting function) between the mathematical model and physical system in order to ascertain stability robustness. This guarantees internal stability of all plants that fall within the bounds of the mathematical model with added uncertainties [**11**]. Hence, robust H_∞ control, including the uncertainty bounds, are characterised and explained in the next chapter.

[21] The Fly-UPS has multiple current inputs and multiple displacement outputs as well as gyroscopic effects, cross-coupled stiffness and speed dependent rotor dynamics.

Chapter 4

Robust H_∞ control theory

This chapter provides an introduction to robust control theory, summarising uncertainties and loop shaping. Furthermore, the mixed sensitivity H_∞ control synthesis strategy using different weighting schemes is investigated. Finally the controller is synthesised with weighting functions relevant to the AMB Fly-UPS system.

4.1 Introduction

Instability is the largest problem in AMBs, especially with the presence of component uncertainties in the amplifiers, air gap uncertainties in the magnetic bearings and displacement uncertainties in the sensors [**11**].

H_∞ control is a multivariable model based control method. If the model the controller is based on contains errors, then the effectiveness of the controller on the real system is questionable. This is part of the problem formulation of robust control theory: synthesising a controller that maintains closed loop stability and performance robustness within predefined tolerances around the modelling errors [**1**]. The robust control framework allows the inclusion of robustness and performance specifications (bounds) in the frequency domain when designing a controller [**9**]. Hence, H_∞ control aims to calculate a controller $\boldsymbol{K}$ such that the adverse effects of modelling errors and disturbances are minimised when implemented [**12**].

The main aspects of robust control theory are system uncertainties and loop shaping, which will be explained in the following sections.

4.2 Uncertainty

All models of any dynamic system contain modelling errors [**1**]. These models only represent a specific part of a physical system, either because it is impossible to model the complete physical system or the effort required in doing so is too large. Generally in standard control design, linear models are considered, although most physical systems are non-linear up to a certain extent. This linearisation introduces modelling errors. Furthermore, when manufacturing designed parts, there is a difference between the parts due to manufacturing tolerances. If these tolerances affect the dynamics of the system, it is impossible for one model to accurately reflect all the different parts. In addition, there are differences between the system and the model because some parameters of the system can only be estimated.

The above observations give rise to the following requirements: a) a controller based on a single flawed model must be able to stabilise the whole family of systems and b) all systems that fall within the predefined error range, controlled by the same controller, must conform to the specified control performance. Robust control theory allows these issues to be managed and implemented.

The model developed in the previous chapter is a linear rigid body motion representation of the Fly-UPS system. Because the physical Fly-UPS system is non-linear, there are system dynamics and gains that are not included in this linear model [**23**]. Furthermore, the Fly-UPS is a rotational system with changing dynamics during variation of rotational speed. As a result, it is necessary to synthesise a controller that maintains stability robustness and performance robustness for a difference between the physical system and the model, as well as the change in rotational speed.

Within robust control design, the linear model is considered as a nominal plant because some system parameters and dynamics are not modelled. It is hard to measure or calculate the AMB parameters and dynamics, such as displacement stiffness, current stiffness or high frequency flexible modes accurately. Mass unbalance is also a large uncertainty within the Flu-UPS system. Therefore it is necessary to identify and bound the differences between the model and the physical system including the changing dynamics with rotational speed variation [**2**]. This is done using an uncertainty bound.

The main types of uncertainty can be characterised within two classes, namely structured uncertainty and unstructured uncertainty.

4.2.1 Parametric (structured) uncertainty

Parametric uncertainty is used to describe well-known uncertainty parameters within the model. This is useful in cases where each individual component (parameter) in a plant deviates from the modelled component over some possible value ranges, either complex or real. It can thus be assumed that each parameter's value is bounded by a region $[\psi_{\min}, \psi_{\max}]$. This gives parameter sets with

$$\psi = \bar{\psi}(1 \pm r_\psi \Delta), \tag{4.1}$$

where $\bar{\psi}$ represents the mean parameter value, $r_\psi = (\psi_{\max} - \psi_{\min})/(\psi_{\max} + \psi_{\min})$ is the relative parameter uncertainty, and Δ is any real scalar with $|\Delta| \le 1$ [**10**].

Structured uncertainties are usually represented in a diagonal matrix with three elements: repeated scalar matrices, repeated scalar complex matrices, and full complex matrices [**13**]. The following definition can thus be applied for structured uncertainty:

$$\begin{aligned}
&\Delta^s \subset \mathbb{C}^{n_w \times n_z} \\
&\Delta^s = \left\{ diag(\delta_1^r I_{r_1}, \ldots, \delta_R^r I_{r_R}, \delta_1^c I_{s_1}, \ldots, \delta_S^c I_{s_S}, \Delta_1 \ldots \Delta_F) \right\} \\
&\delta_i^r \in \mathbb{R} \qquad \delta_i^c \in \mathbb{C} \qquad \Delta_i \in \mathbb{C}^{f_i \times f_i},
\end{aligned} \tag{4.2}$$

where *R* is the number of real matrices, *S* is the number of scalar complex matrices, *F* is the number of full complex matrices and δ is the perturbation [**1**]. The dimensions of the matrices being $r_1, \ldots, r_R$, $s_1, \ldots, s_S$ and $f_1, \ldots, f_F$.

Structured uncertainty is a less conservative approach than unstructured uncertainty [**1**]. However structured uncertainty is often avoided due to the large effort required to model the parameter uncertainty [**10**,**11**]. Furthermore, unstructured uncertainty is the main reason for H_∞ control design because when using clearly parameterised uncertainties, H_∞ control provides no real advantage over conventional state-space control methods [**10**,**12**]. Therefore unstructured uncertainty will be used for classifying model uncertainties.

4.2.2 Dynamic (unstructured) uncertainty

Unstructured uncertainty is the general case where the dynamic modelling errors are characterised. These unmodelled dynamics usually include high frequency uncertainties which are easier to formulate as a lumped unstructured uncertainty block, Δ [**12**]. Unstructured uncertainty is typically represented by a known transfer function matrix where limited information about the uncertainty is known [**24**]. This allows the uncertainty region to be represented in a more "disk-shaped" form, with a single complex perturbation accurately representing the uncertainty [**10**]. The different shapes of uncertainty forms are explained in detail in [**10**].

For the dynamic uncertainty, Δ, only the upper bound b^u on the largest singular value $\bar{\sigma}$ is known, with,

$$\begin{aligned} &\Delta \in \mathbb{C}^{n_w \times n_z} \text{ and} \\ &\bar{\sigma}[\Delta(j\omega)] \leq b^u(j\omega). \end{aligned} \tag{4.3}$$

The above equation states that the uncertainty is norm bounded by a known transfer function for all frequencies, ω, where the upper bound, b^u and the maximum singular value, σ are known. The uncertainty can then be represented by a norm-bounded block $\|\Delta\|_\infty < 1$, cascaded with a scalar transfer function or weight $W_\Delta(s)$ [**24**]. (See appendix A for detail on norms and singular values.)

In addition to the uncertainty type, the way in which the uncertainty perturbs the nominal plant is important. The nominal plant is represented by $G_n(s)$, and the perturbed plant is represented by $G_p(s)$. The two most common representations of modelling uncertainty are additive uncertainty and multiplicative uncertainty [**2**].

Additive uncertainty is represented by (Figure 4.2-1) and given by the following equation:

$$G_p(s) = G_n(s) + W_\Delta(s)\Delta(s). \tag{4.4}$$

The output multiplicative uncertainty is represented by (Figure 4.2-2) and given as:

$$G_p(s) = G_n(s) \times [1 + W_\Delta(s)\Delta(s)]. \tag{4.5}$$

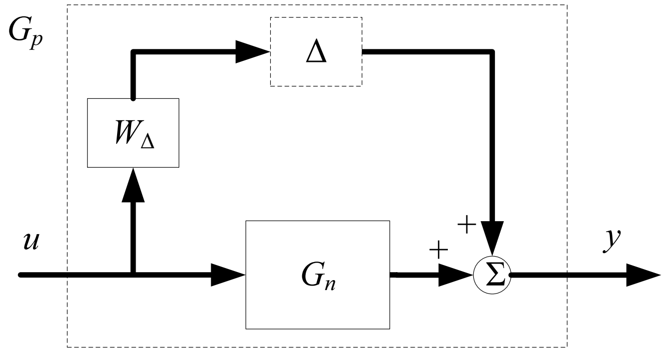

Figure 4.2-1: Additive uncertainty

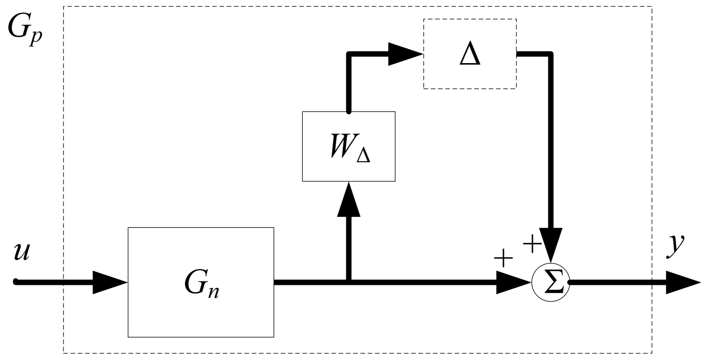

Figure 4.2-2: Output multiplicative uncertainty

Other uncertainty types include: input multiplicative, inverse additive, inverse multiplicative, divisive, and co-prime factor uncertainties. Additional information on these uncertainty types can be found in [**1**], [**2**] and [**24**].

It should be noted again that $W_\Delta(s)$ is a weighting function (bound) that describes the frequency characteristics of the dynamic uncertainty. This uncertainty weight allows the definition of a region around the nominal model within which the non-linear, infinite order physical system resides [**11**]. For the Fly-UPS system the additive method will be used to represent the uncertainty. The additive uncertainty is easier to obtain using present hardware and, furthermore, the control effort and sensitivity are required to be "small" [**11**].

The uncertainty can be isolated from the model, and represented in a standardised form in terms of the uncertainty, Δ, and the augmented interconnected system $\mathbf{G}_a$. This is done using a *linear fractional transformation* (*LFT*). The next section describes the linear fractional transformations.

4.2.3 Linear fractional transformation (LFT)

The additive case in Figure 4.2-1 can be rearranged in order to represent the way in which the uncertainty affects the inputs and outputs of the control system under scrutiny. This rearrangement was introduced in the 1950's and later adapted for robust control uncertainty modelling [**10**,**24**]. This rearrangement is commonly referred to as the general control configuration, shown in Figure 4.2-3, with, **Δ**, the uncertainty, $\boldsymbol{G}_a$, the interconnected system and, ***K***, the controller. Output ***z***, represents all manipulated signals, ***u*** represents the controller output and ***η*** the perturbation output. Input ***w***, represents the reference signals and disturbances, ***v*** represents the uncertainty input, and ***y*** represents the output measurements.

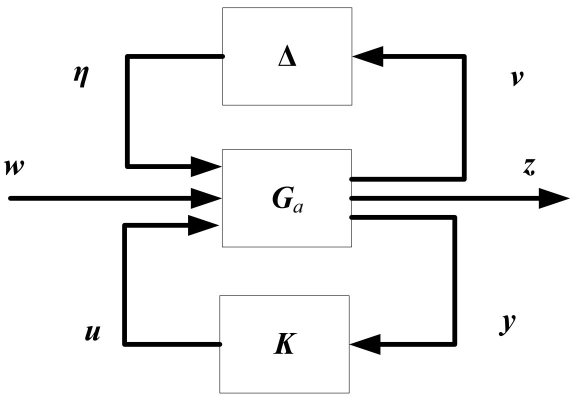

Figure 4.2-3: General control configuration

The system in Figure 4.2-3 corresponds to the following equation:

$$\begin{bmatrix} \boldsymbol{v} \\ \boldsymbol{z} \\ \boldsymbol{y} \end{bmatrix} = \boldsymbol{G}_a \begin{bmatrix} \boldsymbol{\eta} \\ \boldsymbol{w} \\ \boldsymbol{u} \end{bmatrix}, \tag{4.6}$$

with $\boldsymbol{\eta} = \Delta \boldsymbol{v}$ and $\boldsymbol{u} = \boldsymbol{K}\boldsymbol{y}$.

The interconnection system $\boldsymbol{G}_a$ is partitioned as follows:

$$\boldsymbol{G}_a = \begin{bmatrix} \boldsymbol{G}_{a11} & \boldsymbol{G}_{a12} \\ \boldsymbol{G}_{a21} & \boldsymbol{G}_{a22} \end{bmatrix}, \tag{4.7}$$

where $\boldsymbol{G}_{a11}$ and **Δ** as well as $\boldsymbol{G}_{a22}$ and ***K*** have the same dimensions.

When the "upper" loop of $\boldsymbol{G}_a$ is closed with **Δ**, the transfer matrix from ***w*** to ***z*** is derived with

$$\boldsymbol{z} = \left[\boldsymbol{G}_{a22} + \boldsymbol{G}_{a21}\Delta(\boldsymbol{I} - \boldsymbol{G}_{a11}\Delta)^{-1}\boldsymbol{G}_{a12} \right] \boldsymbol{w}. \tag{4.8}$$

If $(\boldsymbol{I}-\boldsymbol{G}_{a11}\Delta)$ is invertible, then

$$\boldsymbol{F}_u(\boldsymbol{G}_a,\Delta)=\boldsymbol{G}_{a22}+\boldsymbol{G}_{a21}\Delta(\boldsymbol{I}-\boldsymbol{G}_{a11}\Delta)^{-1}\boldsymbol{G}_{a12}, \tag{4.9}$$

where the subscript *u* denotes the *upper linear fractional transformation*. Similarly, by incorporating the controller $\boldsymbol{K}$ into the system, the *lower linear fractional transformation* is calculated by

$$\boldsymbol{F}_l(\boldsymbol{G}_a,\boldsymbol{K})=\boldsymbol{G}_{a11}+\boldsymbol{G}_{a12}\boldsymbol{K}(\boldsymbol{I}-\boldsymbol{G}_{a22}\boldsymbol{K})^{-1}\boldsymbol{G}_{a21}. \tag{4.10}$$

When introducing linear fractional transformations, the additive unstructured uncertainty defined in section 4.2.2 can be incorporated using an upper LFT and a correctly organised interconnection system [**24**], with

$$\boldsymbol{G}_a=\begin{bmatrix}0 & \boldsymbol{I}\\ \boldsymbol{I} & \boldsymbol{G}_n\end{bmatrix}. \tag{4.11}$$

Once the uncertainty structure has been incorporated, it is important for a control system to maintain stability when such model uncertainty is present. One method of testing the stability when perturbed with worst-case uncertainty is the small gain theorem. This will be explained in the following section.

4.2.4 Small gain theorem

A system is robust if it maintains stability and certain performance objectives when perturbed by modelling uncertainties [**24**]. The small gain theorem is the robust stability criterion for a plant under unstructured perturbations, as is the case with the Fly-UPS [**11**]. However, the small gain theorem is potentially conservative[22] when applied to general functions. Nevertheless, a small gain theorem version suitable for H_∞ control design will be given.

Consider the system defined in Figure 4.2-4, where the perturbed nominal plant $\boldsymbol{G}_n$, is stabilised by a controller $\boldsymbol{K}$, where the additive perturbation is $\Delta(s)$, an unknown "full" system, but stable. According to the small gain theorem, the closed loop system will remain stable, with stable unstructured uncertainty, as long as the closed loop gain remains below one. It is clear from Figure 4.2-4, that the transfer function from $\boldsymbol{\eta}$ to $\boldsymbol{u}$ is $\boldsymbol{T}_{u\eta}=-\boldsymbol{K}(\boldsymbol{I}+\boldsymbol{G}_n\boldsymbol{K})^{-1}$.

[22] Conservative, in this case, refers to the uncertainty bound enclosing excessive uncertainties not present in the system.

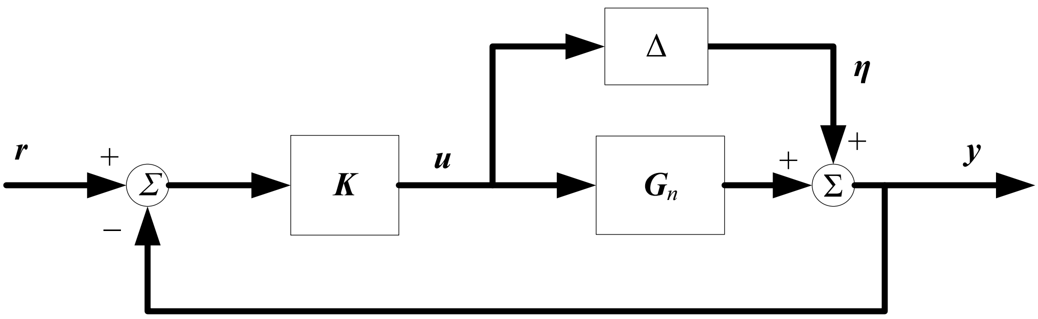

Figure 4.2-4: Additive system configuration

Thus, from the small gain theorem, the following theorem holds:

Definition [**24**]**:** *For stable* $\Delta(s)$, *the closed-loop system is robustly stable if* $\boldsymbol{K}(s)$ *stabilises the nominal plant and the following holds*

$$\left\| \Delta \boldsymbol{K}(\boldsymbol{I}+\boldsymbol{G}_n\boldsymbol{K})^{-1} \right\|_\infty < 1 \tag{4.12}$$

and

$$\left\| \boldsymbol{K}(\boldsymbol{I}+\boldsymbol{G}_n\boldsymbol{K})^{-1} \Delta \right\|_\infty < 1 \tag{4.13}$$

or, in strengthened form,

$$\left\| \boldsymbol{K}(\boldsymbol{I}+\boldsymbol{G}_n\boldsymbol{K})^{-1} \right\|_\infty < \frac{1}{\left\| \Delta \right\|_\infty}. \tag{4.14}$$

The second condition becomes necessary when the unknown Δ *may have all phases.*

The largest possible combination of perturbations can be robustly stabilised using a controller that adheres to the following H_∞ norm[23] minimisation problem [**24**],

$$\min_{\boldsymbol{K}} \left\| \boldsymbol{K}(\boldsymbol{I}+\boldsymbol{G}_n\boldsymbol{K})^{-1} \right\|_\infty. \tag{4.15}$$

In most cases it is possible to characterise the approximate shape or bound of the perturbation. The bound of the uncertainty can be determined either with *a priori* knowledge of the system uncertainty or with system identification techniques such as model error modelling [**1**]. Therefore, assume the uncertainty is bounded in the frequency domain with,

$$\bar{\sigma}(\Delta(j\omega)) \le \bar{\sigma}(\boldsymbol{W}_\Delta(j\omega)) \quad \text{for all} \quad \omega \in \mathbb{R}. \tag{4.16}$$

[23] See appendix A for details on system norms.

This allows the perturbation block to be rewritten as

$$\Delta(s) = \Delta \boldsymbol{W}_{\Delta}(s), \tag{4.17}$$

where $\|\Delta\|_{\infty} \leq 1$ is the unit norm uncertainty set. Accordingly, the robust stabilisation condition in (4.12) becomes

$$\left\| \boldsymbol{W}_{\Delta} \boldsymbol{K} (\boldsymbol{I} + \boldsymbol{G}_n \boldsymbol{K})^{-1} \right\|_{\infty} < 1, \tag{4.18}$$

and the minimisation problem in (4.15) becomes

$$\min_{\boldsymbol{K}} \left\| \boldsymbol{W}_{\Delta} \boldsymbol{K} (\boldsymbol{I} + \boldsymbol{G}_n \boldsymbol{K})^{-1} \right\|_{\infty}. \tag{4.19}$$

The above procedure thus provides a robust stabilisation condition for additive system uncertainty, applicable to the Fly-UPS system.

4.2.5 Performance conditions

It is important, however, to realise that *robust stabilisation* as well as *performance* condition specifications are important in H_{∞} control design. The reason for this is that in H_{∞} design, the robust stabilisation (minimisation) specifications are first provided as *performance condition* problems and then solved in order to find a controller. Hence, before actually characterising the uncertainty bound for the Fly-UPS system, the performance conditions must be explained.

Consider the feedback control system depicted in Figure 4.2-5 with the plant G_n and the controller K. The reference input, control signal, error signal, disturbance input and system output are r, u, e, d and y respectively. The plant model can be written as

$$\begin{aligned} y &= (I + G_n K)^{-1} G_n K r + (I + G_n K)^{-1} d \\ u &= K (I + G_n K)^{-1} r - K (I + G_n K)^{-1} d \\ e &= (I + G_n K)^{-1} r - (I + G_n K)^{-1} d. \end{aligned} \tag{4.20}$$

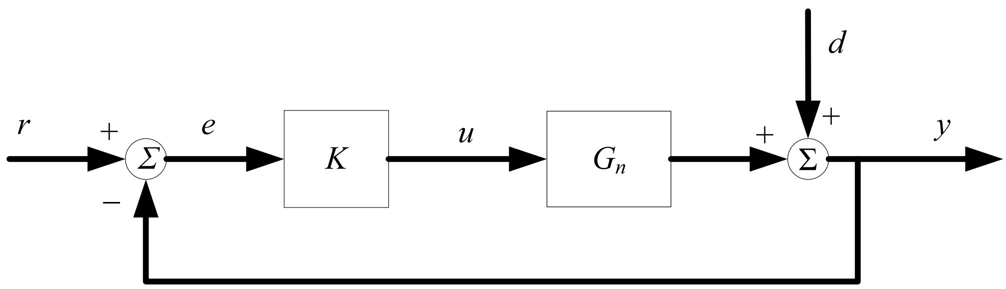

Figure 4.2-5: Standard feedback control system

When using the following terminology:

$S = (I + G_n K)^{-1}$: Sensitivity function and

$T = (I + G_n K)^{-1} G_n K$: Complimentary sensitivity function,

equation (4.20) becomes

$$\begin{aligned} y &= Tr + Sd \\ u &= KSr - KSd \\ e &= Sr - Sd. \end{aligned} \tag{4.21}$$

Assume that the signals r and d are energy bounded and normalised, although the exact signal shapes are unknown. The standard performance specifications require that the tracking, r, and disturbance rejection, d, should be as good as possible. Thus, in correlation with the previous section, the H_∞ norm for these corresponding signals' transfer functions should be minimised.

The design problem is then to find a controller K within the controller set that minimises:

- for good tracking response and disturbance attenuation,

$$\left\| W_e S \right\|_\infty , \tag{4.22}$$

- for less control energy,

$$\left\| W_u KS \right\|_\infty , \tag{4.23}$$

- for good closed loop response,

$$\left\| W_y T \right\|_\infty . \tag{4.24}$$

The identity $S + T = I$ describes the terms sensitivity and complimentary sensitivity [**10**]. Unfortunately, this identity forces a trade-off between minimising either S or T or achieving a balance between the two.

In general, instead of minimising the sensitivity or complimentary sensitivity alone, weighting functions are used in the minimisation procedure. For example, in

$$\min_K \left\| W_e S \right\|_\infty , \tag{4.25}$$

the weight W_e is used to shape the sensitivity function according to the requirement for a good tracking response. These weighting functions are usually required to be stable and of minimum phase [**2**].

Finally, when comparing the minimisation problem as given in (4.19) with the control energy minimisation given in (4.23), it is clear that the weight used to shape the control energy, W_u *is the same as the weight used to represent the additive uncertainty,* W_Δ*. Hence the robustness requirements are represented as performance condition problems.*

Following the definition of the uncertainty specification, robust stability and performance conditions explained above, it would be appropriate to characterise the actual additive uncertainty bound for the Fly-UPS system.

4.2.6 Uncertainty bound for the Fly-UPS

Typically, uncertainty weighting functions are defined based on a priori knowledge of the system perturbations or trial and error specifications. However, this can result in overly conservative uncertainty bounds. It therefore makes sense to specify the uncertainty using a more direct approach in order to reduce error conservativeness.

As previously explained, the uncertainty for the Fly-UPS is unstructured and additive. The standard black box modelling approach, as explained in Chapter 3, can be modified in order to estimate the additive model uncertainty. Instead of using the standard method of mapping the system inputs to the system outputs, the mapping is calculated from system inputs to modelling error. This method is called model error modelling (MEM) and is illustrated in Figure 4.2-6 [**21**].

The model error modelling approach conveys the following:

- The difference between the output of the physical plant and the nominal model is to be predicted, with $e(t) = y(t) - \hat{y}(t)$.
- The model error model is identified and represents the unmodelled dynamics of the system with input $u(t)$ and output $\hat{e}(t)$, giving the additive error between the physical system and the linear model with transfer function $\hat{e}(t) / u(t)$.

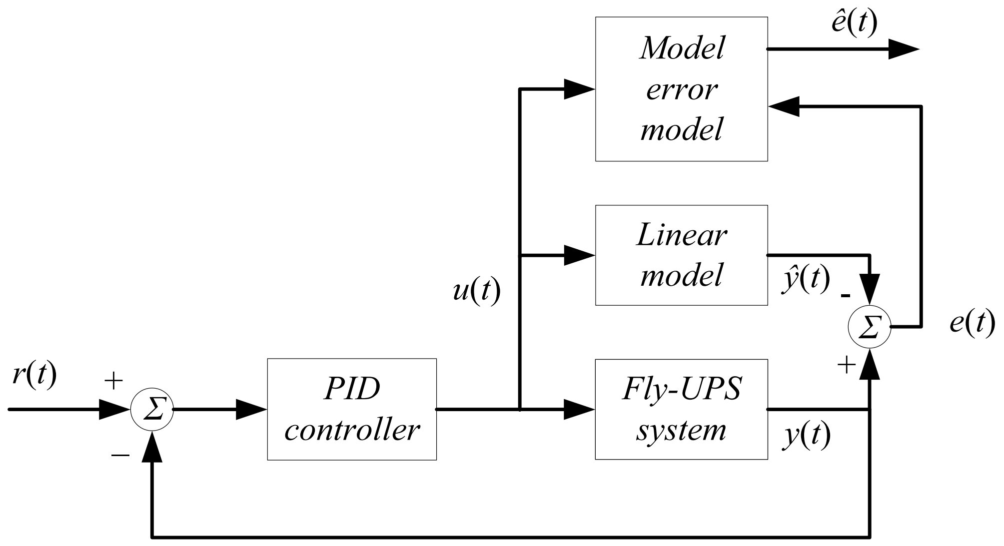

Figure 4.2-6: Model error modeling process

Usually the dynamic model error model explained above is identified using standard parametric system identification techniques such as recursive least squares (RLS) [**9**,**11**]. However for the Fly-UPS system, the model error model was identified using MATLAB®'s *drawmag* command. This involves plotting the model error frequency response data values and then specifying amplitudes at specific frequency points and fitting a transfer function through the specified points (explained in [**14**]). This allows fitting low order transfer functions; however, these low order transfer functions may not be optimised to include extreme outliers (visible in Figure 4.2-9).

For the Fly-UPS system, the aim is to calculate the uncertainty bound for each output of the system. Thus linear mappings for the five-degrees-of-freedom (5-DOF) of the Fly-UPS system from the five inputs to the five error outputs are determined. This is done by first stabilising the Fly-UPS system using the PD controller implemented in section 3.2.5. Then calculating the frequency response functions (FRF) of the model as well as the physical system. The difference between these FRFs is taken as the uncertainty [**9**,**23**].

Denote the frequency response of the *nominal model* at standstill as $H_n(j\omega)$ and the frequency response of the *real system* at standstill as $H(j\omega)$. The additive model error frequency response function (FRF) can be determined experimentally [**9**,**11**], and is defined as:

$$\left|H_\Delta(j\omega)\right| \geq \left|H(j\omega) - H_n(j\omega)\right|. \tag{4.26}$$

The upper magnitude bound (maximum) of the model error FRF, $H_{\Delta}(j\omega)$ is fitted using MATLAB®'s *drawmag* function. This fitted magnitude bound is taken as the uncertainty bound. The procedure explained above is repeated for all five-degrees-of-freedom, i.e. the lower radial AMB *x*- and *y*-axes, the upper radial AMB *x*- and *y*-axes and finally the axial AMB *z*-axis.

The Fly-UPS system dynamics are rotational speed, **Ω**, dependent, as explained and modelled in Chapter 3. Therefore, the uncertainty is also rotational speed dependent, and thus an uncertainty set exists for each rotational speed [**3**]. In order to truly represent the uncertainty, a linear parameter varying (LPV) uncertainty model is required [**23**]. However, since the developed mathematical model of the Fly-UPS is a linear, time invariant (LTI) model, the linear uncertainty is mapped for a difference in the plant and model at certain fixed rotational speeds only [**23**]. The rotational speeds are chosen rather arbitrarily, depending on the system capability and the difference in system response over the rotational speed range [**11**].

The Fly-UPS system is designed to function at a rotational speed ranging from 0 r/min to 25 000 r/min. However due to physical limitations and actuator saturation, the Fly-UPS system could only be excited to 5000 r/min using the PD controller implemented in section 3.2.5. Furthermore, on speculation of weakly damped dominant poles at higher rotational frequencies, large, low frequency, oscillatory behaviour is transposed onto the rotor forcing it into a continuous cyclic oscillation[24]. Present studies on the Fly-UPS system at the NWU have found that the cyclic oscillatory behaviour can be replicated in simulation by including the 11th bending mode in the rotor model. This phenomenon is still being researched.

Following the above limitation, the four speeds selected for a balanced dynamic representation of the uncertainties are: standstill, 1000 r/min, 2000 r/min, and 5000 r/min. Therefore, in order to ensure robustness, the additive uncertainty bound (W_{Δ}) between the model and the physical system across the rotational speeds defined above, must be obtained [**13**].

The procedure surrounding (4.26) above is repeated for rotational speeds of 1000 r/min, 2000 r/min, and 5000 r/min in all five-degrees-of-freedom. Once the uncertainty boundaries for all

[24] One way in eliminating the weakly damped poles is to utilise pole placement. However, in the H_{∞} control framework, pole placement (or pole-zero cancellation) produces transition zeros at the stable plant poles, slow transients, as well as a controller that contains the inverse of the model itself ([**26**] and [**1**]).

four rotational speeds are calculated, the single maximum magnitude fitted across these four uncertainty boundaries (from 0 r/min to 5000 r/min) for each degree-of-freedom is taken as the complete uncertainty bound, W_Δ. Hence there will be five complete uncertainty bounds for the 5-DOF. Unfortunately, by taking uncertainty over such a broad range (0-5000 r/min), the conservativeness of the uncertainty bound is enlarged [**11**]. Thus it is necessary to select the uncertainty bounds as accurate as possible in order to improve performance, while still achieving robust stability.

The calculated uncertainty bounds are applied to the Fly-UPS modelled at 0 r/min, from which a controller is synthesised. It is thus clear that W_Δ describes the frequency characteristics of the uncertainty and defines the model variation upwards from standstill to 5000 r/min [**12**].

It should be noted that the difference in uncertainty between the lower radial AMB *x*-axis and *y*-axis is so small, that the same uncertainty bound is used for both the *x*-axis and *y*-axis. The same holds for the upper radial AMB *x*-axis and *y*-axis. Hence, only three uncertainty bounds for the lower radial AMB, upper radial AMB, and axial AMB across the rotational speed range are used (Figure 4.2-7, Figure 4.2-8 and Figure 4.2-9 below).

The uncertainty bound transfer functions are:

$$W_{\Delta lower} = \frac{3.44\times10^{-5}s^3 + 0.18s^2 + 305.4s + 4.45\times10^4}{s^3 + 2021s^2 + 1.89\times10^6 s + 1.14\times10^9}, \tag{4.27}$$

$$W_{\Delta upper} = \frac{2.37\times10^{-5}s^4 + 0.047s^3 + 28.14s^2 + 1.46\times10^4 s + 9.15\times10^5}{s^4 + 745.6s^3 + 9.17\times10^5 s^2 + 1.08\times10^8 s + 5.04\times10^{10}}, \tag{4.28}$$

$$W_{\Delta axial} = \frac{4.29\times10^{-5}s^3 + 0.088s^2 + 34.39s + 6075}{s^3 + 217.7s^2 + 2.64\times10^5 s + 2.67\times10^7}, \tag{4.29}$$

for the lower radial AMB, upper radial AMB, and axial AMB respectively. These transfer functions are then placed in a diagonal matrix, $\boldsymbol{W}_\Delta$, corresponding to the number of inputs of the plant.

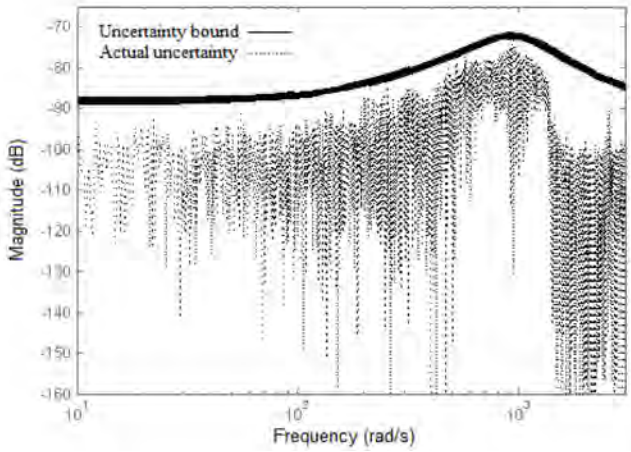

Figure 4.2-7: Lower radial AMB uncertainty bound

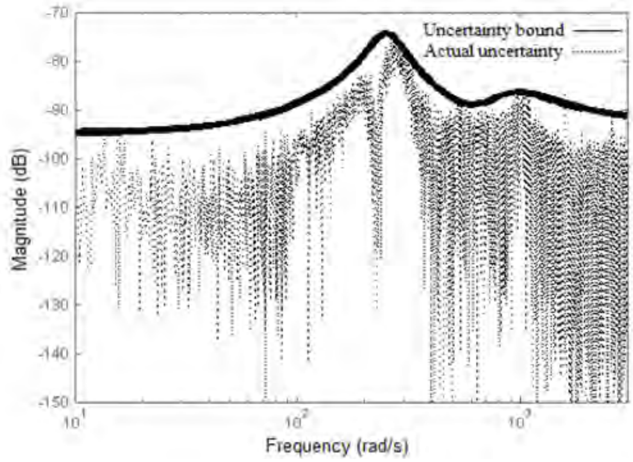

Figure 4.2-8: Upper radial AMB uncertainty bound

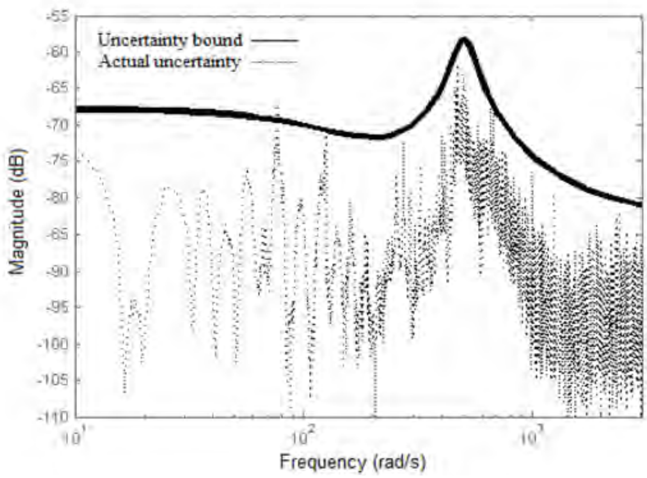

Figure 4.2-9: Axial AMB uncertainty bound

The uncertainty bounds are only displayed up to 500 Hz. The reason for this is because the Fly-UPS system is rated at 25 000 r/min (417 Hz), thus for clarity, the uncertainty bounds are only displayed for frequencies up to 500 Hz.

By formulating and including the uncertainty weight in the H_∞ control design framework, the robustness objectives are formulated as performance objectives, bypassing the nonconvex formulation of the robust control problem [**12**]. Hence H_∞ control exhibits relative robustness both in stability and performance [**5**].

4.3 Robust control

The main goal of H_∞ control synthesis is to "press down" the peaks of transfer functions selected by the designer. The robust H_∞ control synthesis procedure basically has two design approaches [**10**]: loop shaping design and signal based design.

In loop shaping, the required shape of the system transfer function is defined in the frequency domain using singular values, and a controller is designed to shape the system transfer function into that required shape. Loop shaping enables the design of a controller when lacking exact knowledge of the modelling uncertainty. This shifts the design focus to the classical design of imposing sensible transfer function loop shapes to a system [**2**].

On the other hand, signal based design aims to minimise the size of system signals and is a very general approach. The focus shifts from shaping the size and bandwidth of transfer functions, to shaping the sizes of signals alone. LQG[25] control and μ-synthesis are good examples of signal based design methods [**11**]. However signal based design requires the uncertainties to be characterised in a structured parametric form [**2**]. For the Fly-UPS system the uncertainties represent the dynamic error transfer functions, are unstructured, and are used to shape the frequency domain system transfer functions. When accurate modelling of the uncertainty is not available, the loop shaping design method is ideal and will therefore be used.

Within loop shaping, there are two options. One is based on the open-loop transfer function loop shaping and the other one on closed-loop transfer function loop shaping. For open-loop

[25] Linear Quadratic Gaussian control was developed for the Fly-UPS system in [**18**].

shaping, the classical $L=GK$ loop shaping is transposed to MIMO systems by using the singular values of the loop transfer functions as the loop gains [**12**]. One such open-loop transfer function loop shaping method is the Glover-McFarlane[26] H_∞ loop shaping method [**2**,**12**].

Alternatively, closed-loop transfer function shaping aims to shape the sensitivity function $S=(I+GK)^{-1}$ *and the closed-loop transfer function* $T=GK(I+GK)^{-1}$ [**10**]. *This leads to classic mixed sensitivity* H_∞ *control synthesis.*

By adhering to open-loop design objectives, it is relatively easy to estimate the closed-loop requirements over specific frequencies [**10**]. However, because AMB systems are open-loop unstable, specifying an open-loop shape is somewhat difficult. Consequently, closed-loop transfer function design using H_∞ *mixed sensitivity control synthesis* will be the primary focus of this dissertation [**2**]. This allows robust stability by including uncertainty bounds in the model as well as providing robust performance by minimizing the H_∞ norm via weighting [**14**].

Optimal performance can be achieved if the uncertainty weightings are ignored in the controller formulation [**25**]. The controller will still try to achieve the performance objective if the uncertainty weight is included, creating a trade-off between performance and robustness. This is called the waterbed effect [**12**]. H_∞ control does not carry with it any robustness guarantees with respect to modelling uncertainties, however it can be overcome by adding the uncertainty as a performance objective in order to guarantee robust stability [**25**].

4.3.1 Mixed sensitivity H_∞ control design

As explained in section 4.2.5, the stability and performance requirements can be formulated as a minimisation problem. However it would not be sensible to only minimise a single cost function, but rather a combination of cost functions. For example, the standard three block mixed sensitivity control scheme uses three weights or bounds in the mixed sensitivity cost minimisation problem (Figure 4.3-1),

[26] Glover and McFarlane developed H_∞ loop shaping using normalized co-prime factorization which is explained in [**12**].

$$\min_{K}\left\|\begin{matrix} W_e S_o \\ W_u K S_o \\ W_y T_o \end{matrix}\right\|_{\infty} \tag{4.30}$$

where K is a stabilising controller [**26**]. The weights are applied to the control error, e, to shape the output sensitivity, S_o; to the control signal, u, to shape the input sensitivity, KS_o; and to the plant output, y, to shape the complimentary sensitivity, T_o. *Remember, the weight* $W_u = W_\Delta$ *as previously explained in section 4.2.5*. The weighting functions are used to shape, or penalise, the above signals into their desired shapes. However, the weighting functions must be proper and stable to be solvable, since they are not in the loop to be stabilised by the controller [**1**].

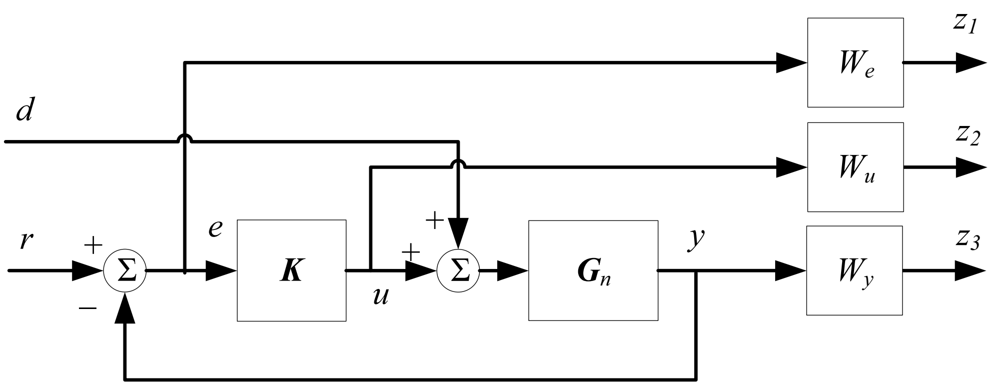

Figure 4.3-1: Standard mixed sensitivity control scheme

In order to adopt a standard configuration, the standard mixed sensitivity scheme above is recast by rearranging Figure 4.3-1 into the augmented configuration given in Figure 4.3-2.

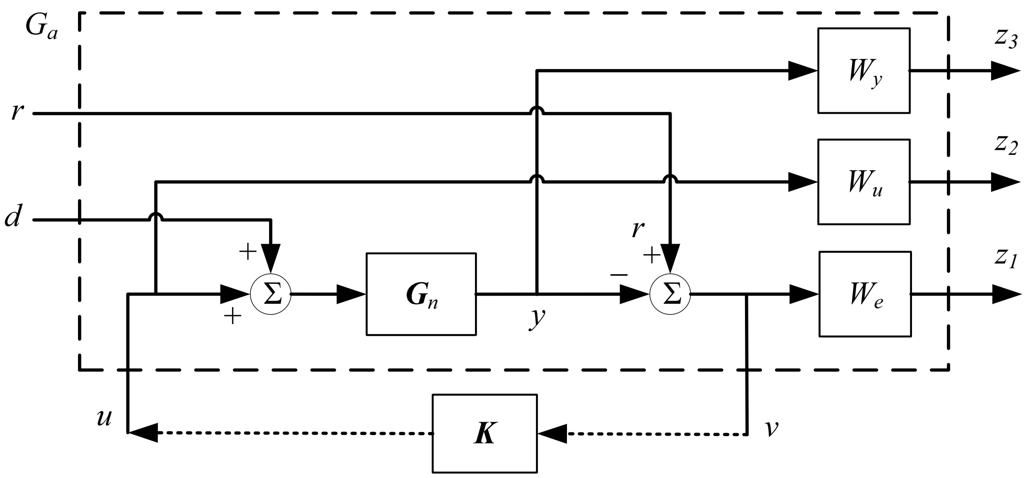

Figure 4.3-2: Augmented mixed sensitivity control scheme

This can then be simplified as shown in Figure 4.3-3, which is similar to the LFT explained in section 4.2.3. The augmented plant or interconnected system, $\boldsymbol{G_a}$, contains the nominal model, $\boldsymbol{G_n}$, and the appropriately connected weighting functions. The signals are then grouped into external inputs and outputs, as well as controller inputs and outputs. The signal $\boldsymbol{y}$ is the vector of measurements available to the controller, $\boldsymbol{K}$, and $\boldsymbol{u}$ the control signals. The weighted signals $\boldsymbol{w}$ and $\boldsymbol{z}$ denote the performance and robustness objectives to be minimised. The objective is thus to find a controller $\boldsymbol{K}$ that minimises the H_∞-norm of the transfer function, $\boldsymbol{T}_{zw}$, from $\boldsymbol{w}$ to $\boldsymbol{z}$.

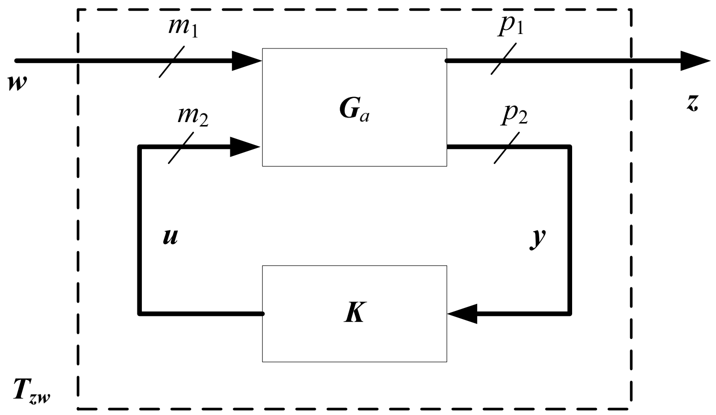

Figure 4.3-3: Standard H_∞ control scheme

The state-space description of $\boldsymbol{G_a}$ is:

$$\begin{bmatrix} \boldsymbol{z} \\ \boldsymbol{y} \end{bmatrix} = \begin{bmatrix} \boldsymbol{A} & \boldsymbol{B}_1 & \boldsymbol{B}_2 \\ \boldsymbol{C}_1 & \boldsymbol{D}_{11} & \boldsymbol{D}_{12} \\ \boldsymbol{C}_2 & \boldsymbol{D}_{21} & \boldsymbol{D}_{22} \end{bmatrix} \begin{bmatrix} \boldsymbol{w} \\ \boldsymbol{u} \end{bmatrix}, \tag{4.31}$$

with dimensions m_1, m_2, p_1, and p_2 as indicated in Figure 4.3-3.

The H_∞ control design for $\boldsymbol{T}_{zw}$ is now [**1**][**10**]:

a) Find a controller $\boldsymbol{K}$ that stabilizes the system $\boldsymbol{T}_{zw} = \boldsymbol{F}_l(\boldsymbol{G}_a, \boldsymbol{K})$.

b) The controller must be such that the H_∞-norm[27] is minimized with $\|\boldsymbol{T}_{zw}\|_\infty < \gamma$ [28]

[27] The H_∞ norm is the supremum of the largest singular value over all frequencies (see appendix A) [**10**].

[28] γ is the condition number, which is the ratio between the maximum and minimum singular values: $\gamma(G) \triangleq \bar{\sigma}(G)/\underline{\sigma}(G)$. [**12**]

The minimisation condition, $\|\boldsymbol{T}_{zw}\|_\infty < \gamma$ given above, is called the *suboptimal problem* and states that the H_∞-norm of the closed-loop transfer function must be less than the condition number, γ [**12**]. The value of γ can be reduced successively in order to obtain an optimal solution, however, as γ approaches its minimum γ^* (Appendix A), the problem becomes numerically ill-conditioned [**24**]. If the two conditions above, *a)* and *b)*, are met, the transfer functions in $\boldsymbol{T}_{zw}$ have their desired shapes. However, there are certain conditions that have to be met for the existence of a suboptimal H_∞ solution. These conditions are explained in [**12**] and [**24**], and are summarised below:

- The set $(\boldsymbol{A}, \boldsymbol{B}_2)$ is stabilisable and the set $(\boldsymbol{A}, \boldsymbol{C}_2)$ is detectable[29].
- $\boldsymbol{D}_{12} = \begin{bmatrix} 0 \\ \boldsymbol{I}_{m_2} \end{bmatrix}$ and $\boldsymbol{D}_{21} = \begin{bmatrix} 0 & \boldsymbol{I}_{p_2} \end{bmatrix}$.
- $\begin{bmatrix} \boldsymbol{A} - j\omega\boldsymbol{I} & \boldsymbol{B}_2 \\ \boldsymbol{C}_1 & \boldsymbol{D}_{12} \end{bmatrix}$ has full column rank for all ω.
- $\begin{bmatrix} \boldsymbol{A} - j\omega\boldsymbol{I} & \boldsymbol{B}_1 \\ \boldsymbol{C}_2 & \boldsymbol{D}_{21} \end{bmatrix}$ has full row rank for all ω.
- $\bar{\sigma}(\boldsymbol{D}_{11}) < \gamma$.
- $\boldsymbol{D}_{22} = 0$.

There are several solutions for the above H_∞ problem, one of which is the state-space method based on the solution of two Riccati equations (compare [**10**,**12**] and [**24**]). The one Riccati equation is solved for the optimal state feedback and the other equation solved for the state observer [**1**]. This provides a controller with state feedback and an observer for the unmeasured system outputs.

H_∞ control provides design freedom in selecting shapes of the individual weighting functions, as well as the weighting scheme. The weighting scheme selects the specific transfer functions to be shaped, and the weights shape the respective singular value plots. Unfortunately, the three block problem mixed sensitivity control has some drawbacks which will be explained in the next section.

[29] A system is detectable if all of its unobservable states are naturally stable [**20**].

4.3.2 Six block problem H_∞ control design

Standard three block problem mixed sensitivity control has one serious drawback: pole-zero cancellation. It aims to cancel poorly damped stable poles of the system with controller zeros, making the poorly damped poles unobservable and uncontrollable [**13**,**26**]. Furthermore, the controller designed using this method, contains the inverse of the plant, causing complications if the plant is non-invertible [**1**].

In order to bypass these problems another weighting scheme is applied, namely the *six block problem* weighting scheme [**2**]. This scheme includes the plant in the weighting of the sensitivity, preventing the inclusion of the inverted plant within the controller. In addition, the *six block problem* weighting scheme prevents pole-zero cancellation and makes the optimisation problem well-posed [**2**]. Apart from only weighting the standard S_o, KS_o, and T_o signals, the input disturbance sensitivity function (G_nS_i), and closed-loop transfer function from the plant input to the plant output (T_i) are also shaped. Thus a term, G_nS_i, involving the plant is included in the standard mixed sensitivity minimisation problem as given in (4.32) below.

$$\min_K \left\| \begin{matrix} W_e S_o W_r & -W_e G_n S_i W_d \\ W_u K S_o W_r & -W_u T_i W_d \\ W_y T_o W_r & W_y G_n S_i W_d \end{matrix} \right\|_\infty \tag{4.32}$$

As can be seen in (4.32), the standard weights W_e, W_u and W_y are present with the addition of two new weights, W_r and W_d. The weight W_r shapes the reference input, r, to the system, and W_d shapes (attenuates) the input disturbances. Weight W_d is important in preventing pole-zero cancellation [**26**]. The structure of the augmented (weighted) *six block problem* scheme is shown in Figure 4.3-4, where the inputs are $\boldsymbol{w} = [r, d]^T$ and $\boldsymbol{u} = [i_z, i_{ax}, i_{ay}, i_{ax}, i_{by}]^T$, and the outputs are $\boldsymbol{z} = [z_1, z_2, z_3]^T$ and $\boldsymbol{v} = [z_z, \mathrm{x_a}, y_a, x_b, y_b]^T$ with regard to the Fly-UPS.

The augmented system Figure 4.3-4 is then reformulated similar to the system shown in Figure 4.3-3. Hence the same procedure as explained in section 4.3.1 is followed in order to synthesise a controller using the six block problem. MATLAB®'s *Robust Control Toolbox* is used to solve the two Riccati equations and to synthesise the stabilising robust H_∞ controller [**14**]. However, selecting the weighting functions for the six block problem controller synthesis is not a trivial task and requires the designer to have sufficient understanding of the design requirements and constraints.

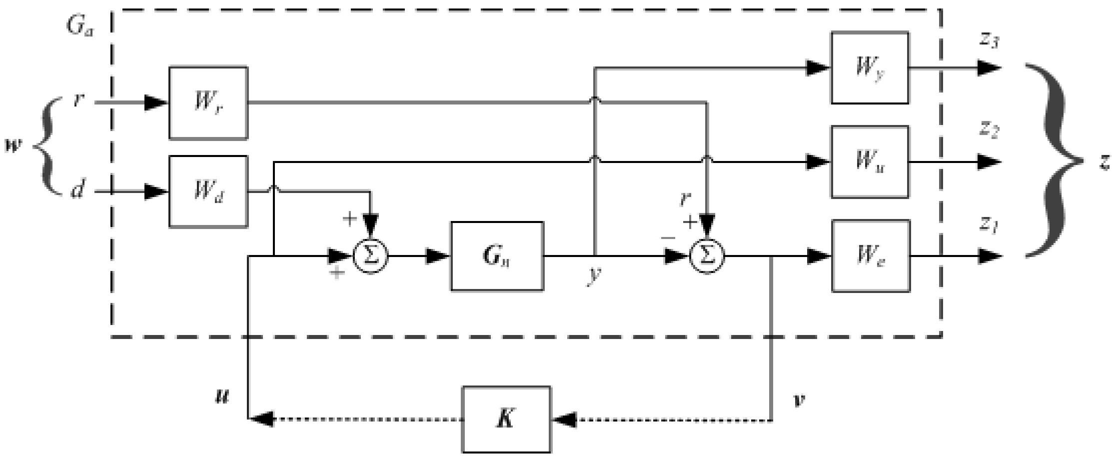

Figure 4.3-4: Augmented six block problem control scheme

4.3.3 Weighting function selection

Within the six block problem weighting scheme there are five weighting functions to be selected, namely: W_r, W_e, W_u, W_y and W_d. Each weighting function is created according to predefined specifications, requirements and constraints related to the AMB Fly-UPS system. As stated earlier, the weighting functions are mostly selected on *a priori* knowledge of the system or in a trial and error basis [**3**]. *Once the required transfer function shape is specified within the weighting function, the inverse of the weighting function is supplied for controller synthesis* [**11**]. This is done in order to 'guide' the minimisation of the H_∞ cost function. In this section, the requirement of each weighting function for the Fly-UPS system is explained and developed, starting with the reference signal weight.

Weight W_r plays a small part in shaping the sensitivity (S_o) and controller gain (KS_o). However, in order to simplify the rest of the weighting function selection, W_r is selected as a constant, with $W_r = 1$. This is generally suitable for flywheel systems that do not have a static stiffness requirement [**2**].

The error weight, W_e, shapes the sensitivity function (S_o). It may be possible to first obtain an initial controller using another design procedure, such as LQG, and using the resulting sensitivity to select an error weight [**2**]. However, this is not necessary because according to the proposed ISO standard in [**15**], the sensitivity for newly commissioned machines should be below 8 dB. Furthermore, in order to obtain an integration effect[30], the magnitude of the error

[30] The integration process in control reduces and eliminates the steady-state error caused by rotor sagging.

weight at frequencies below 1 Hz should be smaller than 0 dB. Thus, it would be adequate to select the weighting function as a first order high-pass transfer function with a pass-band gain of 8 dB cutting off frequencies below 1 Hz.

Weight W_u represents the controller gain (KS_o) and should be a small constant [**1**]. *However, as previously explained, in the case of additive uncertainty, the weight W_u is equal to the uncertainty bound W_Δ* [**10**]. This allows the inclusion of uncertainty compensation by replacing the weight W_u with W_Δ. Lastly, in order to implement controller roll-off, a low-pass transfer function with a bandwidth of 500 Hz is cascaded with the weighting function.

Transfer function W_y, shapes the complimentary sensitivity T_o. In order to keep the closed loop gain as close to unity as possible, W_y is selected as a first order low-pass transfer function with a 4 dB pass-band gain and a 5 kHz bandwidth.

Finally, W_d and W_e shape the input disturbance signal (G_nS_i), and W_d and W_u shape the input closed-loop transfer function (T_i). In order to obtain good input disturbance rejection, the weight W_d is chosen as a small constant of 10^{-4}. Hence, the combined weight $W_d \times W_e$ bounds the change in displacement to 200 μm for an input disturbance of 1 A, and the combined weight $W_d \times W_u$ bounds T_i to a gain of 6 dB.

It should be noted again that the weighting functions must be proper and stable to be solvable. The non-inverted singular value plots of the selected weighting functions are shown in Figure 4.3-5 (the uncertainty weights, W_u, were shown in section 4.2). The respective transfer functions for W_r, W_e, W_u, W_y and W_d are cascaded with diagonal unit matrices with dimension, 5x5, as follows:

$$
\begin{aligned}
\boldsymbol{W}_r &= 1 \times \boldsymbol{I}_{(5\times5)} \\
\boldsymbol{W}_e &= \frac{0.4s + 0.025}{0.16s + 1} \times \boldsymbol{I}_{(5\times5)} \\
\boldsymbol{W}_u &= \boldsymbol{W}_\Delta = \boldsymbol{I}_{(5\times1)} \times \begin{bmatrix} W_{\Delta axial} & W_{\Delta upper} & W_{\Delta upper} & W_{\Delta lower} & W_{\Delta lower} \end{bmatrix} \\
\boldsymbol{W}_y &= \frac{5.05\times10^{-7}s + 1.59}{3.18\times10^{-5}s + 1} \times \boldsymbol{I}_{(5\times5)} \\
\boldsymbol{W}_d &= 100\times10^{-6} \times \boldsymbol{I}_{(5\times5)}.
\end{aligned}
\tag{4.33}
$$

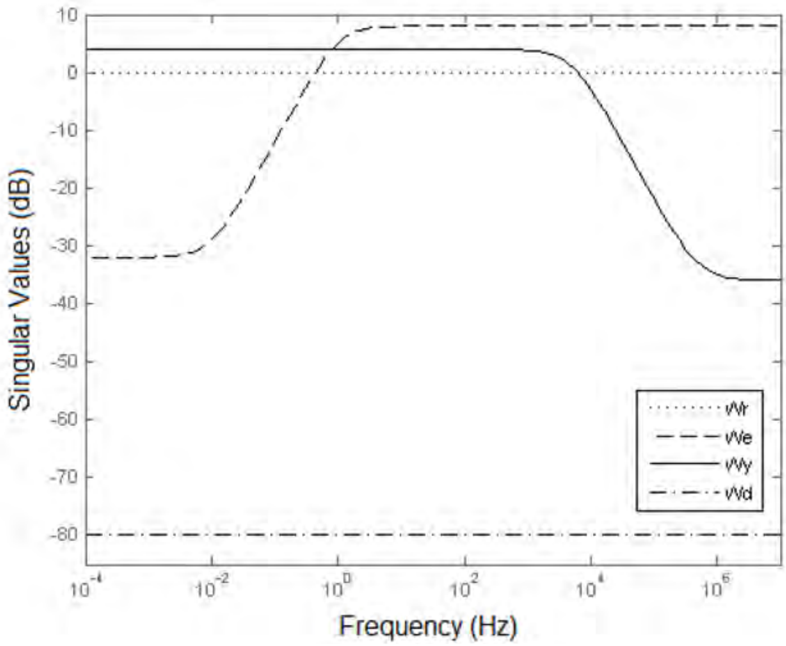

Figure 4.3-5: Weighting function singular value plots

4.3.4 Controller development

When using the specified weights an H_∞ controller was synthesised with MATLAB®'s *Robust Control Toolbox* using the *hinfsyn* function. The H_∞ controller suboptimal solution achieves a minimum condition number of $\gamma = 3.85$. This means that the synthesised controller is able to comply with all the required specifications (bounds) provided by the weighting functions to within 11.7 dB. It should be noted that the robustness to uncertainty is included as a performance weight, thus the controller is synthesised with both performance and stability robustness in mind.

However, the synthesised 5-DOF H_∞ state-space controller has an order of 75. This high order number is due to the model-based H_∞ controller having the same number of states as the plant and the weighting functions added together. This is impractical for most applications and in view of implementing the controller on the Fly-UPS system an order reduction of the controller is necessary. Furthermore, the large number of complex calculations involved in multivariable H_∞ control requires a high sampling frequency. The sampling frequency for the Fly-UPS is fixed at 10 kHz which, in turn, limits the order of any controller implemented on the hardware to a 19th order controller (due to hardware and stability constraints).

Thus it is necessary to reduce the 75th order controller to a 19th order controller. The reduction method used due to its reliability, is the balanced stochastic model truncation (BST) via Schur reduction (see [**14**] for details). The controller order is successfully reduced to a 19th order controller with a multiplicative error bound of less than 7%, mainly affecting the high frequency characteristics of the controller only. Figure 4.3-6 below shows the singular value plots of the reduced order multivariable H_∞ controller. The state-space values of the controller can be found in Appendix C.

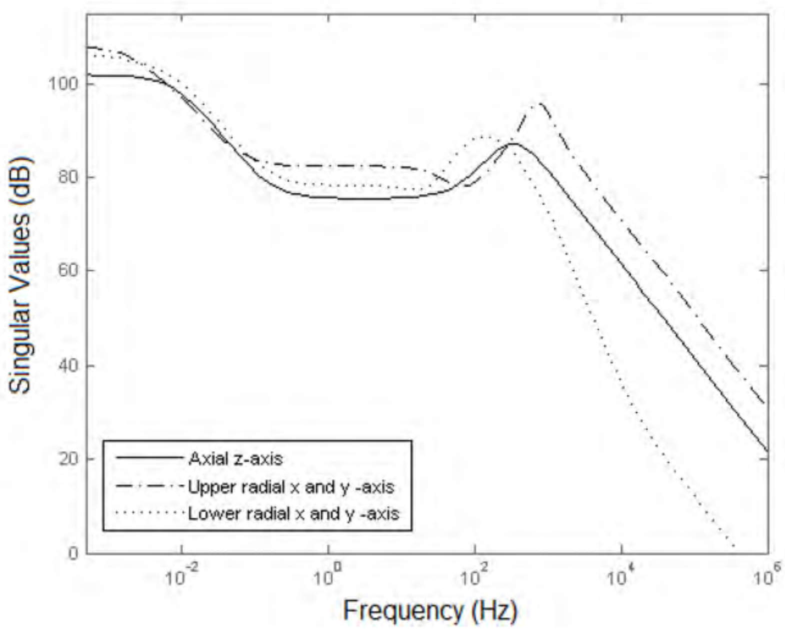

Figure 4.3-6: Singular value plot of the multivariable H_∞ controller

4.4 Conclusion

This chapter explains uncertainties and provides an introduction to robust control theory. The additive uncertainties between the nominal simulation model and the physical model at varied rotational speeds were characterised. Furthermore, the mixed sensitivity H_∞ control synthesis strategy was observed. Different weighting schemes are explained and the *six block problem* weighting scheme is used for H_∞ controller synthesis. A controller was synthesised with weighting functions relevant to the AMB Fly-UPS system and the controller reduced to a 19th order controller.

The experimental performance of the H_∞ controller will be verified and validated in the next chapter. Additionally, the controller will be implemented on the physical Fly-UPS system and the system response, stability robustness and performance robustness will be evaluated.

Chapter 5

Implementation, evaluation and results

This chapter includes the verification of the controller design as well as the physical implementation of the controller on the Fly-UPS system. The system response, stability robustness and performance robustness are evaluated. Finally, the results obtained are compared to the previous system controller in order to establish whether the new controller is an improvement or not.

5.1 Controller validation and verification in simulation

Following the model design in Chapter 3 and the uncertainty characterisation in Chapter 4, an H_∞ controller was synthesised. As a result, the experimental performance of the H_∞ controller on the physical AMB Fly-UPS system is now examined. However, before the controller is implemented on the physical system, the H_∞ controller specifications have to be verified and validated.

In Chapter 4, weighting functions were selected in order to shape and minimise the mixed sensitivity transfer functions in order to synthesise a controller. These weighting functions were selected using *a priori* insight into the Fly-UPS system requirements. Hence, the synthesised H_∞ controller should be able to satisfy the requirements specified by the weighting functions. In order to verify this, the synthesised *full order*[31] H_∞ controller is implemented on the LTI model of the Fly-UPS system developed in Chapter 3. From this simulation, certain theoretical predictions concerning the closed-loop system stability and sensitivity functions of the physical system can be made. For the sake of simplicity, only the *x*-axis of one of the radial AMBs will be used to verify the shaping of the system transfer functions.

The most important loops to be shaped by the controller are the system sensitivity, controller output and closed-loop transfer functions. It is important to remember that the synthesised controller conforms to the weighting specifications to within 11.7 dB and is only able to stabilise the Fly-UPS system to a rotational speed of 6400 r/min.

[31] The synthesised full 75th order controller is used for verification.

Figure 5.1-1 shows the system sensitivity at 0, 1000, 2000, and 5000 r/min. The sensitivity remains below the 8 dB level specified by the weighting function as required by [**15**]. The controller output including the weighting function is shown in Figure 5.1-2. It is clear that the controller shape closely matches the shape specified by the weight W_{Δ}. The closed loop system transfer function with its relevant weight is shown in Figure 5.1-3. Furthermore, according to MATLAB®'s stability robustness analysis (*robuststab*), the controller can tolerate up to 101% of the modelled additive uncertainty. Although some of the transfer functions are above their respective weighting function limits, the controller still conforms to the specified requirements. As a result, the full order controller is verified and found valid.

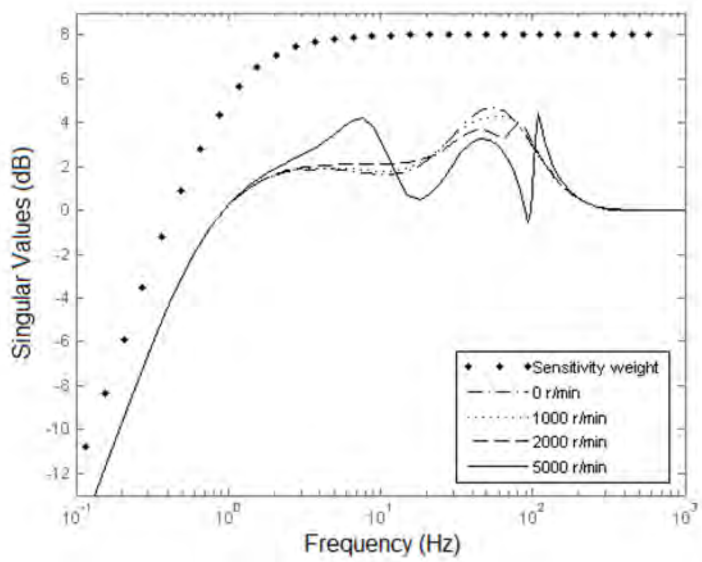

Figure 5.1-1: Model sensitivity with full order controller

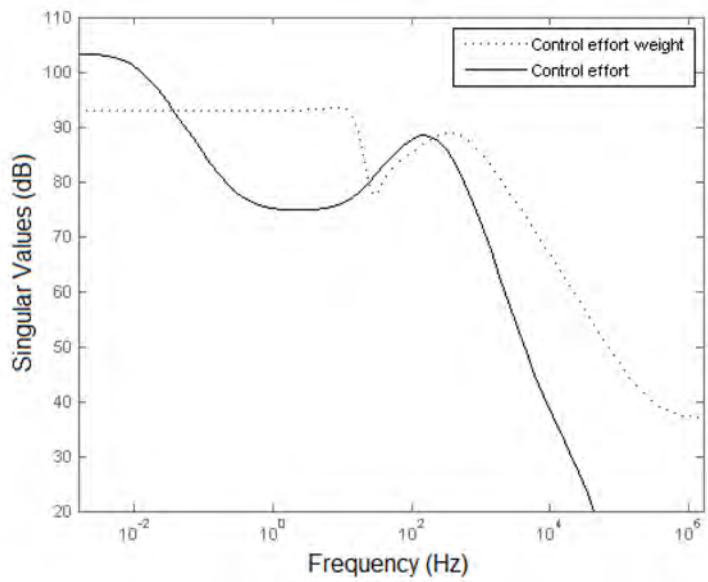

Figure 5.1-2: Control effort and relevant weight

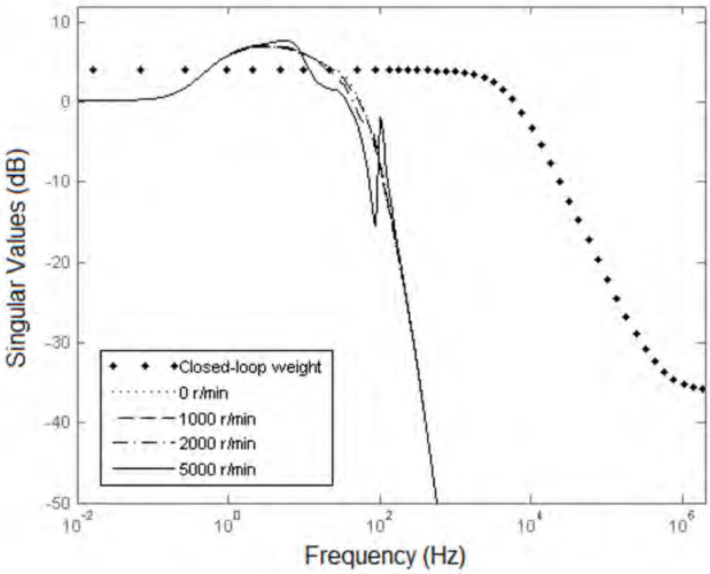

Figure 5.1-3: Closed-loop transfer function and weight

However, in order to implement the controller on the Fly-UPS, the full order controller has to be reduced to a 19th order controller. This is due to the physical hardware sampling frequency constraints mentioned in Chapter 4. Hence the sensitivity plots of the 19th order controller at the above mentioned rotational speeds are shown in Figure 5.1-4. Unfortunately, for the reduced order controller, the sensitivity is much higher and exceeds the weight specification, raising possible performance issues with the controller physically implemented on the Fly-UPS. This concern will be explored in the following section.

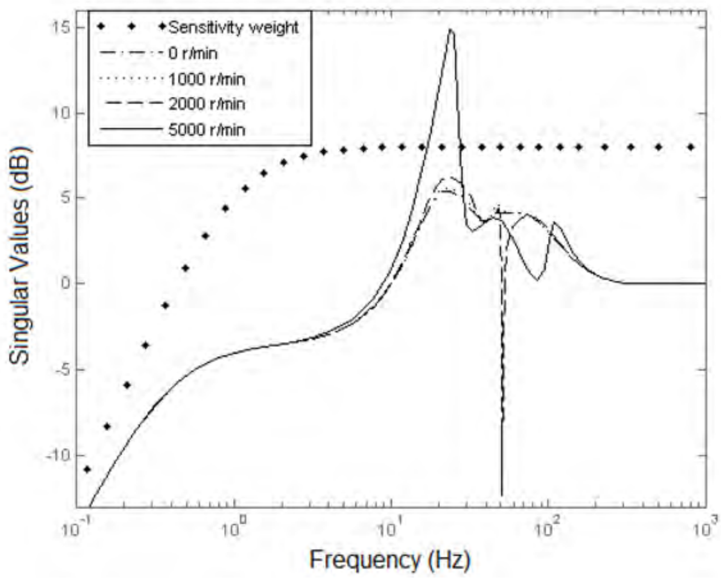

Figure 5.1-4: Model sensitivity with reduced order controller

5.2 Physical implementation

The 19th order controller synthesised in Chapter 4 is now implemented on the physical Fly-UPS system. MATLAB® is used for the real-time control scheme implementation via the MATLAB® xPC Target. There are three levels of implementing the controller on the physical system (Figure 5.2-1). First, the reduced controller is imported into a Simulink® model as seen in Figure 5.2-2. This is done in order to compile all the input/output functions of the Fly-UPS system, including the controller, for use with the hardware interface.

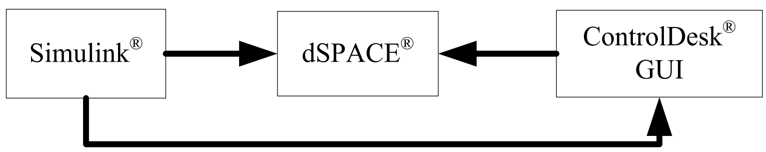

Figure 5.2-1: Fly-UPS implementation levels

The control system in Simulink® is compiled into optimised real-time C code which is downloaded onto a secondary hardware controller. The hardware controller used to implement the multivariable H_∞ controller is the dSPACE® control system[32]. The dSPACE® system interfaces the Simulink® environment with the physical hardware by means of input-output data cables. Furthermore, the dSPACE® system is used to interface the power amplifiers, eddy probe drivers, vacuum system and the motor drive unit with the main desktop computer. This allows real-time control of the Fly-UPS system using a desktop computer.

The Fly-UPS will be monitored in real time via dSPACE's ControlDesk®. ControlDesk® is dSPACE® software which enables the user to implement and monitor real-time control via a graphical user interface (GUI) [**4**]. Using the mentioned GUI, the position, current and rotational speed of the Fly-UPS can be monitored. The GUI for the rotor positions of the Fly-UPS is shown in Figure 5.2-3 with the lower radial AMB orbital plot on the left hand side, the upper radial AMB orbital plot in the centre and the axial AMB position on the right hand side.

Figure 5.2-4 shows all the AMB power amplifier current graphs on the left hand side, the main system controls in the centre and the motor current graphs on the right hand side.

[32] Specifications for the dSPACE® system can be found in [**4**] and [**34**].

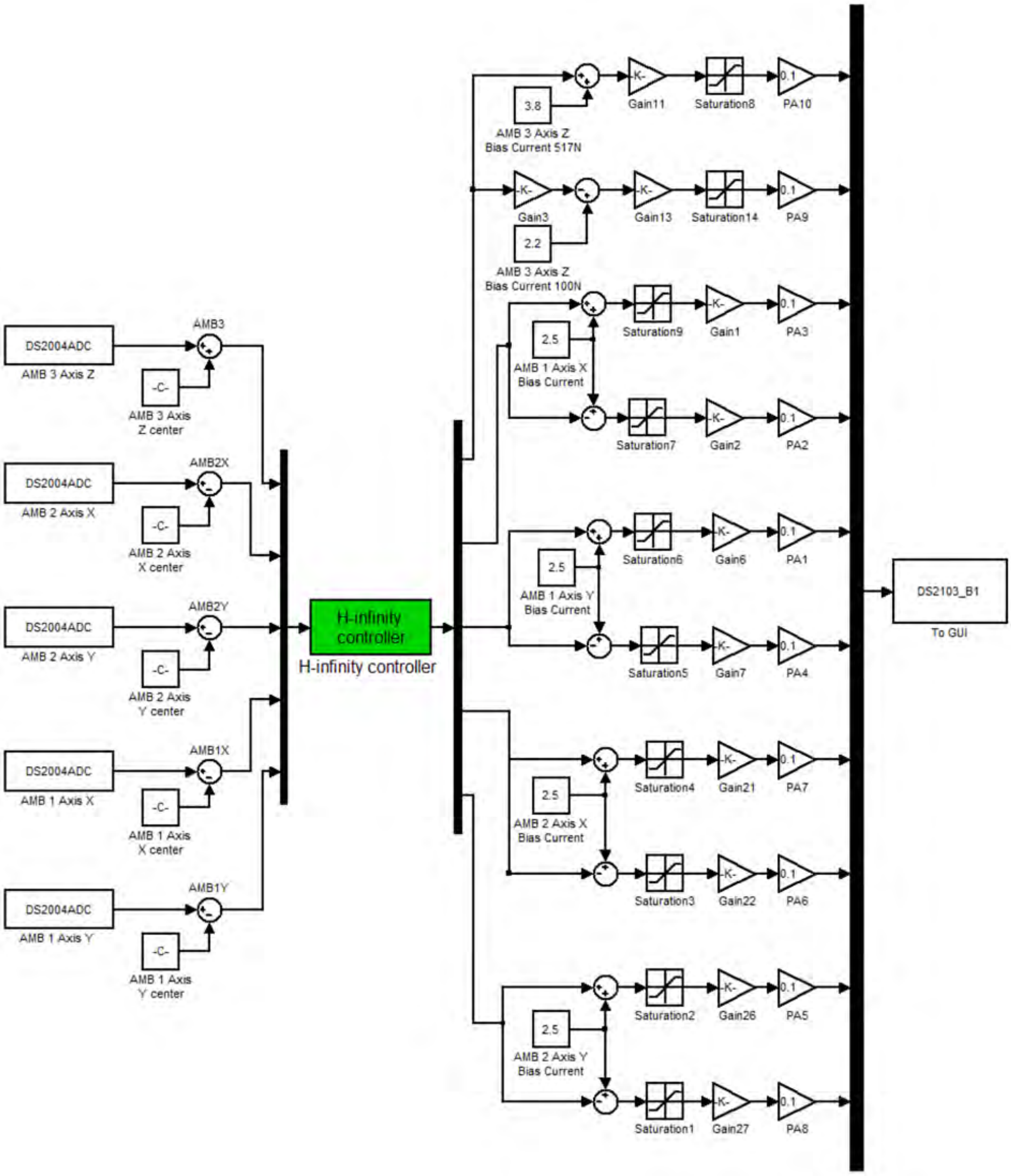

Figure 5.2-2: Simulink® model of the Fly-UPS

Images of the complete Fly-UPS system setup, including the desktop computer, the hardware controller, and the physical flywheel are shown in Appendix D. Once the controller is compiled, downloaded to the hardware controller, and linked with the GUI, testing and evaluation of the Fly-UPS system is possible. Whether the developed H_∞ controller satisfies both the performance and stability requirements is verified in the following sections.

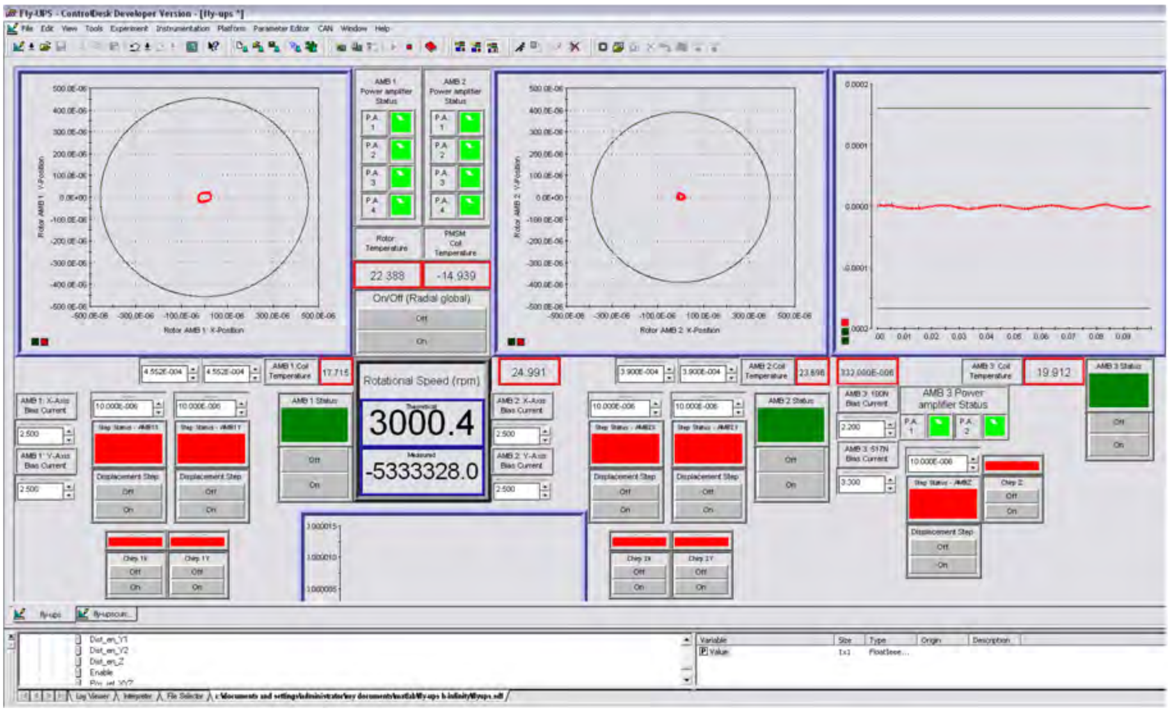

Figure 5.2-3: Fly-UPS rotor positions on ControlDesk® GUI

Figure 5.2-4: Fly-UPS AMB currents and controls on ControlDesk® GUI

5.2.1 Transient response evaluation

In order to test the transient response of the Fly-UPS system, a step reference input of 10 μm is injected consecutively to both the radial AMBs and the axial AMB. The step responses at stand-still of the lower radial AMB, upper radial AMB and axial AMB, are shown in Figure 5.2-5, Figure 5.2-6 and Figure 5.2-7 respectively. For the sake of simplicity, only the *x*-axes of the radial AMBs are shown. The difference in responses between the two radial AMBs is because the flywheel is closer to the upper AMB and thus the inertia and equivalent mass differs between the lower AMB (5.38 kg) and the upper AMB (13.22 kg) [**4**]. The H_∞ controlled plant shows satisfactory response times with the large steady-state errors reduced to near-zero by the controller's integration effect. The percentage overshoot (P.O.) before steady state error reduction of the lower radial AMB, the upper radial AMB, and the axial AMB is 66%, 46%, and 49% respectively.

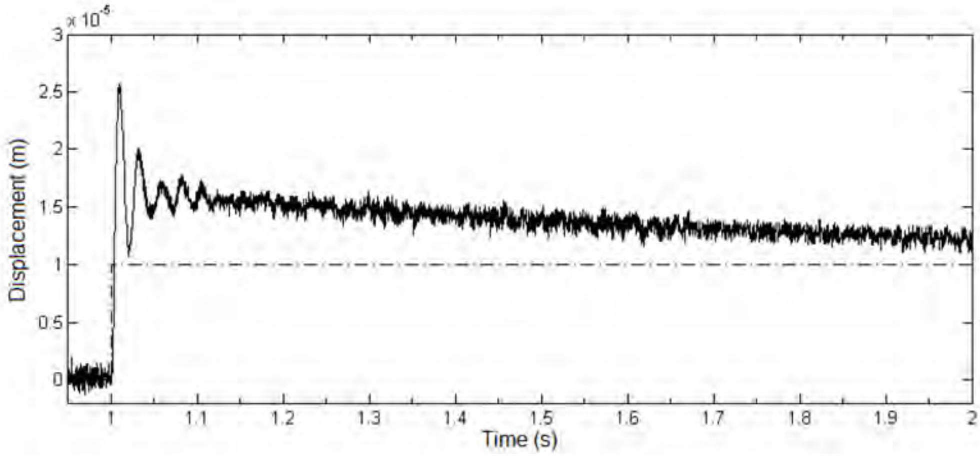

Figure 5.2-5: Lower radial AMB $\boldsymbol{H_\infty}$ step response

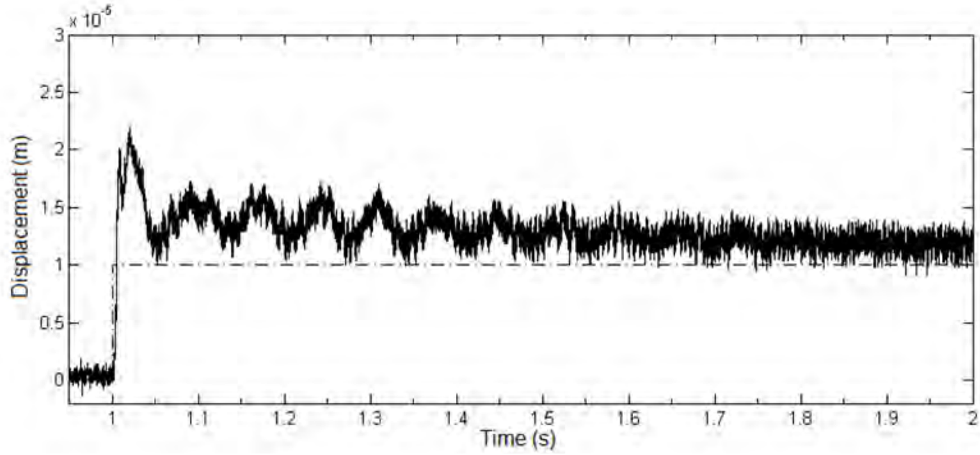

Figure 5.2-6: Upper radial AMB $\boldsymbol{H_\infty}$ step response

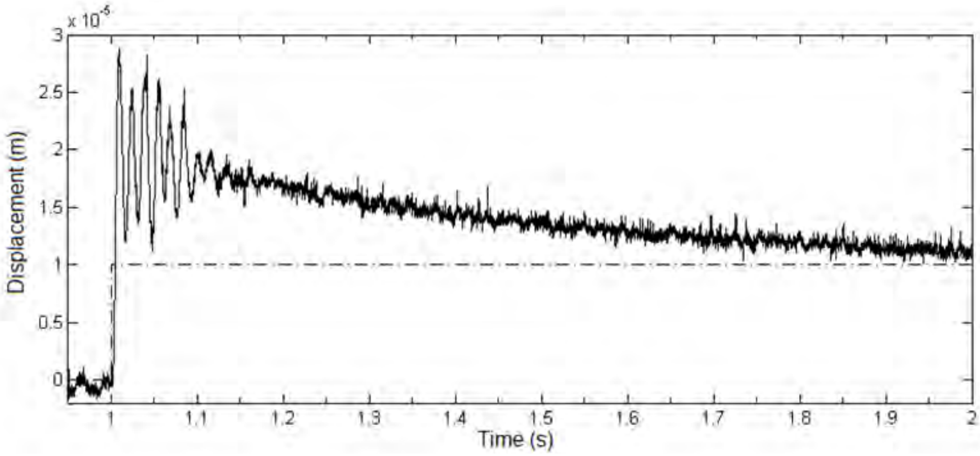

Figure 5.2-7: Axial AMB $\boldsymbol{H_\infty}$ step response

Furthermore, in order to compare the transient response as rotational speed changes, the 10 μm step responses of the upper radial AMB at 2000 r/min and 5000 r/min are shown in Figure 5.2-8 and Figure 5.2-9 respectively. The model of the Fly-UPS system decouples the axial AMB from the radial AMBs; therefore, the axial AMB is excluded from the rotational speed variation response plots. The high frequency oscillations (synchronous with the rotational speed) on both the transient responses are due to the rotor mass unbalance. It is clear that the controller maintains stability and relative performance throughout the rotational speed variation.

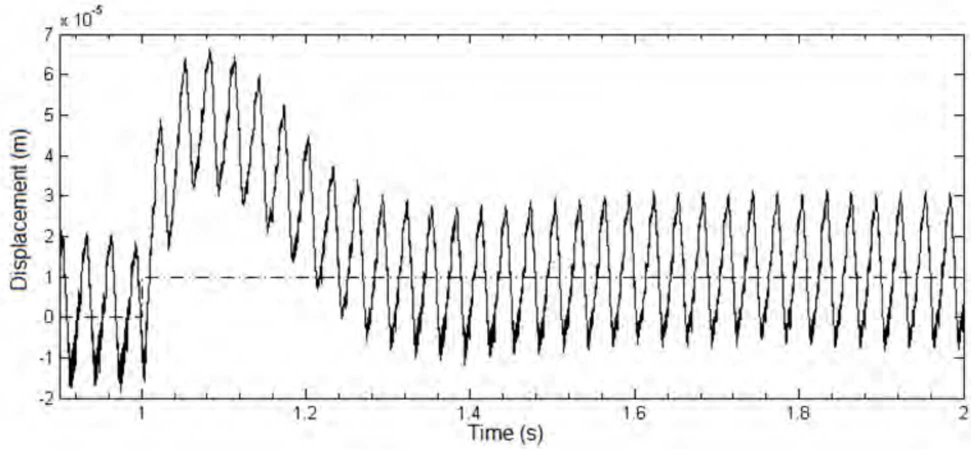

Figure 5.2-8: Radial AMB step response at 2000 r/min

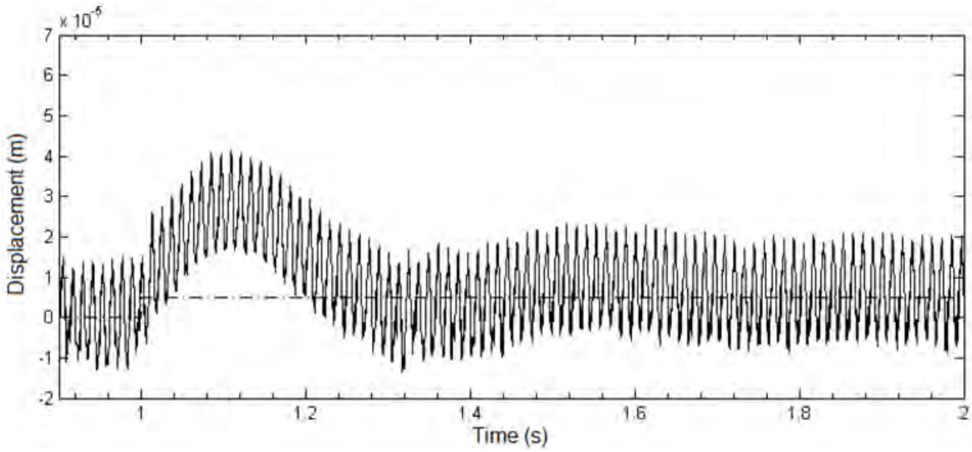

Figure 5.2-9: Radial AMB step response at 5000 r/min

For investigative purposes, the transient response of the H_∞ controller is put side by side to the transient response of the PD controller as specified and designed in Chapter 4 and in [**4**]. The PD controller has K_P, and K_D values of 10 000 and 10 respectively. Figure 5.2-10 below shows the 10 μm step responses of the x-axis of the upper radial AMB, controlled with H_∞ and PD controllers at standstill respectively.

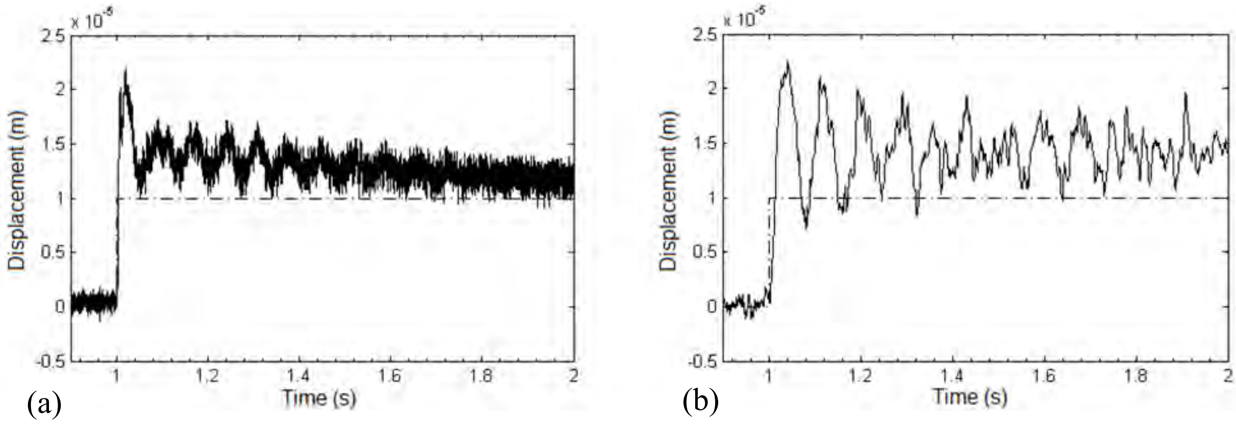

Figure 5.2-10: Comparative step response for (a) H_∞ and (b) PD controllers at standstill

It is clear that the H_∞ controller yields a faster response time as well as higher damping when compared to the PD controller. This clearly shows part of the advantage of using the H_∞ controller on the Fly-UPS system.

5.2.2 Performance robustness

The performance robustness is evaluated via the sensitivity function. The sensitivity function is the stability and performance evaluation method suggested by the proposed ISO CD 14839-3 standard for AMBs. The sensitivity function is suggested because it is relatively simple to measure and shows the sensitivity of AMBs to disturbances of different frequencies [**15**].

The sensitivity can be tested by injecting the closed loop system with a harmonic or sinusoidal disturbance at the same place as a reference signal would be added, and then measuring the response signal directly behind the injection point (Figure 5.2-11). This is done for each separate rotor input and the magnitude of the response of the rotor, due to the disturbance signal, provides the sensitivity function [**15**].

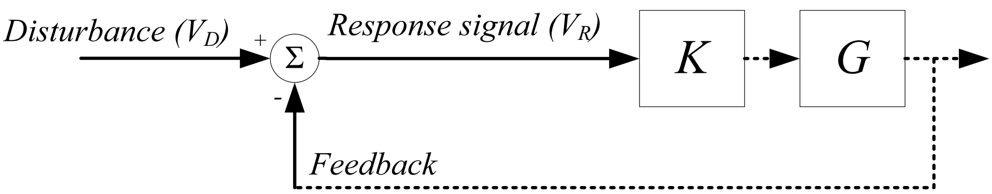

Figure 5.2-11: Sensitivity disturbance injection point

The sensitivity function, S, is then:

$$S = 20\log\left(\frac{V_R}{V_D}\right) \tag{5.1}$$

where V_D and V_R are the disturbance input and response signals respectively.

The proposed ISO CD 14839-3 standard requires the sensitivity to be characterized up to 2 kHz or a frequency of three times the rated speed, depending on whichever is the highest. For the Fly-UPS the sensitivity analysis will be done up to a frequency of 2 kHz, because three times the rated speed (25 000 rpm) is only 1.25 kHz. The worst measured sensitivity among the axes determines the system's overall sensitivity.

The proposed ISO CD 14839-3 standard provides four rating zones for characterizing sensitivity. This is given in Table 5.2-1 below [**15**]:

Table 5.2-1: Sensitivity ratings [**15**]

Zone	Peak sensitivity
A/B	8 dB
B/C	12 dB
C/D	14 dB

Zone A: The sensitivity of new machines normally falls within this zone.

Zone B: These machines are considered acceptable for unrestricted long-term operation.

Zone C: Machines in this zone are considered unsatisfactory for long-term continuous operation. Remedial action is required.

Zone D: Sensitivity within this zone is normally severe and can cause damage to the machine.

The sensitivity, *S*, and the 8 dB limit (zone A) of the lower radial AMB and the upper AMB at stand-still are shown in Figure 5.2-12 and Figure 5.2-13 respectively. The *x*-axis and *y*-axis sensitivity functions are alike; hence only sensitivity plots of the *x*-axes are shown. From the respective figures, it is clear that the sensitivity plots of the AMBs at standstill are above the 8 dB bound at specific frequencies. However, the sensitivity still remains below 12 dB, rating the system as a zone B system making it acceptable for short- to medium-term operation only. The reason for this high sensitivity will be explained shortly. The system rating is specified using sensitivity plot information of the radial AMBs at standstill only, due to the fact that the system is unable to rotate at the nominal design speed of 25 000 r/min.

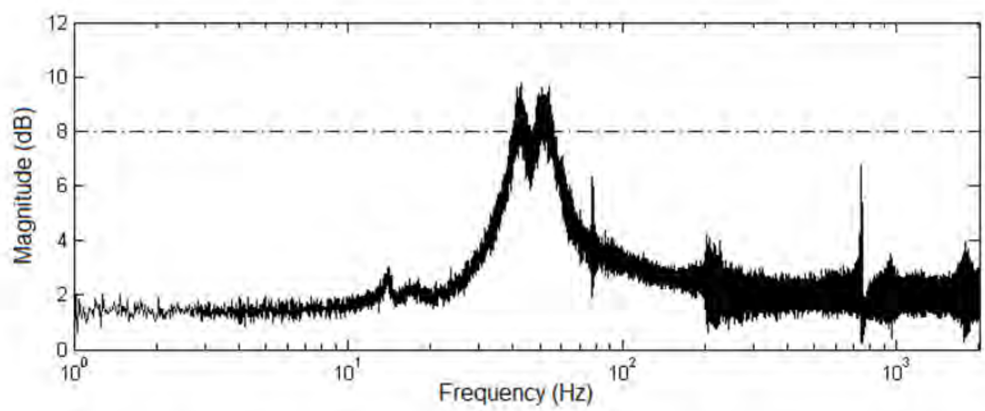

Figure 5.2-12: Lower radial AMB sensitivity at standstill

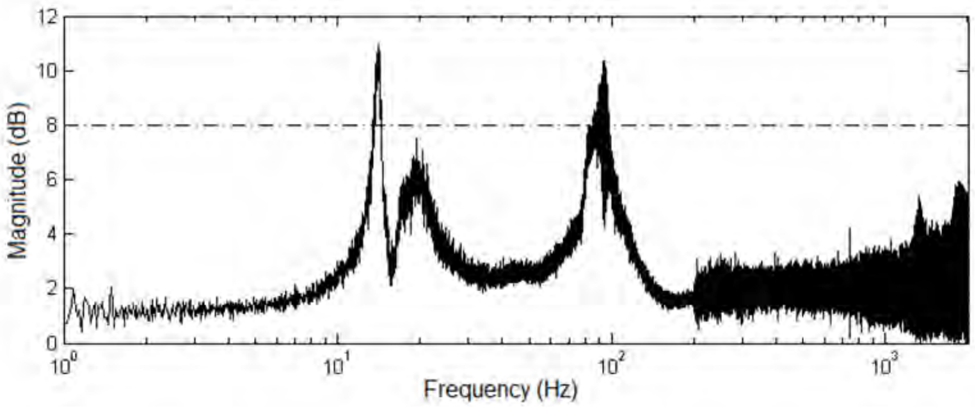

Figure 5.2-13: Upper radial AMB (near flywheel) sensitivity at standstill

Figure 5.2-14 and Figure 5.2-15 show the sensitivity of the two radial AMBs at 5000 r/min. The large spike in sensitivity at 83 Hz in both figures is the synchronous rotational unbalance coinciding with 5000 r/min. However, the low frequency sensitivity of the upper radial AMB is so high at 5000 r/min (when compared to PD control) that the system is rated within zone D. This indicates the proximity to the cyclic instability mentioned in Chapter 4 and observed at 6400 r/min. Consequently, the high sensitivity is due to the conservativeness of the uncertainty bound, the controller order reduction as well as system non-linearity.

The additive uncertainties defined in Chapter 4 have large low frequency peaks due to the cyclic oscillation phenomenon (section 4.2.6) which in turn induces large dynamic low frequency displacements. Due to these large peaks in the uncertainty functions[33], the performance of the Fly-UPS system at 5000 r/min is greatly reduced. Furthermore, by reducing the order of the controller to a 19th order controller the performance degradation is significant, as predicted in section 5.1. This can be seen in the sensitivity function far exceeding the 8 dB threshold at lower frequencies, especially as the rotational speed increases.

[33] Large uncertainty bounds lead to more conservative uncertainty compensation, trading performance for robustness [**24**].

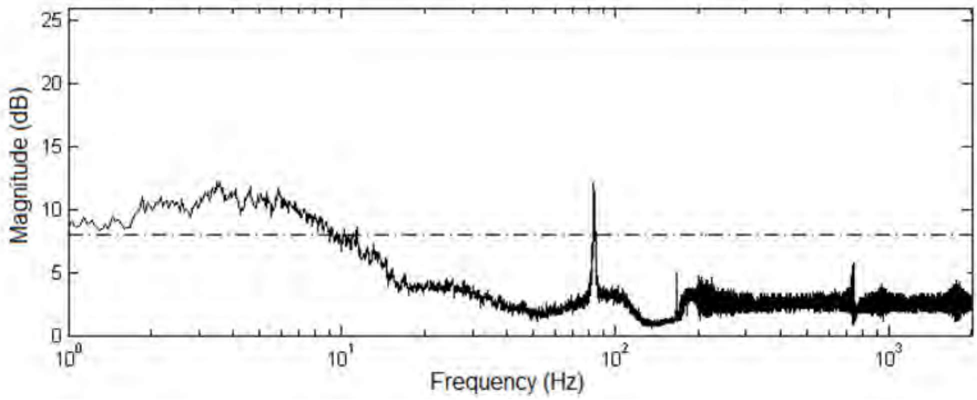

Figure 5.2-14: Lower radial AMB sensitivity at 5000 r/min

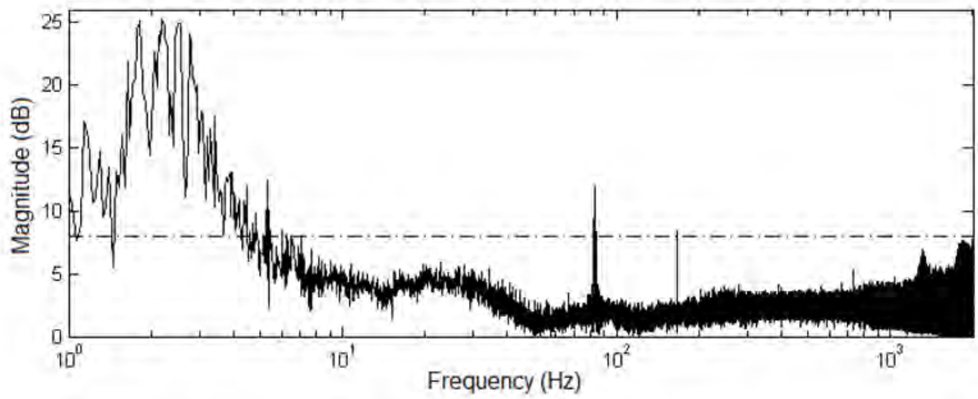

Figure 5.2-15: Upper radial AMB (near flywheel) sensitivity at 5000 r/min

Although the control algorithm achieves a condition number of 3.85, there are certain transfer functions that are far above the recommended sensitivity requirements. This shows that the robust performance requirement has not been achieved and that the system does not preserve the performance as specified by the weighting functions. However, the H_∞ controller still achieves better sensitivity when compared to the PD controller as specified in Chapter 4 and in [**4**]. The PD controller has the same K_P, and K_D values of 10 000 and 10 as in the previous section. The sensitivity plots of the two radial AMBs using the PD controller at standstill are shown in Figure 5.2-16 and Figure 5.2-17 respectively. It is clear that, the H_∞ controlled plant achieves a lower sensitivity threshold than the PD controlled plant at standstill.

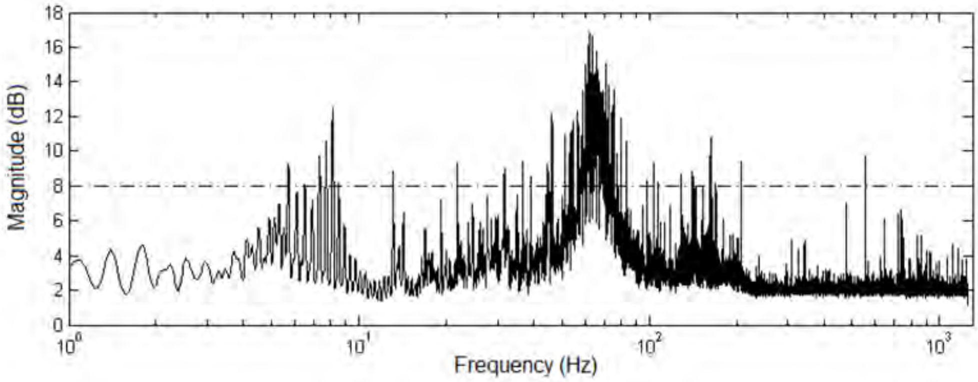

Figure 5.2-16: PD controlled lower radial AMB sensitivity at standstill

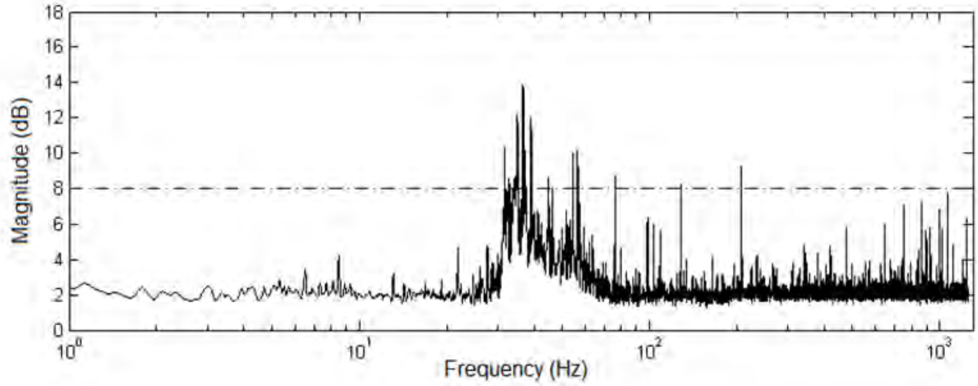

Figure 5.2-17: PD controlled upper radial AMB sensitivity at standstill

Figure 5.2-18 and Figure 5.2-19 show the sensitivity plots of the PD controlled plant at 5000 r/min. At 5000 r/min the PD controlled plant has high peak sensitivity especially at higher frequencies when compared to the H_∞ controlled plant.

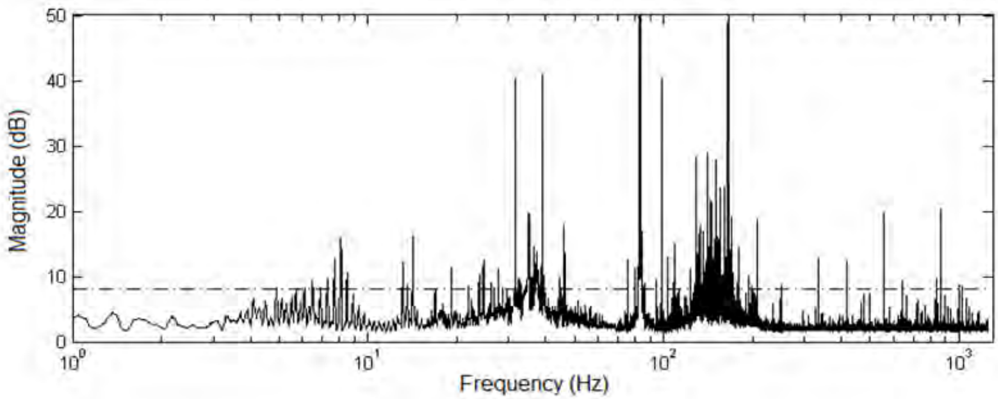

Figure 5.2-18: PD controlled lower radial AMB sensitivity at 5000 r/min

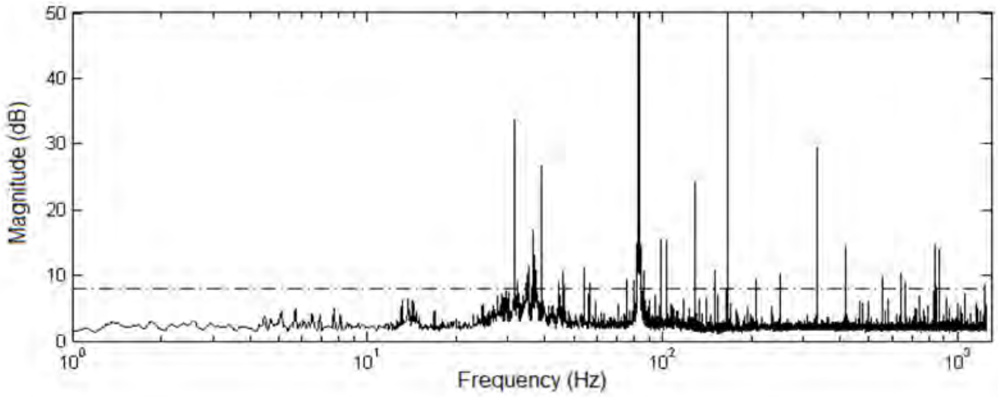

Figure 5.2-19: PD controlled upper radial AMB sensitivity at 5000 r/min

5.2.3 Stability robustness

As discussed in Chapter 4, the stability robustness requirement is included in the controller design as a performance optimisation problem. Hence the stability requirements are provided as additive uncertainty bounds within the controller synthesis. It is thus important to analyse whether or not the 19th order implemented H_∞ controller provides robust stability.

It should be kept in mind that the additive uncertainty bounds are only characterised for a rotational speed up to 5000 r/min, due to the PD controlled Fly-UPS system destabilising effect. Therefore, the stability robustness expectation is valid for rotational speeds up to 5000 r/min only.

It should be noted that the H_∞ controller is able to robustly stabilise the Fly-UPS system up to 6400 r/min, 1400 r/min higher than the robust stability specification and the speed that the PD controllers could manage. Figure 5.2-20 shows the orbital plots of the radial AMBs of the Fly-UPS system at 6400 r/min, just before becoming unstable.

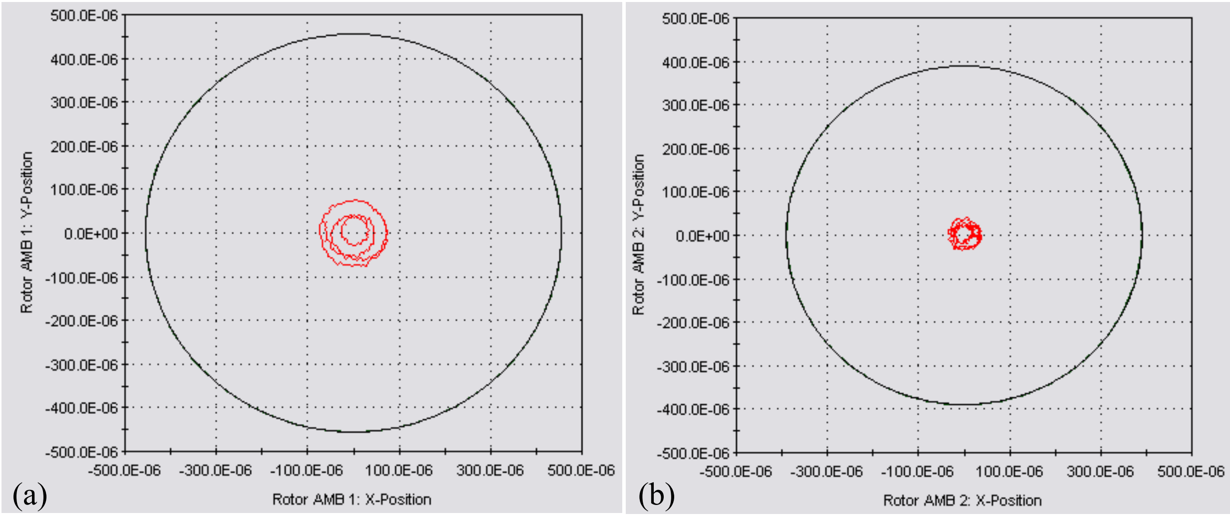

Figure 5.2-20: Orbital plots of lower (a) and upper (b) radial AMBs at 6400 r/min

Robust stability can be verified by observing the Fly-UPS system's closed-loop gain and phase margins. Although the generalised Nyquist stability criterion or Nichols chart M-circles are usually used for MIMO systems [**14**], it is not applied in this case due to physical implementation and data logging constraints. Instead, the classical gain/phase margin analysis for each feedback loop in the multivariable feedback system is done. In order to make the results applicable to the multivariable nature of the Fly-UPS system, the single, smallest gain/phase margin between all 5-DOF at the different recorded rotational speeds is taken as the system's gain/phase margin. *Hence the single representative worst-case gain/phase margin serves as the stability robustness evaluation criteria* [**14**]. This method, however, is not entirely suitable for multivariable systems and may be prone to shortcomings, requiring that the proper method be addressed in future work. The worst-case gain/phase margin of the Fly-UPS system is shown in Figure 5.2-21. The gain margin achieved is 11 dB and the phase margin is 13°, showing system robustness.

Furthermore, the closed-loop forward path gain of the H_∞ controlled Fly-UPS system is tested by inserting an adjustable gain in the forward path of the Simulink® system and adjusting the value until the system becomes unstable. The implemented H_∞ controller tolerates minimum and maximum forward path gains of 0.4 and 2.5 respectively, before the system becomes unstable. As a result, the implemented H_∞ controller robustly stabilises the Fly-UPS system for a large range in forward path gain.

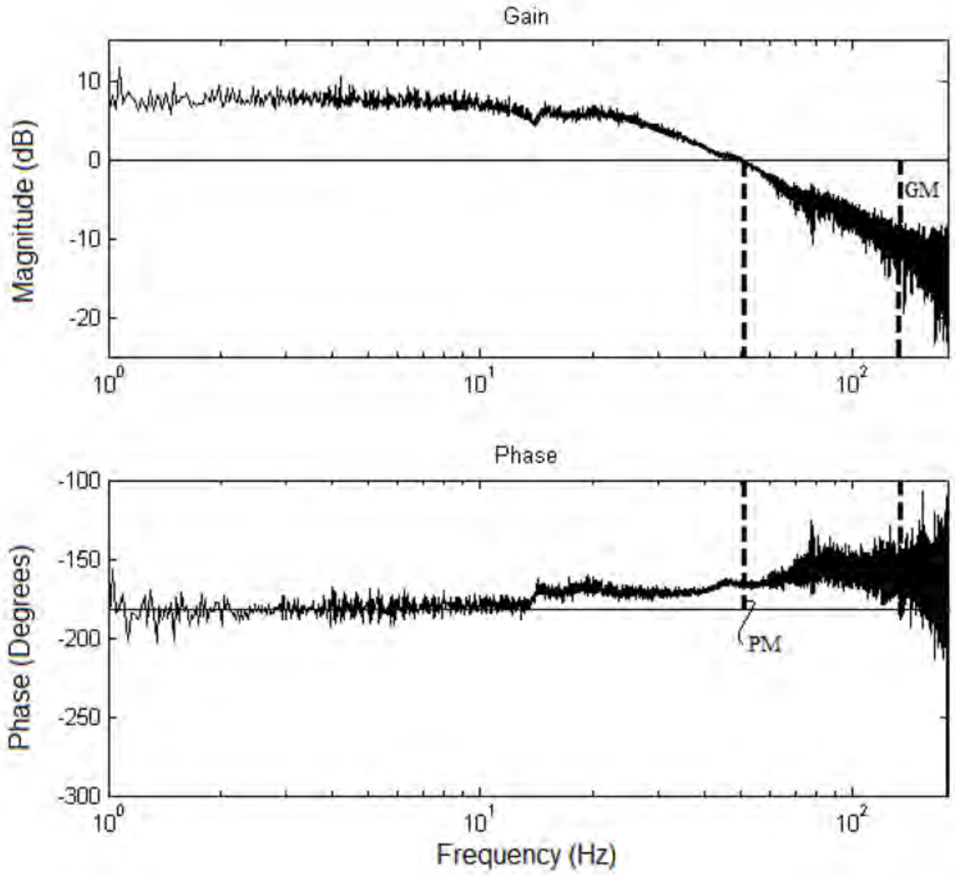

Figure 5.2-21: Worst-case gain/phase margin of the Fly-UPS system across all speeds

5.3 Conclusion

This chapter includes the verification of the controller design as well as the physical implementation of the controller on the Fly-UPS system. The experimental performance of the H_∞ controller is verified and validated and the controller is implemented on the physical Fly-UPS system. The synthesised controller proved stability robustness against rotational speed variation by providing stable system responses for all axes of freedom. It also robustly tolerated a rotational speed variation of up to 6400 r/min. Furthermore, the controller performance was evaluated according to the proposed ISO CD 14839-3 standard. The controller was unable to successfully comply with the performance specifications and was found lacking in sensitivity attenuation. Finally, the results obtained are compared to the previous PD controllers of the system and it is established that the H_∞ controller provides an improvement. The next chapter concludes this dissertation based on experimental results and provides recommendations for future work.

Chapter 6

Conclusion and recommendations

In this chapter, conclusions are drawn from the experimental results obtained in the previous chapter. An overview of the model development, controller synthesis and experimental implementation is provided. Furthermore, recommendations for future work on the controller, model, robustness requirements and system implementation are made.

6.1 Summary

The Fly-UPS design is subject to various uncertainties including changing system dynamics with varying rotational speed. Thus, stability robustness and performance robustness are the primary feedback requirements. In this dissertation a multivariable robust H_∞ controller for an active magnetic bearing flywheel system (Fly-UPS) was developed. A linear time invariant (LTI) model of the Fly-UPS system was successfully developed for use in H_∞ control synthesis.

The additive model uncertainties between the linear model, physical system and varying rotational speeds were characterised. These uncertainty bounds were included in the controller synthesis with the performance weights as performance optimisation problems. Furthermore, the *six block problem* weighting scheme for H_∞ control synthesis was investigated and implemented.

Each weighting function used in the controller synthesis was fully characterised and designed. Finally an H_∞ controller was synthesised using two Riccati equations. The synthesised controller was reduced to a 19th order controller and implemented on the physical Fly-UPS system.

6.2 Limitations and recommendations for future work

6.2.1 Model improvements

The model used for synthesising the H_∞ controller was a low-order, linear, rigid-body, analytical model. This limits the accuracy and included characteristics of the representative model. Techniques such as system identification, finite element analysis, and experimental modal analysis would more accurately model the Fly-UPS system. Furthermore, techniques such as linear parameter varying (LPV) and non-linear modelling can be investigated. This would decrease modelling error, and consequently system uncertainty, and most likely improve overall H_∞ control performance and stability robustness [**23**].

6.2.2 Controller order reduction

Unfortunately by reducing the order of the controller to a 19th order controller greatly reduced the controller performance. This was verified in Chapter 5 by comparing the simulation sensitivity of the 19th order controller with that of the full order controller. Possible solutions are to implement another controller reduction method, or implement a higher order controller by adjusting physical system parameters in order to lower the sampling frequency and thus obtain a higher order controller. This is stated on the basis that the Simulink® system parameters (hardware controller) limit the sampling frequency which in turn limits the controller order.

6.2.3 Performance robustness: weighting function selection

The performance robustness of the H_∞ controller is directly dependent on the specification of the weighting functions. The weighing functions shape the system loops, which characterises the system performance. Therefore accurate specification of the performance weights, relevant to the Fly-UPS system, would greatly increase the system performance [**11**].

Furthermore, the uncertainty weight is included as a performance weight in the control synthesis problem. Therefore, if the uncertainty is overly conservative or inaccurate, the system performance is greatly reduced by the controller overcompensating for robustness. Improved uncertainty weight specification would improve system performance.

In addition to the above mentioned issues, the following factors may have an effect on the overall performance of the Fly-UPS system [**2**]:

- Speed dependent characteristics: The rotation of the flywheel produces speed dependent dynamics such as gyroscopic effects and cross-coupled stiffness.
- Flexible modes: The elastic modes of the Fly-UPS system can adversely affect the performance because these modes are not included in the linear rigid rotor model.
- Synchronous vibration: A large unbalance in the Fly-UPS rotor acts as a disturbance, causing synchronous vibration that adversely affects the system performance.
- Order reduction: By significantly reducing the order of the controller, many of the high order performance robustness characteristics of the controller are lost.

6.2.4 Stability robustness: uncertainty bound specification

Robust stability of the system was achieved, although there are certain factors that greatly influence the overall stability robustness of the Fly-UPS system namely [**2**]:

- Model accuracy: The greater the difference between the model and the physical system, the greater the uncertainty would be, increasing the range of robustness requirements.
- Reassembly differences: Each time the system is disassembled and reassembled there are slight component placement differences. These differences can have a large effect on the system stability [**27**].
- Open-loop nature: The open-loop unstable nature due to the negative stiffness of the Fly-UPS produces limitations on the closed-loop stability.
- Cross-coupled stiffness[34]: The cross-coupled stiffness within the Fly-UPS as rotational speed varies is a major factor in destabilising the system.

By improving the accuracy with which the modelling differences are specified, the system stability robustness can be improved. For example, the individual parameter variations can be characterised, leading to structured (parametric) uncertainty. This would enable the use of μ-analysis or even μ-synthesis control development [**24**]. Therefore, by increasing the modelling accuracy, the uncertainty between the model and physical system would decrease; improving the uncertainty bound specification, and consequently the system robustness.

[34] Cross-coupling represents the coupling between the *x*-*y* axes, as well as the upper - lower *x*-*x*, *y*-*y* axes.

6.2.5 Controller improvements

The H_∞ controller successfully suspended the Fly-UPS system. However, there are certain extensions to the standard multivariable controller that may largely improve the overall system performance. These suggestions can be addressed in future work.

6.2.5.1 Feed-forward control

The Fly-UPS system is prone to synchronous unbalance force vibrations. By adding a feed-forward controller to the standard feedback system, the synchronous unbalance force vibration could be reduced or eliminated. By tuning the feed-forward controller, the Fly-UPS system can be suspended at the rotor's centre of mass. This would mostly eliminate system vibration and reduce the required control currents and consequently reduce actuator saturation.

6.2.5.2 Gain-scheduled H_∞ control

The Fly-UPS system is a system with varying rotational speed and changing system dynamics. This change in rotational speed and gyroscopic effects, influence the system performance. By implementing a gain-scheduled controller with rotational speed as the scheduling variable, a different controller depending on the instantaneous rotational speed of the system would be implemented [**17**]. This could optimise the overall system performance, as the gyroscopic effects at specific critical speeds would be taken into account.

6.2.5.3 μ-synthesis

H_∞ control synthesis is very similar to μ-synthesis, with the exception of structured uncertainty and iterative controller optimisation. Therefore, if the system uncertainty is well known and characterised with less conservative structured uncertainty, a μ controller can be synthesised. Since the uncertainty is well known and less conservative, and the controller is iteratively optimised, the controller synthesised using μ-synthesis will perform better [**1**].

6.2.5.4 Non-linear control

The physical Fly-UPS system, as is the case with most real world systems, is non-linear. Investigating the development of a non-linear model and consequently a non-linear controller is necessary in order to accurately represent and control the physical Fly-UPS system.

6.3 Conclusion

This project aimed to synthesise an H_∞ controller from a linear model of the Fly-UPS system and implement the synthesised controller. The multivariable controller had to control all five-degrees-of-freedom, the lower radial x- and y-axes, the upper radial x- and y-axes and the axial z-axis. Furthermore, the controller had to provide robust stabilisation and robust performance. The uncertainty bounds were specified for stability robustness implementation and weighting functions were devised for performance robustness specification. From the results obtained throughout this document, it is clear that the goals of this project have been reached. The system is robustly stable to plant parameter and rotational speed variation, within limits of the uncertainty bound specification. However, the performance specification was not achieved due to controller order reduction, synchronous unbalance and cyclic oscillatory behaviour.

One of the setbacks of H_∞ control is that the weighting functions are chosen on a trial and error basis. By improving the accuracy of the weighting functions by heuristic algorithms, intelligent model identification methods or any other identification method, the system performance and robustness can be improved.

It should be pointed out that at low rotational speed ranges the H_∞ controller is basically a classical PID controller [**23**]. However at higher rotational speeds, it is used to control the rigid modes with additional characteristics in order to cope with the uncertainty within the system [**24**]. This implies that classical control methods would almost be just as effective. Nonetheless, H_∞ control has the advantage that it provides a systematic and lucid design procedure as well as the ability to compensate for highly coupled multivariable systems, where in classical control the task of tuning the controller to compensate for multivariable systems is not a trivial task. Therefore, robust H_∞ control design provides a systematic tool to develop a multivariable controller that provides performance and stability robustness, with the advantage of specifying and shaping the design requirement trade-offs.

This project may serve as the foundation for further investigation into the feasibility of advanced control algorithms when applied to the Fly-UPS AMB system.

Appendices

Appendix A: Mathematical Notations

A.1 Singular values:

Definition: *Consider a matrix* $\boldsymbol{A} \in \mathbb{C}^{m \times n}$ *and* $k \underset{def}{=} \min(m,n)$. *The singular values* $\sigma_i,\ i = 1,\ldots,k$ *of* $\boldsymbol{A}$ *are the positive square roots of the k largest eigenvalues* $\lambda_i(\boldsymbol{A}^H \boldsymbol{A})$ *of the matrix* $\boldsymbol{A}^H \boldsymbol{A}$, *where* $\boldsymbol{A}^H$ *is the transpose of the conjugate of* $\boldsymbol{A}$, $\boldsymbol{A}^H = (\boldsymbol{A}^*)^T$ [**1**]:

$$\sigma_i(\boldsymbol{A}) \underset{def}{=} \sqrt{\lambda_i(\boldsymbol{A}^H \boldsymbol{A})}. \tag{A.1}$$

The singular values are often ordered such that $\sigma_1 \geq \sigma_2 \geq \ldots \sigma_k > 0$, with the largest singular value σ_1 being denoted $\bar{\sigma}(\boldsymbol{A}) = \sigma_1(\boldsymbol{A})$, and the smallest singular value σ_k denoted $\underline{\sigma}(\boldsymbol{A}) = \sigma_k(\boldsymbol{A})$ [**14**].

In multivariable systems, the gain not only depends on the frequency, but also on the direction [**28**]. The maximum gain of the system ***G*** as the input is varied is the maximum singular value of ***G***,

$$\max_{\boldsymbol{d} \neq 0} \frac{\|\boldsymbol{Gd}\|_2}{\|\boldsymbol{d}\|_2} = \max_{\|\boldsymbol{d}\|_2 = 1} \|\boldsymbol{Gd}\|_2 = \bar{\sigma}(\boldsymbol{G}) \tag{A.2}$$

and the minimum gain of the system ***G*** as the input is varied is the minimum singular value of ***G*** [**10**],

$$\min_{\boldsymbol{d} \neq 0} \frac{\|\boldsymbol{Gd}\|_2}{\|\boldsymbol{d}\|_2} = \min_{\|\boldsymbol{d}\|_2 = 1} \|\boldsymbol{Gd}\|_2 = \underline{\sigma}(\boldsymbol{G}). \tag{A.3}$$

Singular Value Decomposition (SVD):

Definition: *Any complex* $l \times m$ *matrix* $\boldsymbol{A}$ *may be factorized using the SVD*

$$\boldsymbol{A} = \boldsymbol{U}\ \boldsymbol{\Sigma}\ \boldsymbol{V}^H \tag{A.4}$$

where the $l \times l$ *matrix* $\boldsymbol{U}$ *and the* $m \times m$ *matrix* $\boldsymbol{V}$ *are unitary, and the* $l \times m$ *matrix* $\boldsymbol{\Sigma}$ *contains a diagonal matrix* $\boldsymbol{\Sigma}_1$ *of real, non-negative singular values,* σ_i, *arranged in a descending order as in*

$$\boldsymbol{\Sigma} = \begin{bmatrix} \boldsymbol{\Sigma}_1 \\ 0 \end{bmatrix};\ l \geq m, \tag{A.5}$$

where $\boldsymbol{\Sigma}_1 = diag\{\sigma_1, \sigma_2, \ldots, \sigma_k\}$, $k = \min(l,m)$ *and* $\bar{\sigma} \equiv \sigma_1 \geq \sigma_2 \geq \ldots \sigma_k > \equiv \underline{\sigma}$.

Advantages of using SVD over eigenvalues in analyzing gains and directions in multivariable systems are:

- Singular values provide more information about plant gains.
- The system directions obtained from SVD's are orthogonal.
- And finally, SVD's apply to non-square plants.

A.2 Norms of Vectors, Matrices and Systems:

Vector *p*-Norm:

Take the vector $\boldsymbol{a}$ with n elements, $\boldsymbol{a} = \begin{bmatrix} a_1 & \dots & a_n \end{bmatrix}^T \in \mathbb{C}^n$. The vector p-norm of $\boldsymbol{a}$ is:

$$\|\boldsymbol{a}\|_p = \left(\sum_i |a_i|^p \right)^{1/p}, \tag{A.6}$$

where $p \geq 1$ and $|a_i|$ is the absolute value of the complex scalar a_i [**10**].

The special case where $p = \infty$ is considered. This is the vector ∞-norm (or max norm) and is given by:

$$\|\boldsymbol{a}\|_\infty \triangleq \max_i |a_i|, \tag{A.7}$$

where the vector ∞-norm is the largest element value in the vector [**1**].

Induced Matrix *p*-Norm:

Induced matrix norms are directly related to signal amplification in systems, making them important [**10**]. For example, the matrix $\boldsymbol{A} = \left[a_{ij} \right] \in \mathbb{C}^{m \times n}$ has the induced[35] matrix p-norm:

$$\|\boldsymbol{A}\|_p = \max_{w \neq 0} \frac{\|\boldsymbol{Aw}\|_p}{\|\boldsymbol{w}\|_p}, \tag{A.8}$$

with $p \geq 1$ [**1**].

Consider again the special case where $p = \infty$, then:

$$\|\boldsymbol{A}\|_\infty = \max_i \left(\sum_j |a_{ij}| \right), \tag{A.9}$$

which can be translated as the largest row sum [**10**].

---

[35] The norm is induced because the "gain" of the equation $\boldsymbol{z} = \boldsymbol{Aw} \leftrightarrow \dfrac{\boldsymbol{z}}{\boldsymbol{w}} = \boldsymbol{A}$ is induced by $\boldsymbol{w}$ [**1**].

H_∞ Norm of a System:

For the dynamic system $\boldsymbol{G}(s)$, the H_∞ norm is the supremum[36] over all frequencies of the largest singular value of $\boldsymbol{G}(j\omega)$ [**1**]:

$$\left\|\boldsymbol{G}(s)\right\|_\infty = \sup_\omega \bar{\sigma}(\boldsymbol{G}(j\omega)). \tag{A.10}$$

In other words, it is simply the peak value of $\left|\boldsymbol{G}(j\omega)\right|$ as a function of frequency [**10**]:

$$\left\|\boldsymbol{G}(s)\right\|_\infty \triangleq \max_\omega \left|\boldsymbol{G}(j\omega)\right|. \tag{A.11}$$

If correlated with the induced matrix norm, the maximum magnitude over frequency can be given as [**10**]:

$$\max_\omega \left|\boldsymbol{G}(j\omega)\right| = \lim_{p\to\infty}\left(\int_{-\infty}^{\infty}\left|\boldsymbol{G}(j\omega)\right|^p d\omega\right)^{1/p}. \tag{A.12}$$

In the time domain reference, it can be explained as the worst-case gain at any frequency for sinusoidal inputs [**10**]. At any given frequency, the maximum singular value gives the gain in the worst-case direction[37] of a system's response. Because frequency also influences the gain, the H_∞ norm represents the gain at the worst-case frequency [**10**]. In other words, it is the largest of the maximum singular values of the system over all frequencies. The H_∞ norm is the peak value read from a singular value Bode plot of a system [**12**]. The H_∞ norm can be translated as the greatest effect noises, disturbances and uncertainties can have upon controlled signals in a specific frequency range [**11**].

A.3 Condition number:

The condition number is the ratio between the maximum and minimum singular values [**10**],

$$\gamma(\boldsymbol{G}) \triangleq \bar{\sigma}(\boldsymbol{G}) / \underline{\sigma}(\boldsymbol{G}). \tag{A.13}$$

The minimized or optimal condition number is given as:

$$\gamma^*(\boldsymbol{G}) = \min_{\boldsymbol{D}_1,\boldsymbol{D}_2} \gamma(\boldsymbol{D}_1\boldsymbol{G}\boldsymbol{D}_2), \tag{A.14}$$

where $\boldsymbol{D}_1$ and $\boldsymbol{D}_2$ are diagonal scaling matrices [**19**].

---

[36] The supremum, also called the maximum, is the largest upper bound. In engineering, there is no difference between supremum and maximum [**10**].

[37] Multivariable system gains have different directions; from the different inputs, to the different outputs.

A matrix with a large condition number is ill-conditioned, although it depends on the scaling of the inputs and outputs [**19**]. A large condition number may indicate control problems:

- A large condition number $\gamma(\boldsymbol{G}) \triangleq \overline{\sigma}(\boldsymbol{G}) / \underline{\sigma}(\boldsymbol{G})$ may be caused by a small value of $\underline{\sigma}(\boldsymbol{G})$.
- A large condition number may mean the plant has a large minimized condition number.
- A plant with a large condition number is NOT generally concluded to be sensitive to uncertainty.

Appendix B: Mathematical equations

B.1 Moments of inertia:

The inertia properties of a rigid body for rotational motions are characterized by six mass moments. The inertia I_x in the x direction, I_y in the y direction and I_z in the z direction (also the axis of rotation) are [**6**]:

$$I_x = \int \left(y^2 + z^2 \right) dm, \qquad I_{yz} = \int yzdm, \tag{B.1}$$

$$I_y = \int \left(x^2 + z^2 \right) dm, \qquad I_{xz} = \int xzdm \tag{B.2}$$

and

$$I_z = \int \left(x^2 + y^2 \right) dm, \qquad I_{xy} = \int xydm. \tag{B.3}$$

An alternative method for obtaining the moments of inertia for a rotor and a disc is to calculate the inertia of the rotor and of the disc separately, and add them together to form the total moment of inertia. This can be seen in the three equations below [**29**]:

$$I_{x\_rotor} + I_{x\_disc} = \frac{m_{rotor}(3r_{rotor}^2 + h_{rotor}^2)}{12} + \frac{m_{disc} r_{disc}^2}{4}, \tag{B.4}$$

$$I_y = I_x, \tag{B.5}$$

$$I_{z\_rotor} + I_{z\_disc} = \frac{m_{rotor} r_{rotor}^2}{2} + \frac{m_{disc} r_{disc}^2}{2}, \tag{B.6}$$

where m is the rotor mass, r is the radius and h the rotor length.

Appendix C: State-space models

C.1 Sensor state-space values:

The state-space representation of the sensors calculated in MATLAB® is given below:

a =

	x1	x2	x3	x4	x5	x6	x7	x8	x9	x10
x1	-8.886e+004	-6.024e+004	0	0	0	0	0	0	0	0
x2	6.554e+004	0	0	0	0	0	0	0	0	0
x3	0	0	-8.886e+004	-6.024e+004	0	0	0	0	0	0
x4	0	0	6.554e+004	0	0	0	0	0	0	0
x5	0	0	0	0	-8.886e+004	-6.024e+004	0	0	0	0
x6	0	0	0	0	6.554e+004	0	0	0	0	0
x7	0	0	0	0	0	0	-8.886e+004	-6.024e+004	0	0
x8	0	0	0	0	0	0	6.554e+004	0	0	0
x9	0	0	0	0	0	0	0	0	-8.886e+004	-6.024e+004
x10	0	0	0	0	0	0	0	0	6.554e+004	0

b =

	u1	u2	u3	u4	u5
x1	256	0	0	0	0
x2	0	0	0	0	0
x3	0	256	0	0	0
x4	0	0	0	0	0
x5	0	0	256	0	0
x6	0	0	0	0	0
x7	0	0	0	256	0
x8	0	0	0	0	0
x9	0	0	0	0	256
x10	0	0	0	0	0

c =

	x1	x2	x3	x4	x5	x6	x7	x8	x9	x10
y1	0	353	0	0	0	0	0	0	0	0
y2	0	0	0	305.9	0	0	0	0	0	0
y3	0	0	0	0	0	353	0	0	0	0
y4	0	0	0	0	0	0	0	305.9	0	0
y5	0	0	0	0	0	0	0	0	0	353

C.2 Power amplifier state-space values:

The state-space representation of the PAs calculated in MATLAB® is given below:

a =

	PA1x1	PA1x2	PA2x1	PA2x2	PA3x1	PA3x2	PA4x1	PA4x2	PAZx1	PAZx2
PA1x1	-1.573e+004	-49.08	0	0	0	0	0	0	0	0
PA1x2	32	0	0	0	0	0	0	0	0	0
PA2x1	0	0	-1.573e+004	-49.08	0	0	0	0	0	0
PA2x2	0	0	32	0	0	0	0	0	0	0
PA3x1	0	0	0	0	-1.573e+004	-49.08	0	0	0	0
PA3x2	0	0	0	0	32	0	0	0	0	0
PA4x1	0	0	0	0	0	0	-1.573e+004	-49.08	0	0
PA4x2	0	0	0	0	0	0	32	0	0	0
PAZx1	0	0	0	0	0	0	0	0	-1.573e+004	-49.08
PAZx2	0	0	0	0	0	0	0	0	32	0

b =

	PA I_X1 In	PA I_Y1 In	PA I_X2 In	PA I_Y2 In	PA I_Z In
PA1x1	128	0	0	0	0
PA1x2	0	0	0	0	0
PA2x1	0	128	0	0	0
PA2x2	0	0	0	0	0
PA3x1	0	0	128	0	0
PA3x2	0	0	0	0	0
PA4x1	0	0	0	128	0
PA4x2	0	0	0	0	0
PAZx1	0	0	0	0	128
PAZx2	0	0	0	0	0

c =

	PA1x1	PA1x2	PA2x1	PA2x2	PA3x1	PA3x2	PA4x1	PA4x2	PAZx1	PAZx2
PA I_X1 Out	122.7	0.3835	0	0	0	0	0	0	0	0
PA I_Y1 Out	0	0	122.7	0.3835	0	0	0	0	0	0
PA I_X2 Out	0	0	0	0	122.7	0.3835	0	0	0	0
PA I_Y2 Out	0	0	0	0	0	0	122.7	0.3835	0	0
PA I_Z Out	0	0	0	0	0	0	0	0	122.7	0.3835

C.3 Anti-aliasing filters state-space values:

The state-space representation of the anti-aliasing filters is given below:

a =

	x1	x2	x3	x4	x5
x1	-3.028e+004	0	0	0	0
x2	0	-3.028e+004	0	0	0
x3	0	0	-3.028e+004	0	0
x4	0	0	0	-3.028e+004	0
x5	0	0	0	0	-3.028e+004

b =

	u1	u2	u3	u4	u5
x1	128	0	0	0	0
x2	0	128	0	0	0
x3	0	0	128	0	0
x4	0	0	0	128	0
x5	0	0	0	0	128

c =

	x1	x2	x3	x4	x5
y1	236.6	0	0	0	0
y2	0	236.6	0	0	0
y3	0	0	236.6	0	0
y4	0	0	0	236.6	0
y5	0	0	0	0	236.6

C.4 Controller state-space values:

The state-space representation of the H_∞ controller is given below:

a =

	x1	x2	x3	x4	x5	x6	x7	x8	x9	x10	x11
x1	-264.4	76.88	2954	0	0	0	0	0	0	0	0
x2	38.18	-12.57	-596.8	0	0	0	0	0	0	0	0
x3	-1294	230.3	-3078	0	0	0	0	0	0	0	0
x4	0	0	0	-440.8	0.4813	-142.1	-0.04643	20.57	80.55	-102.7	7.651
x5	0	0	0	-0.4813	-440.8	0.04643	-142.1	80.55	-20.57	7.651	102.7
x6	0	0	0	862.3	-0.1966	-922.9	0.000886	78	307.5	144.4	-10.27
x7	0	0	0	0.1966	862.3	-0.0008749	-922.9	307.5	-78	-10.27	-144.4
x8	0	0	0	-76.07	-299.3	49.64	195.7	-76.11	-0.02152	-10.5	58.92
x9	0	0	0	-299.3	76.07	195.7	-49.64	0.02152	-76.11	-58.92	-10.5
x10	0	0	0	-73.25	4.984	49.75	-2.755	0.0322	1.665	-32.69	0.05116
x11	0	0	0	4.984	73.25	-2.755	-49.75	-1.665	0.0322	-0.05116	-32.69
x12	0	0	0	95.93	591.1	57.15	351.8	-29.18	2.487	-4.917	47.54
x13	0	0	0	591.1	-95.93	351.8	-57.15	-2.487	-29.18	-47.54	-4.917
x14	0	0	0	-167.5	-21.92	926.6	121	-88.01	-221.6	-255.9	51.47
x15	0	0	0	-21.92	167.5	121	-926.6	221.6	-88.01	-51.47	-255.9
x16	0	0	0	15	93.84	-31.29	-195.1	78.51	-6.955	28.89	-322.4
x17	0	0	0	93.84	-15	-195.1	31.29	6.955	78.51	322.4	28.89
x18	0	0	0	-3027	126.3	-1040	43.04	42.11	199.5	-712.8	23.74
x19	0	0	0	-126.3	-3027	-43.04	-1040	199.5	-42.11	23.74	712.8

	x12	x13	x14	x15	x16	x17	x18	x19
x1	0	0	0	0	0	0	0	0
x2	0	0	0	0	0	0	0	0
x3	0	0	0	0	0	0	0	0
x4	4.492	28.32	472.3	61.63	-207.2	-1282	3757	157.2
x5	28.32	-4.492	61.63	-472.3	-1282	207.2	-157.2	3757
x6	-207.4	-1283	-1584	-206.7	291.7	1810	1778	73.78
x7	-1283	207.4	-206.7	1584	1810	-291.7	-73.78	1778
x8	305.9	27.05	154.2	-388.1	-488.1	-43.33	-115.9	-550.1
x9	-27.05	305.9	388.1	154.2	43.33	-488.1	-550.1	115.9
x10	-1.472	-25.34	189.8	37.84	-30.26	-335.1	1021	-33.77
x11	25.34	-1.472	-37.84	189.8	335.1	-30.26	-33.77	-1021
x12	-1135	0.4153	-115.1	386.5	958.5	0.2986	268.9	2254
x13	-0.4153	-1135	-386.5	-115.1	-0.2986	958.5	2254	-268.9
x14	-317.7	-1064	-564.9	-0.04962	259.8	872	1456	251
x15	1064	-317.7	0.04962	-564.9	-872	259.8	251	-1456
x16	2112	-0.9703	364.8	-1224	-2691	-0.1252	250.8	2106
x17	0.9703	2112	1224	364.8	0.1252	-2691	2106	-250.8
x18	-95.32	-803.5	-909.1	-156.6	-132.7	-1115	-3048	0.07351
x19	-803.5	95.32	-156.6	909.1	-1115	132.7	-0.07351	-3048

b =

	u1	u2	u3	u4	u5
x1	2864	0	0	0	0
x2	-550.6	0	0	0	0
x3	-7890	0	0	0	0
x4	0	331.1	1920	70.96	405.2
x5	0	-1920	331.1	-405.2	70.96
x6	0	218.7	1265	-490.4	-2826
x7	0	-1265	218.7	2826	-490.4
x8	0	558.2	-249.5	-835.9	373.4
x9	0	-249.5	-558.2	373.4	835.9
x10	0	157.6	629	174.7	712.6
x11	0	629	-157.6	712.6	-174.7
x12	0	-2226	766.9	-2761	953.3
x13	0	766.9	2226	953.3	2761
x14	0	82.34	1954	125.1	2970
x15	0	1954	-82.34	2970	-125.1
x16	0	-1575	541.8	4477	-1542
x17	0	541.8	1575	-1542	-4477
x18	0	-2515	-1.164e+004	181.9	842.9
x19	0	1.164e+004	-2515	-842.9	181.9

c =

	x1	x2	x3	x4	x5	x6	x7	x8	x9	x10
y1	1696	-327.9	-9037	0	0	0	0	0	0	0
y2	0	0	0	282.5	-1639	183.8	-1064	484.7	-216.5	138.4
y3	0	0	0	1639	282.5	1064	183.8	-216.5	-484.7	552.3
y4	0	0	0	474.6	-2737	-956.2	5508	-1546	691	247.8
y5	0	0	0	2737	474.6	-5508	-956.2	691	1546	1009

	x11	x12	x13	x14	x15	x16	x17	x18	x19
y1	0	0	0	0	0	0	0	0	0
y2	552.3	-1712	589.4	33.39	796.1	-1880	647.1	-3697	1.712e+004
y3	-138.4	589.4	1712	796.1	-33.39	647.1	1880	-1.712e+004	-3697
y4	1009	1099	-378.2	-50.66	-1200	-2342	807.1	426.5	-1975
y5	-247.8	-378.2	-1099	-1200	50.66	807.1	2342	1975	426.5

d =

	u1	u2	u3	u4	u5
y1	0	0	0	0	0
y2	0	0	0	0	0
y3	0	0	0	0	0
y4	0	0	0	0	0
y5	0	0	0	0	0

Appendix D: Images of Fly-UPS system

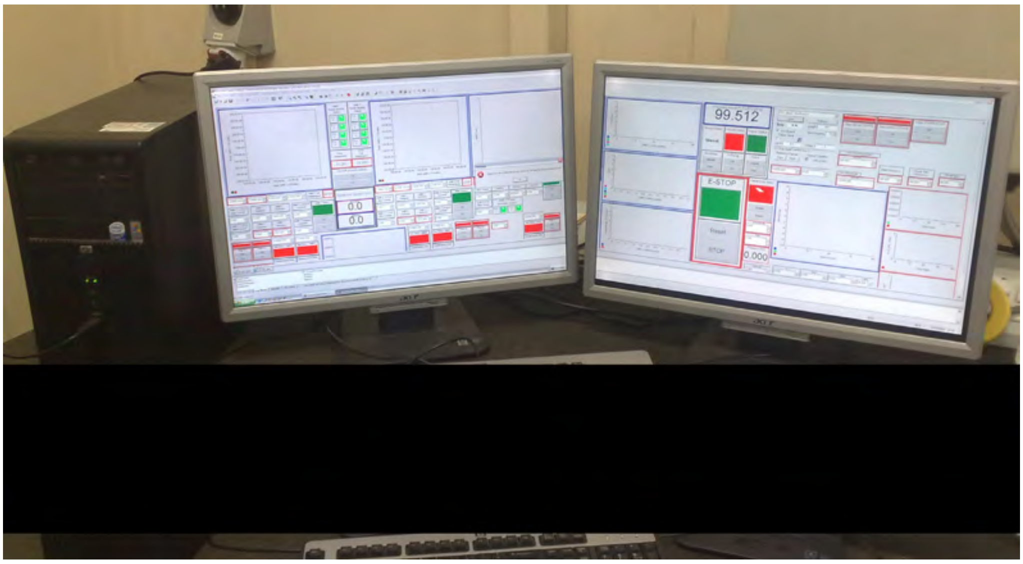

Figure D-1: Desktop computer running GUI

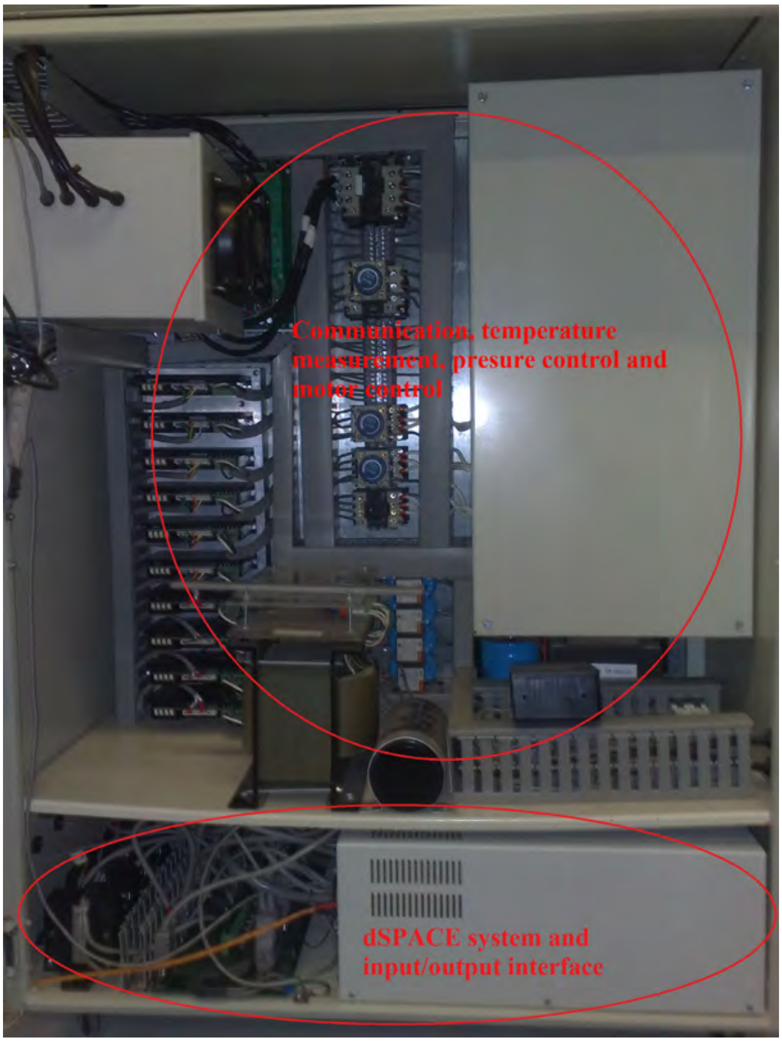

Figure D-2: Hardware controller and interface housing

Figure D-3: Physical Fly-UPS system

Appendix E: Publications

South African Power Electronics Conference (SAUPEC) 2010

S. J. M Steyn, P. A. Van Vuuren, and G. van Schoor, "Multivariable H_∞ Control for an LTI Active Magnetic Bearing Flywheel System," in *Proceedings of the 19th Southern African Universities Power Engineering Conference*, Johannesburg, South-Africa, January 28-29, 2010, pp. 100-106.

United Kingdom Automation and Control Council (UKACC) 2010

S. J. M Steyn, P. A. Van Vuuren, and G. van Schoor, "Multivariable H_∞ Control for an Active Magnetic Bearing Flywheel System," in *Proceedings of the UKACC International Conference on CONTROL 2010*, Coventry, United Kingdom, September 7-10, 2010, pp. 1014-1019.

References

[1] B. Aeschlimann, "Control Aspects of High Precision Active Magnetic Bearings," Ph.D. Thesis, Dept. Elect./Electron. Eng., EPFL, Lausanne, 2002.

[2] G. Li, "Robust Stabilization of rotor- active magnetic bearings systems," Ph.D. Thesis, Dept. Mech./Aero. Eng., Virginia Univ., Virginia, 2007.

[3] B. C. D. Wilson, "Control designs for low-loss active magnetic bearings: Theory and Implementation," Ph.D. Thesis, Dept. Elect./Electron. Eng., Georgia Inst. of Tech., Georgia, 2004.

[4] S. Myburgh, "The Development of a fully suspended AMB system for a high speed flywheel system," M.Eng. Dissertation, Dept. Elect./Electron. Eng., North-West Univ., 2007.

[5] N.-C. Tsai, C.-H. Kuo, and R.-M. Lee, "Regulation on radial position deviation for vertical AMB systems," *Mechanical Systems and Signal Processing*, vol. 21, no. 7, pp. 2777-2793, 2007.

[6] G. Schweitzer, H. Bleuler, and A. Traxler, *Active Magnetic Bearings, Basics, Properties and applications of Active Magnetic Bearings*. Zϋrich: Authors Working Group, 2003.

[7] R. Larsonneur, "Design and Control of Active Magnetic Bearing Systems for High Speed Rotation," Ph.D. Thesis, Dept. Mech./Aero. Eng., Georgia Inst. of Tech., Zurich, 1990.

[8] G. J. Sussman, "Building Robust Systems; an Essay," Massachusetts Institute of Technology, 2007.

[9] H. Choi, G. Buckner, and N. Gibson, "Neural Robust Control of a High-Speed Flexible Rotor Supported on Active Magnetic Bearings," in *Proceedings of the 2006 American Control Conference*, Minneapolis, 2006, pp. 3679-3684.

[10] S. Skogestad and I. Postlethwaite, *Multivariable Feedback Control Analysis and Design*. West Sussex, England: John Wiley & Sons Ltd., 2005.

[11] N. S. Gibson, "H-infinity Control of Active Magnetic Bearings: An Intelligent Uncertainty Modeling Approach," Ph.D. Thesis, Dept. Mech./Aero. Eng., North Carolina State Univ., North Carolina, 2004.

[12] K. Zhou, J. C. Doyle, and K. Glover, *Robust and Optimal Control*. Upper Saddle River, New Jersey: Prentice Hall, 1996.

[13] R. S. Sànchez-Pena and M. Sznaier, *Robust Systems Theory and Applications*. NY: John Wiley and Sons, Inc., 1998.

[14] MATLAB®. (2004) The language for Technical Computing. The MathWorks, Inc. [DVD].

[15] ISO-TC108/SC2/WG7, "Active magnetic bearing – evaluation of stability margin," *ISO CD148393-3*, Oct. 2003.

[16] E. O. Ranft, "The Development of a Flexible Rotor Active Magnetic Bearing System," M.Eng. Dissertation, Dept. Elect./Electron. Eng., North-West Univ., 2005.

[17] L. A. Hawkins, "Analysis and Testing of a Magnetic Bearing Energy Storage Flywheel with Gain-Scheduled, MIMO Control," in *ASME TURBOEXPO 2000*, Munich, Germany, 2000, pp. 405-412.

[18] S. J. M. Steyn, "The development of MIMO control for an AMB energy storage flywheel system," Mini-Dissertation, Dept. Elect./Electron. Eng., North-West Univ., 2008.

[19] J. W. Helton and O. Merino, *Classical Control Using H∞ methods: An Introduction to Design*. Philadelphia, USA: Society for Industrial and Applied Mathematics, 1998.

[20] R. C. Dorf and R. H. Bishop, *Modern Control Systems*. Upper Saddle River, New Jersey: Prentice Hall, 2005.

[21] L. Ljung, *System Identification: Theory for the User*. Upper Saddle River, New Jersey: Prentice Hall, 1999.

[22] J. J. Janse van Rensburg, "Development of a flywheel energy storage system – uninterrupted power supply (FLY-UPS)," M.S. dissertation, Dept. Elect./Electron. Eng., North-West Univ., South-Africa, 2007.

[23] B. Lu, H. Choi, G. D. Buckner, and K. Tammi, "Linear parameter-varying techniques for control of a magnetic bearing system," *Control Engineering Practice*, no. 16, pp. 1161-1172, Jan. 2008.

[24] D. W. Gu, P. H. Petkov, and M. M. Konstantinov, *Robust Control Design with MATLAB*. London, United Kingdom: Springer-Verlag London, 2005.

[25] R. L. Fittro, "A High Speed Machining Spindle with Active Magnetic Bearings: Control Theory, Design and Application," Ph.D. Thesis, Dept. Mech./Aero./Nuc. Eng., Univ. of Virginia, Virginia, 1998.

[26] K. A. Folly, "On the Prevention of Pole-Zero Cancellation in H-infinity Power System Controller Design: a Comparison," *South African Institute of Electrical Engineers*, vol. 99, no. 4, pp. 103-113, Dec. 2008.

[27] G. Li, E. H. Maslen, and P. E. Allaire, "A Note on ISO AMB Stability Margin," in *Proceedings of the tenth international symposium on magnetic bearings*, Martigny, Switzerland, August 21-23, 2006.

[28] J. M. Layton, *Multivariable Control Theory*. Southgate House, England: Peter Peregrinus Ltd., 1976.

[29] R. C. Hibbeler, *Engineering Mechanics Dynamics*, 3rd ed. Jurong, Singapore: Prentice Hall, 2004.

[30] M. S. Sarma, *Electric Machines Steady-State Theory and Dynamic Performance*, 2nd ed. Boston: PSW Publish. Comp., 1996.

[31] L. W. Johnson, R. D. Riess, and J. T. Arnold, *Introduction to Linear Algebra*, 5th ed. United States of America: Pearson Education, Inc., 2002.

[32] Alternative Energy Storage Methods. [Online]. Available: www.mpoweruk.com, [Date of access: April 2010].

[33] T. E. Seiphethlo, "Power electronic activation for active magnetic bearings," M.Eng. Dissertation, Dept. Elect./Electron. Eng., North-West Univ., 2006.

[34] dSPACE Solutions for Control. [Online]. Available: www.dspace.de, [Date of access: May 2010].